# Physical Processes in Complex Plasma

**Slobodan Mitić**


München 2010

# Physical Processes in Complex Plasma

**Slobodan Mitić**

Dissertation
der Fakultät für Physik
der Ludwig–Maximilians–Universität
München

vorgelegt von
Slobodan Mitić
aus Niš / Serbien

München, den 30. March 2010

Erstgutachter: Prof. Dr. Gregor E. Morfill

Zweitgutachter: Prof. Dr. Dietrich Habs

Tag der mündlichen Prüfung: 15. Jun 2010.

# Contents

# List of Figures

# Abstract

This thesis is a cumulative dissertation that consists of four papers addressing the different aspects of complex plasmas.

The first paper addresses the issue of structural properties of complex plasma in elongated dc discharge chamber. The main motivation for this work was based on a detailed three-dimensional reconstruction of complex plasmas rarely investigated so far. The analysis of the structural arrangement of particles is one of the fundamental questions in complex plasma crystals. In this work a full three-dimensional reconstruction of the positions of a few thousand particles was done. The reconstruction of particles positions revealed the locally enhanced structural properties that indicate that the system was near crystallization. Due to the strong influence of gravity a combination of pronounced macro structures is clearly visible, like shells and layers. Presented results might help us to understand similar generic properties of the other cylindrical-shaped systems, particularly those on the nano-meter scale.

The second paper enclosed in this thesis is focused on fundamental gas thermodynamic properties. The convective motion of particles in complex plasma experiments is a common effect. In most cases the origin of this motion was described by a temperature gradient in the discharge or electric forces. In this particular experiment particles experienced unusually high velocities due to the convective motion of the background gas. By detailed analysis it was found that the convection of the gas is produced by the thermal gas creep effect. The main results of this work are the confirmation of the presence of gas creep in typical conditions for complex plasmas experiments, a full reconstruction of the gas velocity pattern and a rare experimental example of this effect.

The third work is oriented to the important question of complex plasma diagnostics by means of optical emission spectroscopy. For this purpose the density of metastables in an argon plasma was estimated in the case of a pure plasma and a plasma with a microparticle cloud levitated in it. The estimation of the metastable density was based on measuring the selfabsorption of the pure plasma and the complex plasma. For the complex plasma an additional correction had to be implemented for the light extinction on the surface of the microparticles. The correction factor was experimentally evaluated. It was found that the presence of particles in the plasma influence the metastable density in a non-local way. Results presented here confirms the changes in plasma parameters (metastable density) due to the presence of particles and introduces wavelength dependent light extinction on particles as an important effect for any spectroscopic observation of complex plasmas.

The fourth paper is the logical extension of the previous work where changes of the electron temperature

were evaluated due to the presence of microparticles in the plasma. For this purpose a simple model was created based on the metastable density and light intensity measurements from previous work. The proposed model was demonstrated on the results of the previous work taking into account three spectral lines with the assumption of a simple Maxwellian EEDF. The advantage of the proposed model lies in the possibility of its extension to more spectral lines and a more complicated EEDF. The model was demonstrated for the case of a pure plasma and a plasma with particles. As a result the evaluated changes of electron temperatures are in agreement with the profiles of the light emission and metastable densities.

# Zusammenfassung

Diese Doktorarbeit ist eine kumulative Dissertation bestehend aus vier Veröffentlichungen, die sich mit verschiedenen Aspekten der komplexen Plasmen befassen.

Die erste Veröffentlichung behandelt die strukturellen Eigenschaften komplexer Plasmen in einer länglichen DC-Entladungskammer. Die vordergründige Motivation dieser Arbeit war eine detailgetreue, dreidimensionale Rekonstruktion komplexer Plasmen, wie sie bis jetzt kaum untersucht wurde. Die Analyse der strukturellen Anordnung von Teilchen ist eine der grundlegenden Fragen auf dem Gebiet der komplexen Plasmakristalle. In dieser Arbeit wurde eine vollständige, dreidimensionale Rekonstruktion einiger tausend Teilchen bewerkstelligt. Die Rekonstruktion der Teilchenpositionen gab die lokal verstärkten, strukturellen Eigenschaften zu erkennen, die zeigen, dass sich das System nahe der Kristallisation befand. Durch den starken Einfluss der Gravitation wird eine Kombination ausgeprägter Makrostrukturen - ähnlich zu Schalen und Lagen - deutlich sichtbar. Die hier präsentierten Ergebnisse könnten uns helfen, ähnliche grundlegende Eigenschaften der anderen zylindrisch geformten Systeme zu verstehen, im besonderen derer in der Grössenordnung von Nanometern.

Die in dieser Doktorarbeit enthaltene zweite Veröffentlichung konzentriert sich auf grundlegende thermodynamische Eigenschaften von Gasen. Die Konvektionsbewegung von Teilchen in Experimenten mit komplexen Plasmen ist ein verbreiteter Effekt. In den meisten Fällen wurde der Ursprung dieser Bewegung durch einen Temperaturgradienten in der Entladung oder den elektrischen Kräften beschrieben. In diesem speziellen Experiment erfuhren die Teilchen ungewöhnlich hohe Geschwindigkeiten durch die Konvektionsbewegung des Hintergrundgases. Eine detaillierte Analyse ergab als Grund für die Konvektion des Gases den thermischen Kriecheffekt des Gases. Die Bestätigung der Existenz dieses Effektes, und eine vollständige Rekonstruktion der Gasgeschwindigkeitsmuster sind das vorrangige Ergebnis dieser Arbeit. Die wichtigsten Ergebnisse dieser Arbeit sind die Bestätigung der Existenz von Kriecheffekten unter typischen Bedingungen in Experimenten mit komplexen Plasmen, die vollständige Rekonstruktion der Gasgeschwindigkeitsmuster, und das seltene experimentelle Beispiel dieses Effektes.

Die dritte Arbeit wendet sich an die wichtige Frage der Diagnostik komplexer Plasmen mittels optischer Emissionsspektroskopie. Zu diesem Zweck wurde die Dichte von metastabilen Atomen in einem Argonplasma bestimmt, zum einen für ein reines Plasma, zum anderen für ein Plasma in dem eine Wolke aus Mikroteilchen schwebte. Die Bestimmung der Dichte der metastabilen Atome basierte auf der Messung der Selbstabsorption des reinen und des komplexen Plasmas. Im Fall des komplexen Plasmas musste eine zusätzliche Korrektur für die Auslöschung von Licht auf der Oberfläche der Mikroteilchen eingebaut werden. Der Korrekturfaktor wurde experimentell bestimmt. Es ergab sich, dass die Anwesenheit von Mikroteilchen im Plasma die Dichte der metastabilen Atome auf eine nicht örtlich beschränkte Weise beeinflusst. Die hier gezeigten Ergebnisse bestätigen die Veränderungen in Plasmaparametern (Dichte der metastabilen Atome), verursacht durch die Anwesenheit von Teilchen, und führen die Wellenlängenabhängige Lichtauslöschung auf Teilchen als einen wichtigen Effekt für jegliche spektroskopische Beobachtung komplexer Plasmen ein.

Die vierte Veröffentlichung ist die logische Erweiterung der vorhergehenden Arbeit. Hier wurden Veränderungen der Elektronentemperatur durch die Präsenz von Mikroteilchen im Plasma ausgewertet. Ein einfaches Modell, basierend auf der Dichte der metastabilen Atome und der Messung der Lichtintensität, wurde dafür entworfen. Das vorgeschlagene Modell wurde anhand der Ergebnisse früherer Arbeiten veranschaulicht, wobei drei Spektrallinien verwendet wurden, unter der Annahme einer einfachen Maxwellschen EEDF. Der Vorteil des vorgeschlagenen Modells liegt in seiner Erweiterungsmöglichkeit um mehr Spektrallinien und einer komplizierteren EEDF. Das Modell wurde sowohl für ein reines Plasma, als auch ein Plasma mit Teilchen vorgestellt. Die als Ergebnis ermittelten Änderungen der Elektronentemperatur sind in Übereinstimmung mit den Profilen der Lichtemission und den Dichten der metastabilen Atome.

# Chapter 1

# Introduction

## 1.1 General review of complex plasma

Complex plasmas represent systems of small solid (dust) particles immersed into a plasma. Plasma-particle interaction and particle-particle interaction result in very complex and interesting underling physics of complex plasmas.

The number of parameters (plasma parameters, particle size and material, concentration) and their range allow to engineer complex plasmas in many different ways.

Starting from star forming regions, interplanetary medium, planetary rings, Earth's atmosphere, large number of industrial applications, laboratories investigations to fusion reactors and new materials, complex plasmas are ubiquitous and making their mark in physics.

The observation of small solid particles in a discharge due to the sputtering of the cathode material in 1920's by Langmuire [1] represents the first publication of aggregates immersed in a discharge.

Latter investigation of space environments found the presence of dust particles almost everywhere. The well known observation of spokes in saturn's B ring in the early 1980's represent a key point for dusty/complex plasmas. Theories built to explain this phenomena led to a number of studies proposing particle - plasma interaction and charging processes in space plasmas [2], [3]. Further studies were initiated in mid 1990's with the prediction of Ikezi in 1986 about a possible crystallization of higly-charged particles in a plasma due to the strong electrostatic coupling. First experiments of ordered particle structure were

reported in 1994 in an rf discharge [4], [5], [6], [7]. From this point on Complex plasmas started to develop very fast.

### 1.1.1 Complex plasma in nature

The study of plasma-dust interaction are of major interest in astrophysics due to the presence of dust almost anywhere in space. The closest example of dusty plasma in nature have been observed in the lower part of the Earth's ionosphere. The most significant phenomenon is the formation of a special type of clouds, named noctilucent clouds (NLC) (from latin - night shining) and micro-meteorits. The NLC are composed of ice, heavy ion clusters, dust from man made pollution (terrestrial aerosols). They are visible only when illuminated by sunlight from below the horizon, while the ground and lower layers of the atmosphere are in the Earth's shadow. Due to the presence of sub-micronsize particles in the ionized surrounding of the NLC there is a strong radar backscattering at MHz and GHz frequencies [8].

A new group of examples of complex plasmas existing in nature can be observed in space environment. Most of the rings of the giant planets contain micron to sub-micron size of dust particles and with further analysis a wealth of information was recovered [9]. First observation of the Jupiter's rings were made in 1979 and inspired the further research. Observation of planetary rings continue with recordings of Saturn's rings and legendary "spokes" which were an inspiration for a number of publications and theories about charge and dust-plasma interaction [10], [11], [12], [13], [14].

Away from the planets other types of particles can be found. The origin of the interplanetary dust is mainly from comets and asteroids. Submicrometer dust is mainly composed of carbon mineral grains. Zodiacal light and cometary dust tails are great representations of complex plasmas in the planetary systems. A bright comet is an excellent cosmic laboratory for the study of dust-plasma interactions, and their physical and dynamical consequences. As the comet approaches the Sun, at few AU, the nucleus is warming up and a long tail of evaporated molecules, carrying small solid particles, is formed. The Suns radiation pressure and the solar wind accelerate in different ways the components of comets tail. The ion tail formed by the UV radiation from the Sun appears as a more or less straight line, opposite to the Sun, while the dust tail is slower accelerated, being much broader and tends to be curved.

Smaller dust particles can be found in the interstellar medium. This submicron size particles are mainly composed of silicates, carbon, ice and iron compounds. Dust in the interstellar medium can play an important role in spectral observations of light from other stars. Depending on the particle size and particle number density, the passing light can by dimmed due to the extinction of light by particles. If the dust cloud is thick enough, the light will be completely blocked, leading to dark areas. These dark clouds are known as dark nebulae.

### 1.1.2 Complex plasma in industry

The development of surface-processing, etching and computer chips industry using chemically active discharges in early 1990s were faced with the presence of levitating grains in the plasma which triggered further investigation in the direction of complex plasmas [15], [16], [17]. The physics of grain formation and growth in etching processes is actively investigated [18], [19]. Presence of dust in almost all industrial plasma is a big problem due to contamination of semiconductors, films etc. Argon silane mixture is widely used as buffer gas in industry and a great number of publication were devoted to the growth of particles in it [20], [21], [22], [23], [24], [25], [26], [27].

The transport of dust particles in the discharge has also been well studied (see for example [28], [29]). Depending on the construction of the discharge different forces can be used to confine and move particles. Manipulation of a dust cloud or an individual particle become a great tool for industry and for experimental use [30].

Over the years, research of complex plasmas redefined the role of dust in plasmas from unwelcome, disturbing contaminants to often desirable elements that can, for example dramatically improve the basic properties of plasma-made thin films. The useful presence of particles in plasmas triggered new directions in applied plasma research. Particles were produced by employing plasma technologies in order to create small size (from nanometer to micrometer range) mono-dispersed particles from different materials and with different properties. Now, that particles were produced with unique and desirable qualities, new possibilities opened for their use in several applications like ceramics, catalysis and optoelectronics. For example, it was found that nanometer sized structures of silicon material have increased photoemission properties then the bulk material under the radiation in visible spectrum. Plasma (complex plasma) technologies have been devoted to the synthesis of

such materials with promising optoelectronic and electronic properties. The incorporation of these particles into the crystalline layers led to an enhancement of the layer properties: the crystalline structure was improved, it had a higher stability under thermal annealing and the defect density was reduced. As a result those materials are highly suitable for thin film transistors and solar cells [31], [32].

Detailed studies of particle formation and growth in plasma led to a better control of the particle production. Size, structure and composition can be tailored for the specific application [33]. Using gases like methane, ammonia or nitrogen in addition to silane plasmas lead to the formation of dust particles based on this components. A good temperature control and gas flow allows creating a desired particle stoichiometry. With the mentioned feed gases, particles like $Si_3N_4$ and $S_iC$ have been formed resistant against oxidation with very good mechanical and thermal properties, and thus are excellent catalyst support powders [34], [35].

Development of applied complex plasma research led to the creation of an entirely new class of materials by using plasma-based technologies. Increased interest of industry on dusty plasma technologies resulted in the development of applied dusty plasma research in direction of coating, surface activation, etching, modification and separation of clustered grains in the plasma environment [17].

New perspectives in the application of complex plasmas are related to their basic physical properties. The investigations of complex plasmas over the years resulted in more insight in particle interaction and the possibility to tune this interaction. Current work shows very interesting results in changing the interaction potential between the particles by external electric fields [36]. Moreover modifying the potential can result in changes of other properties like viscosity and optical properties. Resulting effects can have significant industrial applications in the production of smart materials based on fast response of complex systems on the external influence.

### 1.1.3 Complex plasma in laboratories

The development of laboratory studies of complex plasmas was triggered in mid 1990 with the discovery of the plasma crystal in laboratory conditions. Predictions of crystallization of the particle subsystem by Ikezi in 1986 was realized in 1994 in an rf discharge [37], [38], [39], [40]. Later on, plasma crystals were observed in DC discharge [41], thermal plasmas

at atmospheric pressure [42] and nuclear-induced dusty plasmas [43], [44]. Transition from a disordered gaseous-like to a liquid-like phase and the formation of plasma crystals were observed [45]. Experiments are based on particles that are either grown in chemically active discharges or injected in to the plasma.

Since then many studies (experimental and theoretical) are devoted to the investigation of charging processes, dust-dust interaction, dust-plasma interaction and the forces acting on the dust particle (electric force, neutral drag force, ion drag force, thermophoretic etc.). Recent developments of laboratory investigations give the opportunity to study complex plasmas in various types of gas discharges and in a broad parameter range (pressure, power, particle size and density etc.). The discharges are typically sustained in the pressure range from 0.1 to a few hundred Pa with input power up to a few hundreds of Watts. In such plasmas the average electron temperature is in a range from 1 to 7 eV and the ion temperature on the order of the neutral gas temperature 0.03 eV, with the electron and ion densities $n_e = n_i \sim 10^8 - 10^9 cm^{-3}$. The particle sizes usually used in the laboratories on Earth are spherical dielectric particles in the range form 1 to 10 $\mu m$ which acquire a significant negative charge in plasma of about $10^3 - 10^5$ elementary charges.

As a result of the high particle charge the interaction between particles can strongly exceed the interaction between particles and other plasma species for several orders of magnitude. In this case the behavior of the particle cloud is mainly governed by the electrostatic (repulsive) Coulomb force and these systems are known as strongly coupled Coulomb systems (liquids or crystals). Strongly coupled systems represent one of the most studied areas of complex plasmas due to the strong scientific impact on other fields and the potential in industrial applications.

Further developments in complex plasma laboratory investigations, was ignited by research under microgravity conditions, started at the end of 90s. In most complex plasma experiments under gravity particles were levitated under the influence of a strong electric field in the discharge which lead to a high anisotropy in the plasma conditions. Plasma forces acting on particles and the interparticle force were found to be much weaker than the gravitational force creating problems in experimental observations. Most complex plasmas in ground experiments are strongly compressed, inhomogeneous and anisotropic, therefore strongly limited by the influence of gravity. Therefore the study of complex plasma under microgravity conditions is of great importance. Microgravity conditions were created during parabolic flights, with sounding rocket experiments, on board of MIR and the inter-

national space station. As a result, it was possible to directly study the plasma-dust and dust-dust interactions without gravitational perturbations. There it is possible to study a much wider set of parameters and increase the size of dust particles up to hundreds of microns, which is impossible in laboratories on Earth.

Everyday research (theoretical and experimental) is still committed to the investigation of the interaction potential between particles and its control. Latest discovery that complex plasma can have electrorheological properties [36] add a new dimension to the research of electro-rheological fluids having a significant industrial application potential in hydraulics, photonics or medical engineering. Meanwhile, the research on dusty plasma interaction and particle growth is still motivated by strong technological challenges. Presence of dust particles created by plasma-wall interaction represents a serious safety hazard in thermonuclear fusion devices [28], [46]. Thus, the problem of dust removal from these devices represents one of the most important technological and scientific problems. On the other hand, nanoparticles grown in the plasma can have very useful properties. For example, the polymorphous silicon created by embedding the silicon nanoparticles in the amorphous silicon, is of major interest for the manufacture of solar cells [47], [48].

Beside all possible industrial and technological applications of complex plasmas, there is one more aspect of complex plasma research that promises to become of great importance. Complex plasmas gives the opportunity to observe the phenomena beyond the limits of continuous media on the microscopic level and study various generic processes at the kinetic level. Timescales associated with dust (in order of ms) and precise visualization of particles results in the observations of phenomena in complex plasmas on an elementary (particle) level. Complex plasmas in this context represent a fully resolved strongly coupled system known to resemble regular physical systems. The research on complex plasma crystals led to the observation of some elementary processes in crystal physics on the level of individual particles. For example, processes of crystal grow [49], re-crystallization and melting [50], [51], [52], wave propagation [53], [54], [55], dislocations observations [56], [57], structural analysis [58] were resolved in details. The results obtained with this and similar works can be easily transferred to other fields like, material science, solid state physics, fluid dynamics, nano-science etc. The liquid phase of complex plasma can be used for resolving fundamental questions in hydrodynamics, like self-organization of fluid flows, interpenetrating flows, non-equilibrium phase transition, multicomponent systems etc. In general, complex plasmas are model systems for the study of fundamental processes occur-

ring in nature. The information obtained on the elementary (particle) level represent the link between the atomistic and macroscopic behavior of the systems. A detailed overview of the interdisciplinarity of complex plasma was recently reported in [59].

# Chapter 2

# Basics of Complex Plasma

In this chapter some basics of complex plasma important for further understanding of this work are explained.

## 2.1 Microparticle charging

The screening of electric fields created by individual charged particles (ions, electrons and dust particles) or by a surface with a potential that is different to the plasma potential is a fundamental characteristic of plasma. The screening effect is defined by a characteristic length called the Debye length. Below this length the electric field of charged particles can influence other charged particles. For electron and ions the Debye lengths are defined by the following equation

$$\lambda_{e(i)} = \sqrt{\frac{\epsilon_0 k_B T_{e(i)}}{n_{e(i)0} e^2}} \tag{2.1}$$

where $k_B$ is the Boltzmann constant, $\epsilon_0$ the vacuum permittivity, $T_{e(i)}$ the electron (ion) temperature, $n_{e(i)}$ the electron (ion) density and $e$ the elementary charge.

For typical discharge conditions $T_e = 3\ eV$, $T_i = 0.03\ eV$ $n_0 = 10^{15}\ m^{-3}$ electron and ion Debye lengths are 120 $\mu$m and 13 $\mu$m respectively.

In dusty plasmas, the linearized Debye length is often used. It is given by [60]:

$$\frac{1}{\lambda_D^2} = \frac{1}{\lambda_{D_e}^2} + \frac{1}{\lambda_{D_i}^2} \tag{2.2}$$

Depending on the ratio between the Debye length and the interparticle distance $d$ two extreme cases can be considered. On one hand, when the Debye length is much smaller

than the inter-particle distance $d$, particles can be considered as isolated in the plasma. On the other hand, when $\lambda_D > d$, particle interact with each other and show a collective behavior.

In this section charging of the particles will be considered only for an isolated particle with $a \ll \lambda_D$ where $a$ is the radius of particles.

The charging process of dust particles in a plasma is governed by the contributions of all currents entering and leaving the dust surface, involving plasma electron and ion currents, photoemission and thermionic emission currents, etc.

$$\frac{dQ_d}{dt} = \sum_{ab} I_{ab} + \sum_{em} I_{em} \tag{2.3}$$

where $Q_d$ is charge of the particle and $I_{ab}$ and $I_{em}$ are currents absorbed and emitted by the particle with appropriate signs. In most cases for discharge plasmas, one can ignore emission currents so the particle consequently get charged by the accumulation of charged plasma particles:

$$\frac{dQ_d}{dt} = \sum_{j} I_j \tag{2.4}$$

where $I_j$ is the current associated to the species $j$.

In the stationary regime the charge of the particle depends on the frequency of collisions of electrons and ions with the particle. In most plasmas $v_e \gg v_i$ where $v_{e(i)} = \sqrt{8k_B T_{e(i)}/\pi m_{e(i)}}$ is electron (ion) the thermal velocity. Consequently electrons reach the particle surface at a greater rate, more electrons are collected, and the particle surface potential $\phi_d$ is thus negative. Ion and electron currents are affected by the dust surface potential. Thus, when it is repulsive for the species $j$, the current from the oppositely-charged plasma particles is favored which modifies, in proportion, the dust surface potential.

For particles with radius $a$ and for $a \ll \lambda_{e/i} \ll \lambda_{e(i)mfp}$, where $\lambda_{e(i)mfp}$ is the mean free path of electron/ion, the currents of the plasma species on the particle surface can be calculated using the orbital motion limited (OML) theory [61], [62].

Let us consider a plasma particle $j$ with velocity $v_j$ approaching the solid particle with radius $a$ from infinity. When the particle $j$ enters the Debye sphere of the solid particle, it experiences an electrostatic force, its trajectory gets affected and the velocity change to $v_j'$. From the fig. 2.1 it is clear that the impact parameter $b_j$ influences the outcome of this interaction. For the same velocity $v_j$ decreasing of $b_j$ leads to an impact of particle $j$ on the solid particle surface. Here the impact parameter $b_j$ is connected to the geometrical

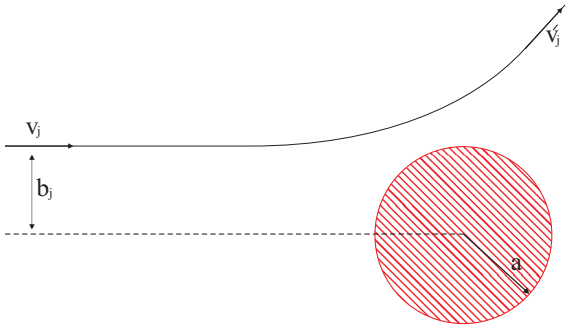


Figure 2.1: Schematic of interaction of a particle $j$ with a dust grains of the same charge.

collision cross section:

$$\sigma_j^d = \pi b_j^2 \tag{2.5}$$

For a solid particle with mass $m_d \gg m_i \gg m_e$ the equation of energy and momentum conservation for the interaction with particle $j$ has the form

$$m_j b_j v_j = m_j v_j^{'} a \tag{2.6}$$

$$\frac{1}{2} m_j v_j^2 = \frac{1}{2} m_j v_j^{'2} + \frac{q_j Q_d}{4\pi\epsilon_0 a} \tag{2.7}$$

where $m_j$ is the mass of $j$ particle and $q_j$ is its charge. The charge of the solid particle $Q_d$ is directly connected to the potential difference $\phi_{dif} = \phi_d - V_{pl}$ where $V_{pl}$ is the plasma potential. For a spherical particle where $\lambda_D \gg a$ the charge of the particle is $Q_d = C\phi_{dif}$ where $C = 4\pi\epsilon_0 a \exp(-a/\lambda_D) \approx 4\pi\epsilon_0 a$ is capacitance of spherical solid particle with $\lambda_d \gg a$. Combining the equations 2.5, 2.6, 2.7 the cross section can be written as

$$\sigma_j^d = \pi a^2 (1 - \frac{2 q_j \phi_d}{m_j v_j^2}) \tag{2.8}$$

For a velocity distribution function $f_j(v_j)$ of plasma species $j$ the current on the particle surface can be written as

$$I_j = q_j \int_{v_{jmin}}^{\infty} v_j \sigma_j^d f_j(v_j) d^3 v_j \tag{2.9}$$

Depending on the mutual charge of the plasma particle $j$ and the dust surface two cases must be considered. For $q_j\phi_d < 0$, the interaction between the plasma particle $j$ and the solid particle is attractive and the minimal velocity that particle $j$ requires to collide with dust surface, $v_{jmin}$, can be equal to 0. Where as for $q_j\phi_d > 0$, interaction is repulsive,

governed by equation $(1/2)m_j v_{jmin}^2 = q_j \phi_d$, and the particle needs a minimal velocity of $v_{jmin} = \sqrt{2q_j\phi_d/m_j}$ to overcome the potential difference from the charged solid particle.

For a Maxwellian plasma, the velocity distribution function is

$$f_j(v_j) = n_j(\frac{m_j}{2\pi k_B T_j})^{3/2} \exp(-\frac{m_j v_j^2}{2k_B T_j}) \tag{2.10}$$

where $n_j$ is the number density of $j$ species. Combining attractive and repulsive cases the currents to the particle surface have the following form, respectively:

$$I_j = 4\pi a^2 n_j q_j \left(\frac{k_B T_j}{2\pi m_j}\right)^{1/2} \left(1 - \frac{q_j\phi_d}{k_B T_j}\right) \tag{2.11}$$

$$I_j = 4\pi a^2 n_j q_j \left(\frac{k_B T_j}{2\pi m_j}\right)^{1/2} \exp\left(-\frac{q_j\phi_d}{k_B T_j}\right) \tag{2.12}$$

In the steady state case, the particle charge is constant and electron and ion currents, $I_e$ and $I_i$, compensate each other $I_e = I_i$. For most laboratory plasma where $T_e > T_i$ the dust potential upper limit is thus [30], [60], [63].

$$\phi_d = \frac{k_B T_e}{e} \ln\left(\frac{n_i}{n_e}\left(\frac{m_e T_e}{m_i T_i}\right)^{1/2}\right) \tag{2.13}$$

and the dust particle charge is

$$Q_d = \frac{4\pi\epsilon_0 a k_B T_e}{e} \ln\left(\frac{n_i}{n_e}\left(\frac{m_e T_e}{m_i T_i}\right)^{1/2}\right) \tag{2.14}$$

The maximum charge on an isolated dust particle in the simplest approximation is given by equation 2.14. Over the time, many different experimental and theoretical studies were done in order to extend this model and include more sophisticated plasma/particle interactions. It was thus shown that the most important process which influences the particles charge are ion - neutral collisions [64], [65], [66], [67], [68], [69].

## 2.2 Interaction of particles in complex plasmas

The interparticle interaction is one of the most fundamental property in complex plasmas. Understanding the underlying physics of the interaction is of great importance for explaining the observed phenomena in laboratory complex plasmas, astrophysical plasma, fusion reactors, plasma processing etc. In order to estimate the electrostatic force of the charged particles it is necessary to know the distribution of the electrostatic potential $U(r)$ in the plasma around the dust particle. The main point is that the interaction potential is not unique but strongly depend on the conditions of the background plasma. Here it should be mentioned that the interaction between dust particles is not only of electrostatic nature.

For the lower dust concentration the interparticle interaction can be considered within the approximation of an isolated particle.

The electrostatic force acting on a particle with a charge $Ze$ from another particle at a distance $r$ is presented in the form:

$$F_{int} = -\frac{dU(r)}{dr} \tag{2.15}$$

where $U(r)$ is the interaction potential.

One of the main interaction mechanisms is the electrostatic repulsion between like-charged particles. For small distances $r \ll \lambda_D$ the potential of an isolated particle is not affected by the ion screening and it can be considered to be of pure Coulomb form [70]. At the moderate distances $r \sim \lambda_D$ screening starts to affect and the Debye-Huckel potential can by used.

$$U(r) = \frac{Q}{r} exp(-r/\lambda_D) \tag{2.16}$$

At larger distances (several Debye length) absorption of ions on the particle surface results in a much slower decay of the potential, which scale as $\propto r^{-2}$. Here it is important to notice that previous evaluations are valid for collisionless, isotropic plasma where ion mean free path is much larger then Debye screening length, $\lambda_{imfp} \ll \lambda_D$. For collisional plasma, $\lambda_{imfp} \ll \lambda_D$, the ion-neutral collisions strongly affect the potential distribution around the particle resulting in even slower decay of the potential which scales as $\propto r^{-1}$ [71], [72].

One of the first experiments which determined the particle interaction potential was done by Konopka *et al.* [73]. This experiment was based on the analysis of elastic collision

between two particles. The interaction potential was reconstructed from the particles trajectories and velocities during the collisions by using the equation of motion.

Beside the electrostatic interaction, system of particles can experience forces caused by flow of plasma species on their surfaces. For a single grain in a isotropic plasma, ion and electron flows on its surface is spherically symmetric and there is no net momentum transfer from ions to a grain. For two grains separated by a distance smaller than the ion mean free path in isotropic collision-less plasma, the plasma flux on one grain is shadowed by the presence of other in its vicinity. This shadowing effect results in a difference in momentum transfer from plasma to grains where pressure is larger from outside of the grains than from inside. As outcome some attraction of particles can be expected. This effect was proposed by Ignatov *et al.* [74] followed by works of Tsytovich *et al.* [75] and Lampe *et al.* [76]. Theory predict that the shadow force can be dominant only for collision-less plasma at large interparticle distances $d \gg \lambda_D$ where the repulsive Coulomb field is screened and that attraction is proportional to the grain size.

Shadowing of the neighboring particle can result in an additional interaction associated with neutral atoms. If the temperature of the particle surface is different from the surrounding plasma, neutral atoms scattered from the particle surface will have energy distribution different from that of the ambient neutral gas [77]. This will result in net fluxes of energy and momentum between particle and gas. If two particles are located close to each other, an anisotropy in momentum flux on the particles will exert shadowing force between them. This force can be repulsive for temperature of particles higher then ambient gas and attractive in opposite case. This effect was first proposed by Tsytovich *et al.* [77].

However interactions governed by shadowing effect are only theoretical and, so far, there are no experimental confirmations. Possibility of experimental observation of this effects lies in microgravity experiments where big particles can be levitated in an isotropic plasma.

A separate type of interaction between particles is induced by the anisotropy of the background plasma. In the directional ion flow, the screening sphere around the particle becomes asymmetric. Streaming ions focus downstream from the grain creating positively space charge, a *wake*, which can attract with negatively charged neighbor particles. This additional particle-wake interaction makes the interparticle interaction non-reciprocal. The presence of wake breaks the symmetry in the interaction between the two charged grains,

making it non-Hamiltonian.

The wake effect is usually observed in ground experiments where particles are levitated in the plasma sheath above the lower electrode. In the work by Lampe *et al.* [76] it was calculated numerically that, for plasma conditions where $T_e/T_i \approx 25$ the decay of the wake potential behind the particle depends on the value of the Mach number. Experimental work of Melzer *et al.* [78] based on laser manipulation of particles confirmed the presence of non-reciporcal force between two particles. Two particles of different sizes were levitated one above the other in the plasma sheath of a low pressure rf discharge. Then radiation force created by a focussed laser beam was used to push the particles separately and observe the reaction of the other one. It was shown that the lower particle followed the motion of upper one and that the effect was not reciprocal.

Another type of anisotropic particle interaction was recently discovered in the presence of alternating uniaxial electric field [36]. Under this conditions the screening sphere around the charged particle is "smeared out" along the field axes and hence making the resulting potential symmetric. Ion oscillations was induced by applying alternating modulation to the existing rf field in the discharge. The frequency of the modulating electric field for these purpose has to be between dust plasma and ion plasma frequency. This kind of attractive potential consist of pure Debye-Hückel (particle-particle interaction) part and particle-wake interaction identical to the interaction between two equal and parallel dipoles. The "dipole" term of the interaction potential is responsible for the reciprocity of the anisotropic interaction between two particles. Increase of the alternating electric field increases the dipole-dipole attraction and particles arrange themselves into strongly coupled chains, sheets or crystalline structures. This type of interaction induced by external electric field puts complex plasmas in the group of electrorheological systems.

## 2.3 Forces

A particle immersed in the plasma is under the influence of many forces. On ground experiments gravity is always present. Collisions of ions and neutrals with the particle lead to considerable momentum transfer so that particle can fell an ion drag and a neutral drag force. An inhomogeneity in the plasma can create electric or pressure gradients which can influence the particle.

**The electric force**

Due to its charge the particles are subject to electric forces $F_e$ induced by electric fields in the plasma. The different mobility of electrons and ions leads to unequal space distributions of the charges in the plasma which lead to the appearance of an electric field. In capacitively coupled rf discharge due to the higher mobility of the electrons electric field is created in the sheath region which is strong enough to levitate micron size particles. Also due to the ambipolar diffusion the walls of the discharge chamber gets negatively charged and repel the particles. In general the electric force acting on a particle can be written as:

$$F_e = Q_d E \tag{2.17}$$

**Gravity force**

In any ground-based experiments, gravity plays an important role in the particle positioning in the discharge. For micron size particles the gravity force is of the same order of magnitude or even higher as other plasma induced forces so it can not be neglected. For smaller particles $a \ll 1\ \mu m$ gravity is negligible. This is the reason why nano particles occupy the whole volume of the discharge. For a spherical particle with mass density $\rho$ the gravity force is:

$$F_g = m_d g = \frac{4}{3}\pi\rho a^3 g \tag{2.18}$$

The gravity force can be the dominant force for micron size particle and can hide the influence of other more interesting interactions between particles so microgravity experiments are essential for more fundamental investigations of complex plasmas.

### Neutral drag force

This force is the result of collisions of solid particles with neutral gas atoms or molecules. It is the rate of momentum transfer between the neutral atoms/molecules and the solid particle during their collisions. It is therefore proportional to the gas pressure and particle velocity, which is usually much smaller than the thermal velocity of neutrals. The behavior of particles in the plasma with respect to neutrals can be expressed via Knudsen number as the ratio of atomic/molecular mean free path and particle radius $K_n = \lambda_{mfp}/a$. For large Knudsen number $K_n \gg 1$ the molecular regime is realized.

For a particle velocity $v_p$ and gas flow velocity $v_n$ the neutral drag force can be approximated by [79]

$$F_n \simeq n_n m_n \sigma_{nd} (v_d - v_n) \tag{2.19}$$

assuming the hard sphere interaction, elastic collision, between particles and the neutral gas atoms, where $n_n$ is the density of neutral atoms/molecules, $m_n$ their mass and $\sigma_{nd}$ the cross section of the dust neutral interaction.

More accurate expression is developed in case when relative velocity of dust and gas is very small in comparison with the neutral gas thermal velocity, $|v_d - v_n| \ll v_{Tn}$. In this case the neutral drag force can be approximated as a simple expression (so-called Epstein expression) [80]:

$$F_n = -\frac{4}{3}\pi a^2 n_n m_n v_{Tn} (v_d - v_n) \tag{2.20}$$

The letter is valid for specular collisions in which the neutrals colliding with the dust particle have their velocity components normal to the dust surface reversed after collision. In most practical situations neutrals are first absorbed at the particle surface and then re-emitted and this is diffuse reflection. In case for the perfect diffuse reflection the neutral drag force should be corrected in following way

$$F_n = -\frac{4}{3}\pi a^2 n_n m_n v_{Tn} \left(1 + \frac{\pi}{8}\right) (v_d - v_n) \tag{2.21}$$

For relative velocity $|v_d - v_n|$ very high in comparison with the neutral thermal velocity $v_{Th}$ (not experimentally achieved) the neutral drag force is proportional to the squared velocity and it is same for both the specular and perfect diffuse reflection [26]:

$$F_n = -\pi a^2 n_n m_n |v_d - v_n| (v_d - v_n) \tag{2.22}$$

For a Knudsen number $K_n \ll 1$, the system is in the hydrodynamic regime and the neutral drag can be evaluated like friction leading to the Stokes expression [81]

$$F_n = -6\pi\nu a v_d \tag{2.23}$$

where $\nu$ is the neutral gas viscosity.

**Ion drag force**

The ion drag force describes how momentum is transfered from the ions to the dust particles. Collisions of particles and ions is induced by an external electric field or simply by thermal motion of ions and particles. Momentum transfer is realized through inelastic collisions (absorption of ions by the particle surface) and elastic collisions (scattering of ions in the electric field of particle).

The ion drag force plays an important role in positioning of the particles in the discharge and the structural arrangement of particles in laboratory experiments [82], [29]. A variety of publications are dedicated to the ion drag force, observing its properties (direction and intensity) in the plasma, see for example [83], [84], [85], [86]. In other investigations this force is used to evaluate other properties in complex plasma systems, like charge of the particle in [67]. This force is responsible for low-frequency waves in complex plasmas [87], [88], voids on ground and microgravity experiments [89], [90] etc.

Analytical evaluation of ion drag to the particle is based on pair collision approximation for collisionless ions where $\lambda_{mfp} \gg r_{int}$ and isolated dust particle $d \gg r_{int}$, where $\lambda_{mfp}$ is main free path of ions, $r_{int}$ is characteristic distance of ion particle interaction and d is the average distance between particles. In general ion drag force can be expressed as:

$$F_i = m_i n_i \int v f_i(v) \sigma_i^{tr}(v) v dv \tag{2.24}$$

where $f_i(v)$ is the ion velocity distribution function, $\sigma_i^{tr}$ is the momentum transfer cross section for ion particle collisions depending on the ion velocity through the scattering parameter $\beta = U_0/mv_i^2\lambda_D$ where $U_0 = e|\varphi_s|aexp(a/\lambda_D)$ and $\lambda_D$ is effective screening lenght. For subthermal flows (ion flow velocity below thermal ion velocity, $u_i \leq v_{Ti}$) the thermal scattering parameter is used $\beta_T = e^2|Z|/\lambda_D T_i$.

In case of small Mach number ($M_T = u_i/v_{Ti} \ll 1$) and $\beta_T \leq 5$ the following expression for the ion drag force can be used [91]:

$$F_i = \frac{1}{3}\sqrt{\frac{2}{\pi}}\left(\frac{T_i}{e}\right)^2 \Lambda \beta_T^2 M_T \tag{2.25}$$

where

$$\Lambda(\beta_T) \simeq \int_0^\infty e^{-x} \ln(1 + 2x/\beta_T) dx \tag{2.26}$$

is the modified Coulomb logarithm integrated over the Maxwellian velocity distribution function. The screening length is equal to ion Debye length here. For larger scattering parameter $\beta_T$, investigated in [92] ion drag force have the following expression

$$F_i \simeq \frac{2}{3}\sqrt{\frac{2}{\pi}} \left(\frac{T_i}{e}\right)^2 \ln^2 \beta_T M_T \tag{2.27}$$

When $M_T \gg 1$ in equation for scattering parameter $\beta$ instead of ion thermal velocity $v_i$, drift velocity $u_i$ should be used.

**Thermophoretic force**

Solid particles suspended in the gas with a temperature gradient will be subjected to a force directed from the hot part to the cold part. The difference in momentum transfer from neutral gas to the particle from cold and hot part results in thermophoretic force towards the lower gas temperature. Then the thermophoretic force $F_{th}$ on a microparticle with the radius $a$ [93] is given as

$$F_{th} = -\frac{8}{3}\frac{a^2}{v_{th}} k_{tr} \nabla T_n \tag{2.28}$$

where $v_{th} = (8kT/\pi m)^{1/2}$ is the average thermal velocity of the gas atoms with mass $m$ at the gas temperature T and $k$ is a Boltzmann constant. $k_{tr}$ is the coefficient of heat conductivity and $\nabla T$ is temperature gradient.

Thermal conductivity for monoatomic gases can be found in the literature [94] in the form

$$k_{tr} = 2.4\frac{\eta c}{m} \tag{2.29}$$

where $c = 3k/2$ is the specific heat per atom and $\eta$ the shear viscosity of the gas. Viscosity was derived from the precise solution of the transport problem in the case of hard sphere [95]

$$\eta = 0.553\frac{\sqrt{mkT}}{\sigma} \tag{2.30}$$

with the gas cross section $\sigma$ for atomic scattering, which can be found in the literature [96], [93]. The main parameters, like gas-kinetic atom-atom cross section, viscosity, heat

conductivity for different noble gases can be found in the [93]. Combining the equations 2.28, 2.29 and 2.30 gives the equation of the thermophoretic force

$$F_{th} = -3.33\frac{ka^2}{\sigma}\nabla T \tag{2.31}$$

A large number of publications is devoted to thermophoresis. It is commonly used for particle levitation [93]. Compensating the gravity by thermophoresis in an rf parallel plate plasmas results in presence of particles in central/bulk plasma so that the creation of a void can be observed and investigated on ground experiments. For example, for a melamine formaldehyde spherical particle of radius $a = 1.46$ $\mu$m and density $\rho = 1.51$ $g/cm^3$, a temperature gradient of 4.65 $K/cm$ is required to compensate gravity in neon [97]. This temperature gradient is easily reachable in case of narrow gap (few $cm$). A lot of phenomena are induced by a thermal gradient in the discharge. Most of these investigations were done in a parallel plate discharge where a uniform heating or cooling of the electrodes is possible. With precise manipulations, many different thermally induced effects can be observed, like bubbles, eruptions [98], convections [97], [99], structures [100] and particle levitations [93].

A temperature gradient in plasma can occur by difference in temperature of some parts of the discharge chamber (heating of vacuum pump) or by an inhomogeneous ionization (Ohm heating).

## 2.4 Structures

Under the influence of a background plasma microparticles introduced into the plasma can selforganize in various ways. Differences in selforganization are induced by interparticle interaction and mobility. When dust particles have high kinetic energies, they are in a gaseous state. By "cooling" it down, the microparticles system starts to self-arange and liquify until the particles crystalize.

In the gaseous state particles have higher kinetic energies and lower level of order. When liquifying the particle cloud, electrostatic interactions overcome their kinetic energy and particles arrange towards a *hcp* lattice structures while more crystalized structures arrange in $fcc$ lattice types.

The structural analysis plays a very important role in the characterization of complex plasmas. There are many examples where changing the self-organization of microstructures influence mechanical and optical properties of materials. By detailed reconstruction of

particles positions and their correlation with neighboring particles the local order can be evaluated observing the coupling parameter, pair correlation function or by comparison with different ideal lattice types.

### 2.4.1 Coupling parameter $\Gamma$

One of the fundamental parameters of large systems of dust particles is the coupling parameter $\Gamma$. It is the ratio of the potential energy of the interaction between two particles to their kinetic energy. For a simple Coulomb interaction between the particles,

$$\Gamma = \frac{Z^2 e^2}{dT_d} \tag{2.32}$$

where $d \cong n_d^{-1/3}$ is the characteristic average interparticle spacing with number density $n_d$ of the particles and $T_d$ characterizes their kinetic energy.

For the Yukawa interaction the screening of the particles by the surrounding plasma modifies the coupling ratio by a factor $\exp(-k)$ where $k = d/\lambda_d$ is the structure (or lattice) parameter - the interparticle spacing normalized by the effective screening length, leading to

$$\Gamma = \frac{Z^2 e^2}{dT_d} \exp(-d/\lambda_d) \tag{2.33}$$

Depending on the value of $\Gamma$, the system can be strongly or weakly coupled. Usually there are strongly coupled systems if $\Gamma \geq 1$.

There are plenty numerical works devoted to the resolving of the phase of the systems characterizing it with two independent dimensionless parameters $\Gamma$ and $k = d/\lambda_d$. Different phases and possible lattice types are presented in $(\Gamma, k)$ plane summarizing available numerical results. The phase diagram of the Debye-Hückel system is presented in figure 2.2 obtained by numerical modeling [101]. Three different phases were found depending on the values of coupling and structure parameters. For $\Gamma$ above the melting curve two solid phases are found, *bcc* for small $k$ and $fcc$ for bigger $k$ and fluid phase for $\Gamma$ below melting curve.

Another interesting correlation can be made from the number of particles with 6 neighbors and the coupling parameter. By calculating the percentage of particles with 6 nearest neighbors $N_6$ from $N$ particles in the system preliminary estimations of coupling parameter can be made [102]. Figure 2.3 shows the dependence of $N_6/N$ on $\Gamma$ for different types of confinement from [102].

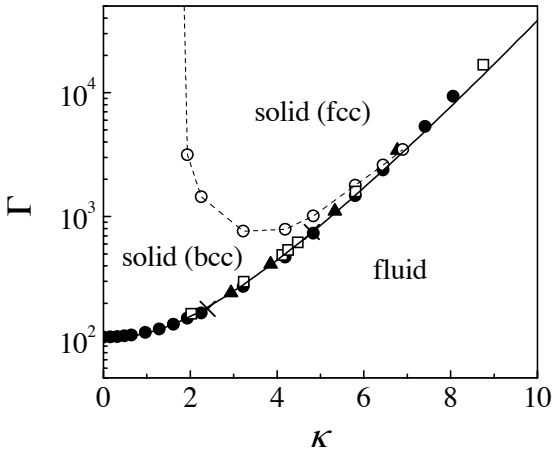


Figure 2.2: Phase diagram of Debye-Hückel systems, obtained from numerical modelling.

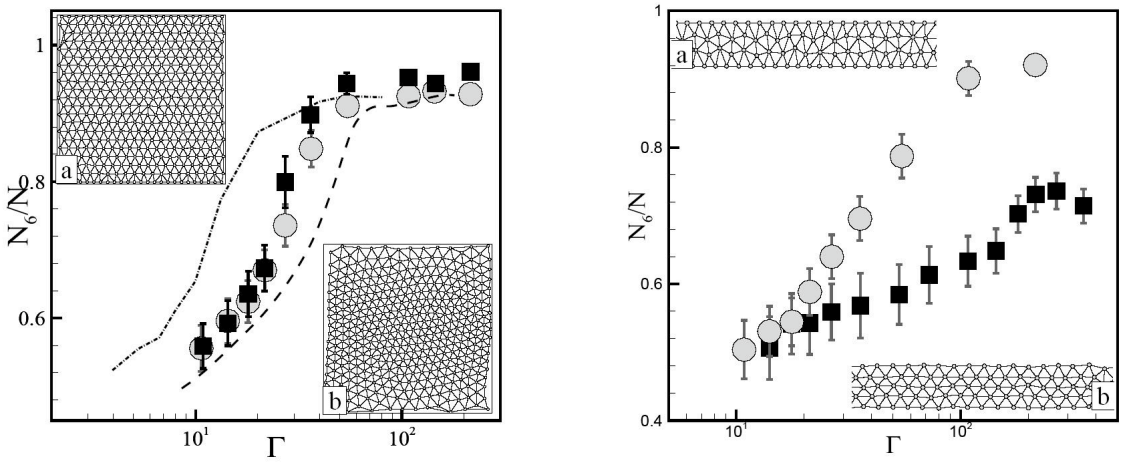


Figure 2.3: Relative number of microparticles $N_6/N$ that have six neighbors (6-fold cells) vs. the coupling parameter $\Gamma$ for different types of confinements presented in insets (a) for potential-well and (b) for parabolic confinement.

### 2.4.2 Pair correlation function - g(r)

The structural analysis of the systems of particles in the plasma starts with a studies of single layers of particles. In this case fast and simple information of the interparticle separation could be extracted by calculating the pair correlation function $g(r)$.

The pair correlation function presents the probability of finding two particles separated

by distance $r$, and it measures the translational order in the system.

$$g(r) = \frac{1}{N} \sum_{i=0}^{N} \sum_{j=0}^{N_j} \delta |r_i - r_j| / N_j \tag{2.34}$$

where $r_i$ and $r_j$ are the coordinates of two particles separated by distance $r + \Delta r$, $\Delta r$ is a bin thickness and $N_j$ is the number of particles in the bin. An example of $g(r)$ for different $\Gamma$ is presented in figure 2.4. The position of the first peak corresponds to the particle separation.

There are many publications where pair correlation function is used for structural characterization of the system [103], [104], [105], [102].

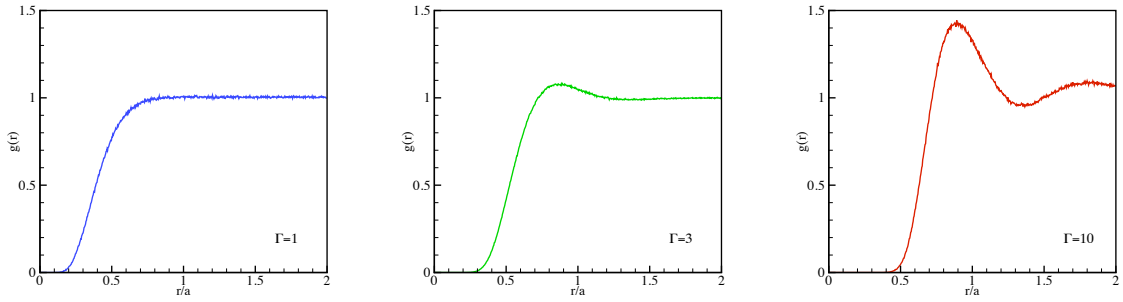


Figure 2.4: Pair correlation factor, g(r), for different coupling parameters.

### 2.4.3 Local Order Analysis

For a detailed characterization of the system in an ordered state, a much more precise method for the structural analysis should be used. In a liquid or crystal phase, particles have well defined positions creating different lattice types. In these states the method should evaluate the position of each particle with respect to its nearest neighbors and compare this results with ideal lattice types.

To determine the local order of the particles a bond order parameter method is used [106]. In the framework of this method, the local rotational invariants for each particle are calculated and compared with those for perfect lattice types like $fcc/hcp/bcc/ico$ (see Fig. 2.5).

Local rotational invariants of second order $q_l(i)$ and third order $w_l(i)$ are calculated for

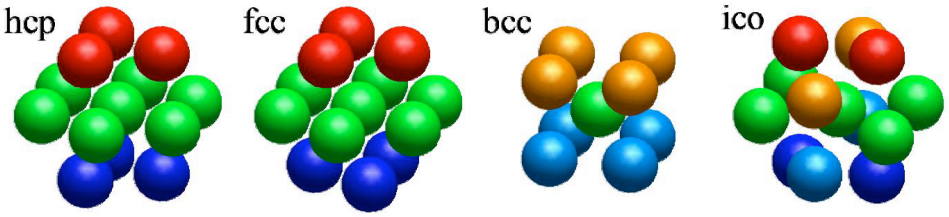


Figure 2.5: Different types of lattice structures commonly found in complex plasma systems.

each particle $i$ by using $M$ nearest neighbors $N_b(i)$:

$$q_l(i) = \left( \frac{4\pi}{(2l+1)} \sum_{m=-l}^{m=l} \mid q_{lm}(i)|^2 \right)^{1/2} \tag{2.35}$$

$$w_l(i) = \sum_{\substack{m_1,m_2,m_3 \\ m_1+m_2+m_3=0}} \begin{bmatrix} l & l & l \\ m_1 & m_2 & m_3 \end{bmatrix} q_{lm_1}(i) q_{lm_2}(i) q_{lm_3}(i), \tag{2.36}$$

where

$$q_{lm}(i) = \frac{1}{N_b(i)} \sum_{j=1}^{N_b(i)} Y_{lm}(r_{ij}) \tag{2.37}$$

and $Y_{lm}$ - are the spherical harmonics, $r_{ij} = r_i - r_j$, where $r_i$ are the coordinates of $i$-th particle. In equation (2.36) $\begin{bmatrix} l & l & l \\ m_1 & m_2 & m_3 \end{bmatrix}$ are the Wigner $3j$-symbols, and the summation in the latter expression is performed over all indices $m_i = -l, ..., l$, that satisfy the condition: $m_1 + m_2 + m_3 = 0$.

It is important to stress that each lattice type has its own unique set of $q_l$ $w_l$ rotational invariants. It give us a possibility to identify observed lattice types, by comparing the observed $q_l$, $w_l$ values with those $q_l^{\mathrm{id}}$, $w_l^{\mathrm{id}}$ for a perfect lattice.

To define the local order around a particle we used $q_4$, $q_6$, $w_4$ rotational invariants. The rotational invariants can easily be calculated for perfect fcc/hcp/ico/bcc. For fcc/hcp/ico the number of nearest neighbors $N_b = 12$ and we have for fcc: $q_4^{\mathrm{fcc}} = 0.1909$, $q_6^{\mathrm{fcc}} = 0.5745$, $w_4^{\mathrm{fcc}} = -0.1593$ $w_6^{\mathrm{fcc}} = -0.01316$; for hcp: $q_4^{\mathrm{hcp}} = 0.0972$, $q_6^{\mathrm{hcp}} = 0.4847$, $w_4^{\mathrm{hcp}} = 0.1341$, $w_6^{\mathrm{hcp}} = -0.01244$ and for icosahedral lattice type (ico): $q_4^{\mathrm{ico}} = 0$, $q_6^{\mathrm{ico}} = 0.6633$, $w_4^{\mathrm{ico}} = -0.1593$, $w_6^{\mathrm{ico}} = -0.1697$ respectively.

For the bcc case $N_b = 8$ and $q_4^{\mathrm{sc}} = 0.5092$, $q_6^{\mathrm{sc}} = 0.6285$, $w_4^{\mathrm{sc}} = -0.1593$, $w_6^{\mathrm{sc}} = 0.1316$. To identify bcc clusters it is sometimes important to know the position of the second shell having 6 particles (the distance between the nearest-neighbor and the second shells in the bcc lattice is $(2/\sqrt{3} - 1)\Delta \simeq 0.15\Delta$). In that case $N_b = 14$ $q_4^{\mathrm{bcc}} = 0.0363$, $q_6^{\mathrm{bcc}} = 0.510$, $w_4^{\mathrm{bcc}} = 0.1593$, $w_6^{\mathrm{bcc}} = 0.01316$.

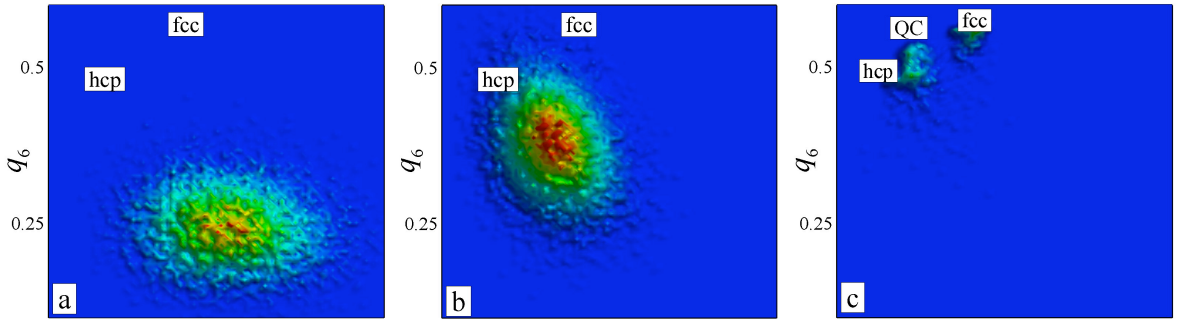


Figure 2.6: Local order analysis for characteristic phases in the process of crystallization. From liquid like (far left), glassy (middle) to crystal phase of particle cloud (right).

In figure 2.6 a local order analysis is performed in different moments of crystallization of the particle cloud [107]. The first picture represents the local order for the particles in the gaseous phase. The second picture shows an already cooled system which is in a liquid like or glassy state where we see that the arrangement goes towards the *hcp* lattice type. In the last snapshot, the particles already have well defined local order divided into two lattice types *hcp* and $fcc$.

## 2.5 Optical emission spectroscopy

In this section an elementary introduction about plasma spectroscopy will be presented. Plasma spectroscopy is a powerful tool for plasma diagnostics. Spectroscopic diagnostics is specially useful for complex plasmas as non-destructive method in contrast to Langmuir probes. By simply observing the emission spectrum of the gas discharge, one can reveal information of the purity of the gas. Many methods and models were developed to analyze emission spectra in order to reveal plasma parameters. In order to use emission spectroscopy for complex plasma evaluation, some accommodations to existing models for pure plasma should be done, taking into account the interaction of plasma glow with particles.

### 2.5.1 Elementary introduction

Plasma spectroscopy was intensively studied for the last few decades. Consequently there are a big number of processes and phenomena connected to this field. Nobel gases are inert and monoatomic in most cases so the number of plasma components involved in processes of plasma light emission is limited. In this section, only elementary processes relevant for the further understanding of the thesis will be described.

The starting point in all spectroscopic evaluations deals with the excitation of some upper states of neutral gas atoms and its spontaneous emission. Light intensity $I_{ij}$ emitted from some upper level $i$ to level $j$ is given by:

$$I_{ij} = A_{ij} h\nu_{ij} N n_e k_{gi} \tag{2.38}$$

where $A_{ij}$ is the Einstein coefficient for spontaneous emission for $i \rightarrow j$ transition, $h\nu_{ij}$ the elementary energy of light with frequency $\nu_{ij}$, $N$ is the neutral density, $n_e$ is the electron density and $k_{gi}$ is the rate coefficient of the population of the upper state from the ground level. The population of the upper state $i$ can be done through different channels. For the excitation from the ground state the rate coefficient can be expressed as:

$$k_{gi} = \int v\sigma_{gs}(v) f(v) dv \tag{2.39}$$

where $f(v)$ is the electron energy distribution function (EEDF) and $\sigma_{gs}(v)$ is the excitation crossection from ground state to upper level $i$ which depends on the electron temperature. Combining (2.38) and (2.39) a simple equation for light intensity emission can be obtained. It corresponds to a simple model where state $i$ is populated only by collision of electrons and gas atoms in ground states and no excitation from other levels is included. Many publications proposed models [108], [109], [110] for plasma evaluation are based on this simplified approach.

In reality, population of some excited state includes all possible channels of excitation, through metastable and resonant levels and cascading from higher levels. Summarizing the population of state $i$ from all this different channels is not a simple task due to the big number of possibilities and insufficient informations about cross sections (for example see [111]).

Another improvement in describing the processes of population of some state can be made using the optical cross section instead of the excitation cross section [112], [113].

Optical cross sections, are strictly connected to the observed transitions and levels from which the excitation are made. It includes all the possible channels for population of the upper level and Einstein coefficients.

Using the optical cross sections the equation for light emission now can be rewritten as:

$$I_{ij} = h\nu_{ij} n_e \sum_s n_s k_{ij}^s \tag{2.40}$$

where $n_s$ represent the population of the level $s$ from which the excitation to level $i$ is made (ground state and metastable states) and $k_s$ is the emission rate coefficients for the corresponding level $s$. The value $k_s$ is then defined as:

$$k_{ij}^s = \int v\sigma_{ij}^s(v) f(v) dv \tag{2.41}$$

The most common plasma diagnostics based on optical emission spectroscopy (OES) deals with ratio of line intensities as a function of electron temperature. The selection of spectral lines used for this method strongly depends on the type of gas with the general rule to use lines which excitation energies of upper levels that are quite different. A general overview of this method can be found in [114]. There are other methods for plasma diagnostics beside OES which are however based on a detailed knowledge of plasma spectroscopy. Some common methods are laser induced fluorescence (LIF) for the evaluation of the number density of the population of states and tunable diode laser absorption spectroscopy for the measurement of the population of metastable levels.

### 2.5.2 Spectroscopy and Complex Plasmas

There are not many experimental works which use spectroscopy to characterize complex plasmas. In [115] a simple Corona model is used to evaluate changes of the electron temperature due to the particle injection. Recent work [116] used plasma emission changes induced by different sizes of particles to characterize the influence of the dust on discharge properties. The most common quantities estimated by means of plasma spectroscopy are the metastable density by measuring self-absorption of relevant spectra lines propagating through the plasma [20], [117], [118], [119].

In the previously mentioned publications, methods developed for dust-free plasma are used to evaluate complex plasma parameters. However, experiments and theories predict that models build for a pristine plasma should be used carefully in the case of a complex

plasma. Particle in the discharge, beside disturbing the ionization balance due to the charging, can interact with the plasma light and hence change the background plasma conditions.

Plasma light can interact with the particles by Mie scattering and change the intensity of the escaped light from the discharge [119], [120]. It means that measured light emission emitted from a discharge can not be directly used in the models and a correction for the extinction of light by microparticles is needed [119].

Small wavelength emission in a plasma, specially in the UV and VUV range, have energies high enough to cause a photoemission effect from the particle surface [121]. This mechanism is the dominant dust-charge process on the lunar sunlit environment leading to levitation and transportation of dust on the lunar surface [122], [123]. Similar to this, light can cause photodetachment of electron from the charged particle surface [27] which can also influence particle charge and background plasma.

The measurement of metastable density variations in the presence of particles is presented in a few publications [20], [117], [118], [119]. Depending on the plasma parameters and the size of particles these changes are different. In the case of nanosize grown particles in the plasma an increase of the metastable density is measured [20]. With larger particles introduced in the plasma the metastable density seems to decrease[117] (increase[119]). Non consistent changes in these two cases gives no possibility for building a unique theory which will explain the underlying physics.

Collisions of metastables with particles can result in the ejection of electrons from the particle surface based on the tunneling effect of an excited atom from the metastable state to the valence band in the particle surface followed by ejection of an electron [124], [125], [126]. The probability of electron ejection due to this effect is almost equal to the unit for metal surfaces while for insulators there are no reliable informations. The method for qualitative surface evaluation on atomic level based on this interaction is called Metastable-atom Deexcitation Spectroscopy (MDS). The energy of the ejected electron depends on the work function of the surface material and the energy level of the excited electron in the metastable state. For example, interaction of a clean Pb surface with the metastable atom of He (Ne) can result in the ejection of electrons with energies of about 8 $eV$ (5 $eV$) [127].

# Chapter 3

# Experimental Setup

There are many different setups for experimental investigations of complex plasmas. For example, in MPE there about 10 different setups built for different experiments in complex plasmas. All these setups are different in size, driven power, pressure range and plenty of other details. The reason for this variety lies in the purpose of the investigation.

## 3.1 Evolution of the setup: History of Complex Plasmas, Different setups, Microgravity experiments

In this chapter, an elementary introduction to the experimental setups relevant for this thesis will be described. The experiments presented in this work are done in two different setups, Plasma Crystal 3 Plus (PK-3 Plus) and Plasma Crystal 4 (PK-4). These two experimental setups are the logical successors of the Plasma Crystal 1 and 2 and PKE Nefedov experimental setups.

PK1 and PK2 were setups designed for complex plasma experiments under microgravity on the Russian Orbital Station MIR. The PKE Nefedov setup was the first scientific experiment done on board of the International Space Station (ISS) from 2001 to 2005. The experimental module consists of an Experimental Block and the so-called Telescience Unit used for controlling and recording the experiment. For more details about this setup see [128]. After 45 successful experiments done with this setup during this time there were plenty of ideas for improvement for its substitute on the ISS: PK-3 Plus.

The next generation of a complex plasma experimental setup, PK-4, will hopefully be

launched in 2012. This is a fundamentally different setup from all its precursors. In PK-4 a DC or low frequency discharge within a glass tube is dedicated to different investigations, mainly fluid dynamics and fluid properties of complex plasmas.

In parallel to the microgravity modules there are exact copies of the experimental setups on ground used for preparing new experiments. In the next two sections the PK-3 Plus and PK-4 setups for ground-based experiments will be described in more details.

## 3.2 Plasma Crystal 3 Plus, PK-3 Plus

The PK-3 Plus chamber is a parallel plate rf discharge. The electrodes are round shaped with a diameter of 6 *cm* made from aluminum. The distance between the electrodes is 3 *cm*. On both electrodes there is a metal (guard) ring which under ground voltage confines the plasma and hence also the particles in radial direction towards the center of discharge. The discharge reactor is a square vacuum chamber with a size of 10×10 $cm^2$ and a hight of 5.4 *cm*. The walls are made of quartz glass with high transparency for visible light. A sketch and cross section of the setup are presented in figure 3.1.

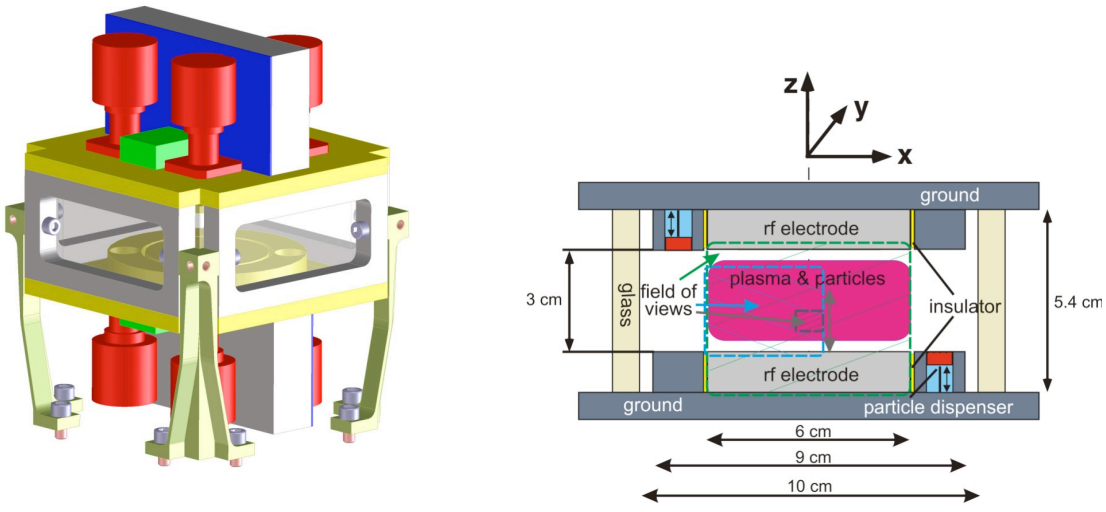


Figure 3.1: Sketch (left) and cross section (right) of the PK-3 Plus experimental setup.

On the top of the chamber there is a vacuum flange for the connection to the vacuum system consisting of a membrane pump for pre-vacuum (minimum pressure 5 *mbar*) and a turbo-molecular pump for high vacuum $< 10^{-5}$ mbar. After every opening the chamber is

usually pumped for one day to reach high vacuum and to guarantee a clean environment for the experiments. For gas injection gas bottles are connected to the chamber through a system of valves and controllers. During the experiments gas is injected into the chamber in cycles controlled by software in order to avoid gas degradation. Depending on the experimental conditions the usual refreshing cycle interval is a couple of ten seconds. Direct gas injection would result in a disturbance of the particles. Therefore the gas is injected into the dead volume of approximately 1 $mm^3$ and from there diffuses slowly into the chamber through a small narrow tube.

Particle injection in the chamber is done by particle dispensers. There is the possibility for attaching 6 mechanical particle dispensers with a software controlled intensity and number of shakes. in this way there is the possibility for roughly controlling the number of the particles per injection.

The plasma is ignited by an rf generator (frequency 13.56 MHz) capacitively coupled to the electrodes with maximum power of 4 W. Most of the experiments are run of low power below 1 W. In order to manipulate particles an additional function generator is coupled to the electrodes which can run in DC or AC mode with a maximum output of $\pm 50V$ to each electrode. In AC mode different shapes of the signals can be used (sinusoidal, square...).

In the experiments performed in laboratories the particles sediment to the lower electrode due to the gravity force. In order to compensate gravity and arrange the particles to fill the whole chamber, which is essential for many experiments, the thermophoretic force can be used. In order to create a temperature gradient between electrodes a system of resistors and fans is used. Resistors are evenly distributed on the bottom electrode while two small fans are used to cool the top electrode. In this way a temperature difference of about 70 ° K between the electrodes can be achieved.

For particle visualization a system of laser and camera is attached to a holder on the side of the chamber. The particles scatter the laser light which is recorded by camera under the angle of 90 degree. In PK-3 Plus chamber a 532 $nm$ laser of 200 mW power is used, where the beam is spread into a sheet of about 140 $\mu m$ thickness. In this way the whole vertical cross section of the chamber can be illuminated and recorded with the camera. In order to record fast motion of the particles a CCD camera must be used together with a system of adequate lenses. In this setup for a typical field of view of 30x30 $mm^2$ up to 1000 frames per second can be achieved. Higher frame-rates (up to 3000 fps) can be achieved by decreasing the field of view. On top of the lenses, a filter of the wavelength

of the illumination laser is attached in order to avoid light from the discharge to interfere with illumination light scattered from the particles. The positioning of the laser/camera holder is done by a software controlled step motor which give the possibility for full space resolved particle observation by scanning through the particle cloud. Using this system allows to achieve very precise 3D reconstruction of the particle cloud in the plasma.

This kind of discharge chamber is suitable for various types of experiments. Most common experiments concerns particle crystallization and melting, temperature induced gas dynamics, waves, self-induced instabilities etc. The possibility to inject large number of particles and fill a large fraction of the chamber is useful for spectroscopic observation of the influence of particles on the plasma parameters [115], [119] .

## 3.3 Plasma Crystal 4, PK-4

The PK-4 setup contains a different type of chamber compared to all its precursors. The PK-4 type of chamber design is mainly thought for the observation of fluid like properties of complex plasmas. The heart of the setup is "U" shaped discharge glass tube as sketched in figure 3.2. The tube is overall 750 *mm* long with 30 *mm* inner diameter and DC electrodes on both sides. The main experimental part of the tube, the positive column of the discharge is 350 *mm* long with flat windows at the sides for optical illumination. The system is mounted on a vertical plate with the possibility of changing the orientation with respect to gravity from vertical to horizontal, depending on the needs of the experiments.

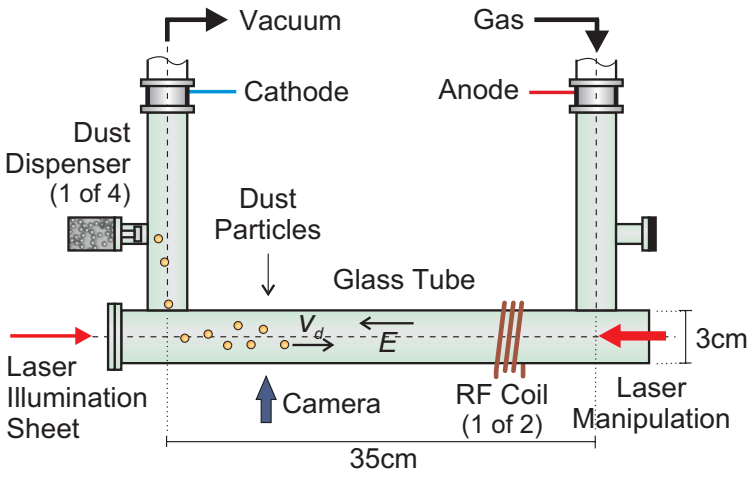


Figure 3.2: Sketch of PK-4 experimental setup.

One end of the discharge tube is connected to a system of vacuum pumps, pressure controllers and valves while the other end to a system for gas injection through the flow controller as it is shown in figure 3.2. The evacuation of the tube is done by two pumps. Pre-vacuum of about 5 $mbar$ is created by a membrane pump while higher vacuum about $10^{-5}$ $mbar$ is reached by a turbo-molecular pump. To ensure stable plasma conditions over longer time of the discharge, the plasma can be refreshed by continuous gas flow. In vertical configuration continuous gas flow can be used also for particle levitation and manipulation.

This system was first developed as a pure DC discharge. Later on the power supply was upgraded with few additional possibilities. In the latest configuration the plasma can be created as pure DC or low frequency discharge (polarity switching) up to a few $kHz$. In the polarity switching mode one of the electrode is grounded and the other changes the sign of the voltage with an adjustable frequency. The polarity switching duty cycle can be changed in order to create a net electric field in the plasma. The discharge is current limited with a maximum of 3 $mA$. The voltage difference on the electrodes depends mainly on the pressure and can be from a couple of hundreds volts to about 3 $kV$. In addition to the main power supply the plasma can be created locally by an rf coil mounted around the tube. This provides the possibility to create a plasma using both DC (or low frequency) and rf combination. The rf mode can be run with a frequency of 13.56 MHz or 81.36 MHz.

The discharge tube is designed with the possibility to attach 6 particle dispensers. The intensity and number of shakes can be controlled which ensures a rough control of number of particles injected with each shake.

This configuration of the discharge is suitable for different types of manipulation of the particles. For example, the previous mentioned rf coil can be used for particle trapping. Thermophoretic force can be easily obtained by using a heating coil around the tube. Creating a temperature gradient can lead to additional gas convection inside the discharge which lead to particle motion (see below section 4.2.). Also it is possible to integrate additional electrodes in the tube and to push or attract particles by applying a voltage to it. Particle manipulation can be done also by using a manipulation laser introduced along the tube or from the side in radial direction. For this purpose a 20 W infrared diode laser is installed.

For particle visualization a system of illumination laser and camera is installed on an translation stage of the side of the tube. The laser is directed along the tube which enables

the illumination of the particles along the whole positive column. For these purpose a small power 10 mW red (683 nm) laser spread into a sheet is used. The thickness of the laser sheet is about 150 $\mu$m. The camera is attached to the same holder perpendicular to the laser with the possibility to move it along the whole main part of the tube. The frequency of recording with a typical 30x30 mm$^2$ field of view is 60 frames per second. The whole holder can be moved precisely manually or by step motor. Using the step motor with an adjustable velocity is suitable for 3D scanning of the particle cloud. In this way a 3D reconstruction of the particle positions and velocity distributions can be done [58] (see sect. 4.1.).

The PK-4 experimental setup is mainly designed for investigating the particle dynamics although stable structures can be observed. In the horizontal orientation of the tube the levitation of the particles is done by the plasma sheath above the glass wall which imposes a strong limitation on the particle size that can be used in the experiments ($a \leq 7$ $\mu$m). In this orientation it is possible to observe the particles in steady state without intensive motion using the polarity switching. In the vertical orientation the particles can be levitated by various forces depending on the desired effect. Gravity can be compensated by neutral gas flow, electric force, combination of thermophoretic force and induced convections, in an electric field created inside of striations. Except for the last method all others lead to a strong motion of the particles so there is no possibility for observing steady structures or crystallization.

# Chapter 4

# Cumulative thesis

This cumulative thesis consists of the following papers

1. S. Mitić, B. A. Klumov, U. Konopka, M. H. Thoma and G. E. Morfill, Structural Properties of Complex Plasmas in a Homogeneous Discharge, Phys. Rev. Lett. **101**, 125002 (2008).

2. S. Mitić, R. Sütterlin, A. V. Ivlev, H. Höfner, M. H. Thoma, S. Zhdanov and G. E. Morfill, Convective Dust Clouds Driven by Thermal Creep in a Complex Plasma, Phys. Rev. Lett. **101**, 235001 2008.

3. S. Mitić, M. Y. Pustylnik and G. E. Morfill, Spectroscopic Evaluation of the Effect of the Microparticles on Radiofrequency Argon Plasma, New Journal of Phys., **11**, 083020, 2009

4. S. Mitić, B. A. Klumov, M. Y. Pustylnik and G. E. Morfill, Determination of Electron Temperature in Low-pressure Plasmas by Means of Optical Emission Spectroscopy, JETP Lett. **11**, *5*, 249-253, 2010

The main ideas and results of these papers (1) to (4) are summarized in sections 4.1 to 4.4, respectively.

## 4.1 Structural Properties of Complex Plasmas in a Homogeneous Discharge

### 4.1.1 Objectives

The main objective of this work is to present a full 3D reconstruction and the local order analysis of a microparticle cloud in a homogeneous DC discharge. For this reason a cloud of microparticles confined in the horizontally oriented "PK-4" laboratory setup was observed. The local order analysis of the experimentally observed microparticles structures was compared with the molecular dynamic (MD) simulation.

### 4.1.2 Experiment and methods

The experiment was done in PK-4 laboratory setup with melamine formaldehyde spherical particles of 2.55 $\mu$m diameter in a neon plasma on 30 $Pa$. Particles were confined in a horizontally mounted discharge tube levitated by the radial electric field of the plasma sheath above the tube walls [97]. Since highly charged particles introduced into the positive column of the DC discharge strongly react with the electric field no steady state conditions can be reached in homogeneous DC discharge (see sect. 3.3.). In order to compensate the effect of the longitudinal electric field on the particles in the plasma, the polarity of the voltage between the electrodes was switched with a frequency above the response frequency of the particles (above 100 Hz).

Particles were injected from the side of the discharge and slowly drift to the center of the positive column of the discharge tube. After some time (approximately 10 minutes) scanning was performed using the step motor (for more details about the experimental setup see chapter 3.3).

For the further analysis a molecular dynamic simulation based on a Coulomb (Yukawa) type of interaction was done for the conditions of the experiment, geometry, confinement, particles charge, size and density, neutral gas density etc. The system of equations

$$m\ddot{\mathbf{r}}_i = -Z_{\mathrm{d}} \sum \nabla\phi - m\gamma\dot{\mathbf{r}}_i - m\mathbf{g} + \mathbf{L}_i \tag{4.1}$$

was solved for each particle involving all knowing forces acting on particle including, electrostatic, Epstein friction, gravity and stochastic Langevin force (thermal noise) respectively (terms on right hand side of the equation).

The lattice arrangements observed in the experiment were compared with the one from the numerical simulation using the local order analysis (see chapter 2.4.3).

### 4.1.3 Results

The three-dimensional positions of the particles in the observed part of the cloud (right) together with the snapshot of particles positions from the MD simulation (left) are presented in figure 4.1. Particle positions are overlapped for all microspheres in the cloud showing the projection of the system as side view and top view (upper and lower image in the fig 4.1 left). About 6000 particles are detected.

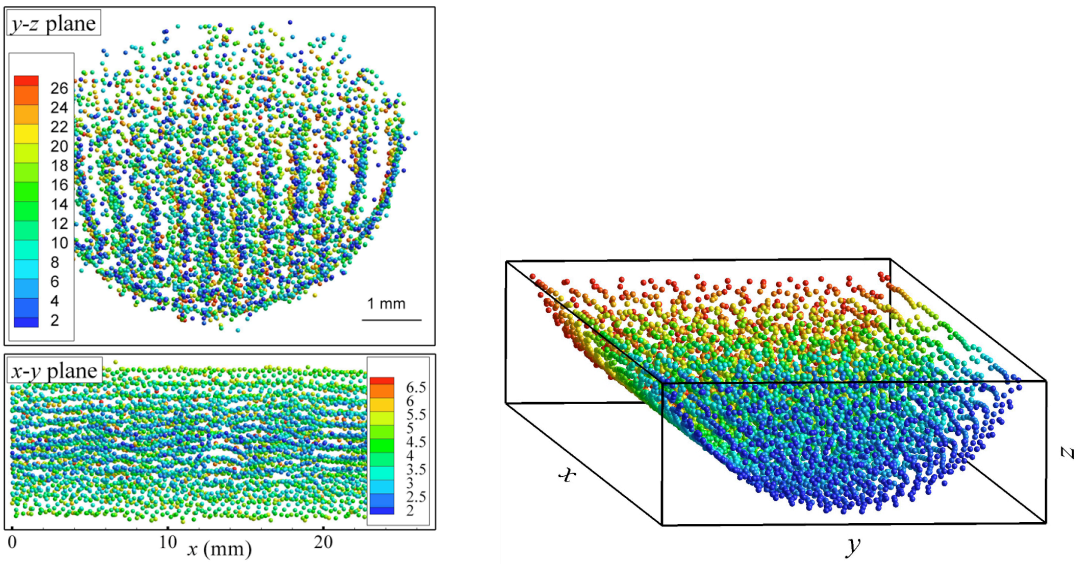


Figure 4.1: Left: Experimentally recorded particle positions. Particle are color-coded by corresponding third coordinate presented in millimeters. Right: MD simulation of the Yukawa system of the dust particles. Snapshot of the particle positions in the steady-state stage for a coupling $\Gamma \simeq 10$.

As it is visible from figure 4.1, the overall shape of the particle cloud is defined by the shape of the confinement. From the first look a few interesting (macro) structural properties can be noticed. The particles in the bulk of the cloud represent a kind of vertically oriented structure. These vertical structures are not so pronounced in the lower part of the particle cloud where particles self arrangement is disturbed by confinement and pressure from upper particles. There is a distinct outer particle layer that represent the

structure of the radial confinement across the discharge tube. In the top of the cloud, close to the center of the tube, the particles do not exhibit high structural arrangement.

The local order analysis of the experimentally observed system of particles was compared with the local order of simulated system in different stages of coupling. The results are presented in figure 4.2. The local order analysis of the simulated system is presented in the figure 4.2 for two different values of coupling parameter $\Gamma \simeq 1$ and $\Gamma \simeq 10^4$, area (b) and (a) respectively. Experimental results are over-plotted and distributed within the area (c) reviling the liquidlike behavior. It was found that the local order of the experimentally observed system of particles corresponds to the coupling of $\Gamma \simeq 10$ of the simulated system.

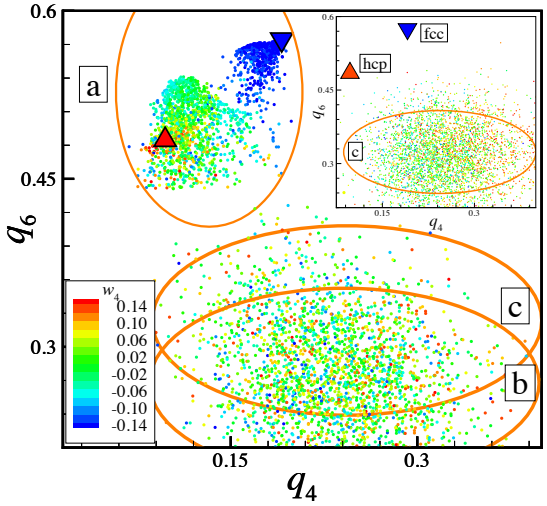


Figure 4.2: Distribution of dust particles at different values of $\Gamma$ in the plane of local order parameters $q_4 - q_6$ (calculated by using 12 nearest neighbors) as seen from MD simulations of Yukawa systems of particles together with experimental data. Scattered data are color-coded by third order rotational invariant $w_4$ value. Data for ideal hcp ($\triangle$) and fcc ($\nabla$) are also plotted. Distribution (b) shows a liquid-like system with $\Gamma \sim 1$, while case (a) corresponds to a crystallized Yukawa system with $\Gamma \simeq 10^4$. Experimental data are scattered within the area marked with (c) and in detail presented in the insert.

### 4.1.4 Conclusion

In this work, a first 3D analysis of a complex plasma in a dc discharge environment is presented. With striation free discharge conditions the particle cloud showed a liquidlike

structure with locally enhanced structural properties that indicate that the system was on its way to crystallization. Local order analysis was performed on the experimental data and compared with molecular dynamic simulation taking into account the experimental conditions. Simulation and experiment showed good agreement.

In order to better comprehend the possibilities of this kind of systems few more structures are presented in figures 4.3, 4.4 and 4.5 under different experimental conditions (pressure, power and particles densities). From the figures it is clearly visible that the macro structures like shells and layers strongly depend on the plasma conditions and particle density. Further studies should be directed to the detailed investigations of the dependence of macro structures on experimental conditions.

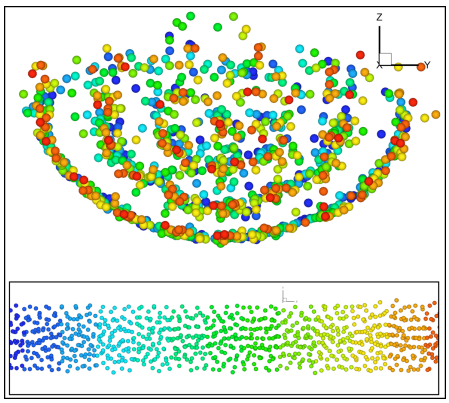


Figure 4.3: Experimentally recorded particle positions for 30 $Pa$ pressure and low power plasma. Shell-like structure is clearly visible.

The observed shell like structures could be of a special interest since is suggest that physical properties such as the shear viscosity might be anisotropic. Information about the structural arrangement of particles in this kind of confinement might help us understand similar generic properties of other cylindrical-shaped systems, particularly those on the nanometer scale e.g. nano-tubes.

A drawback of all these presented structures is the strong influence of gravity. Under the influence of their own weight the structures are strongly pushed into the sheath above the wall which influence the particle behavior. A complete understanding of the natural self-arrangement of particles under the present confinement can be realized only under microgravity conditions.

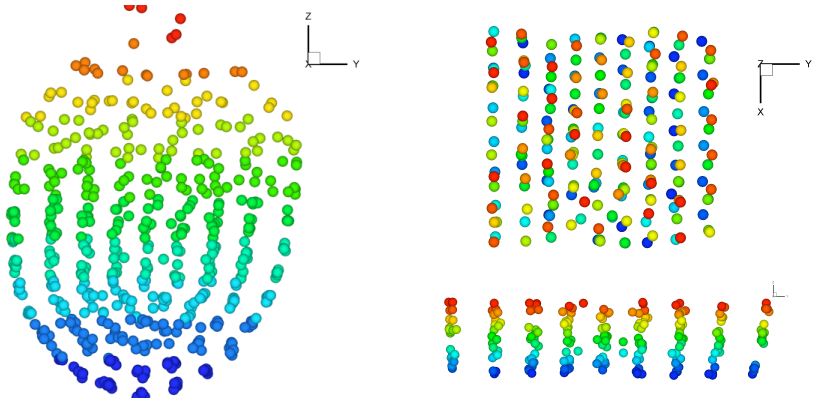

Figure 4.4: Example of other experimentally resolved particle positions (left). Top and side view of crossection of cloud approximately at the middle of its hight (right). Particles are clearly ordered in shells and have well defined order.

## 4.2 Convective Dust Clouds Driven by Thermal Creep in a Complex Plasma

### 4.2.1 Objectives

Convective motion of dust particles in complex plasmas is a phenomena that is often observed in very different experimental conditions. In this work a steady-state cloud of the microparticles levitating in the low-frequency glow discharge generated in vertically orientated "PK-4" laboratory setup were observed. A series of experiments dedicated to the study of the convective motion of dust particles in the presence of external controllable heating were performed.

There are many publications, both theoretical and experimental, in which the origin of vortex motion in complex plasmas has been investigated [89], [99], [129]. In particular, vortices in complex plasmas can be produced both in the ground-based experiments and under microgravity conditions, either in the dc and rf discharge plasmas. Many possible mechanisms can explain vortex motion in complex plasmas. This motion can be caused by the ion drag force [89], by nonpotential forces acting on the particles[130], by the convection of the background neutral gas [131], by an inhomogeneous electric field inside of striations [132] etc. This clearly indicates that the nature of such vortices, in spite of a quite similar appearance, might be different.

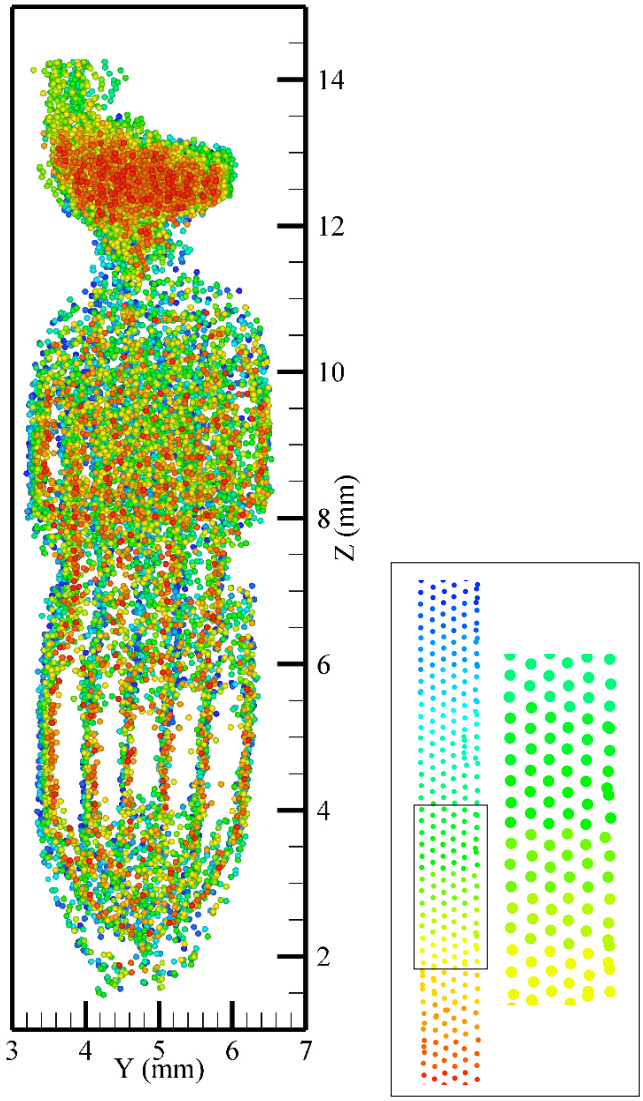


Figure 4.5: Particle structure at higher power and high pressure. The complexity of these structure is due to the presence of different types of particles in the plasma (left). One layer of particles at about 5 mm hight and magnification of one part of it (right). A clear hexagonal structural arrangement is obvious.

The main conclusion of the research presented here is that the particle motion is driven by the convective motion of the background neutral gas. The underlying mechanism of the convective gas motion is *thermal creep (slip)* induced by the temperature gradient along the tube walls.

The thermal creep flow, more then hundred years ago was predicted by maxwell and

discovered by Reynolds. Today, it is used in many industrial applications for chemical vapor deposition in the integrated circuit fabrication [133] and the crystal growth [134]. The influence of thermal creep on the particles in colloids, resulting in the formation of colloidal crystals was recently reported in [135]. Despite the importance of these applications, only a few experimental works dedicated to the thermal creep effect have been published [136], [137], [138]. The literature mostly consist of the reports of numerical simulations, see for example [139], [140], [141], [142].

### 4.2.2 Experiment

The experiments were conducted in a low frequency neon plasma produced in the vertically oriented "PK-4" laboratory setup. The polarity of the voltage between the electrodes was switched with a frequency of 1 kHz (duty cycle 50 %) so that the electric force along the tube axis, acting on the microparticles, effectively vanishes. Experiments were performed at constant pressures of 30, 50 and 100 Pa. The spherical melamine-formaldehyde particles of two different sizes (with the radius of 1.64 and 3.05 $\mu m$) were used.

The particles were levitated in the discharge above a metal wire that was put around the lower part of the tube. To produce heating a dc current was applied to the wire. We measured the temperature along the tube at different locations.

The results of measurements and the estimates showed that the maintained temperature gradient was not strong enough for thermophoretic levitation of the particles. However, the particles were confined and levitated in the area above the heating wire. Furthermore, the particles had a very well defined convective motion with the velocity directed upwards in the center of the tube and downwards close to the wall. The velocity of the particles and the shape of the particle cloud were depended on the pressure. Examples of the observed shapes of the particle cloud at different pressures are presented in figure 4.6. It's natural to assume, as it is discussed below, that the intense convective motion of the particles is induced by the gas motion triggered by the tube heating.

### 4.2.3 Results

The most important feature of the particle behavior is the fact that the particle cloud can levitate with the thermophoretic force not strong enough for full compensation of the gravitational force. This clearly implies that there is an additional force which serves

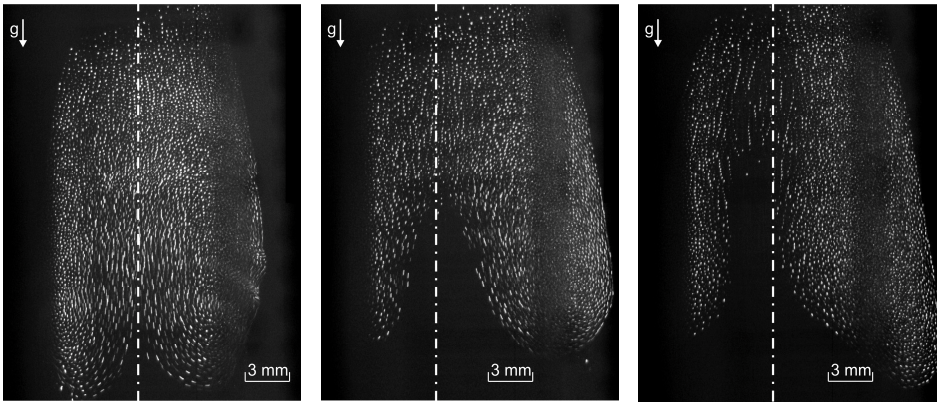


Figure 4.6: Dust clouds of $a = 1.64\mu m$ particles at pressures of 30, 50, and $100Pa$ (from left to right). The vertical dash-dotted lines indicate the position of the center of the tube. The field of view is 21 x 26 mm.

to compensate for gravity. This force acts on the particles and induces the convective motion. Plasma forces can not be responsible for this effect. Because of the fast polarity switching, neither the electric force nor the ion drag force could support the particles. The thermophoretic force, being potential, cannot cause convection because $\nabla \times F_{th} \equiv 0$. By these reasons, it was natural to assume that the intense convective motion of the particles is induced by the gas motion which is triggered by the local tube heating.

In order to verify this assumption a simple experiment was done. It was observed that the particles after switching off the discharge expand across the tube and keep rotating a few more cycles before eventually falling down. There is an additional radial electric force $F_r$ which confines the particles.

Under this conditions the particle dynamics is determined by the balance of forces:

$$m_p \ddot{\mathbf{r}} = \mathbf{F_{th}} + \mathbf{F_n} + \mathbf{F_r} + m_p \mathbf{g} \tag{4.2}$$

Since the thermophoretic force $F_{th}$, the particle positions and velocities are known, the only unknown remaining forces are neutral friction $\mathrm{F_n}$ and the radial electric force $\mathrm{F_r}$. We analyze first the data when plasma was off in the tube and hence no radial electric force ($F_r = 0$) acts on the particles. This allows us to get the velocity field of the conveying gas molecules which is not effected by the electric force.

With this information the radial electric force exerted by the plasma on the particles could be calculated for the area where the particle trajectories recorded with and without

plasma overlap as shown in figure 4.7.

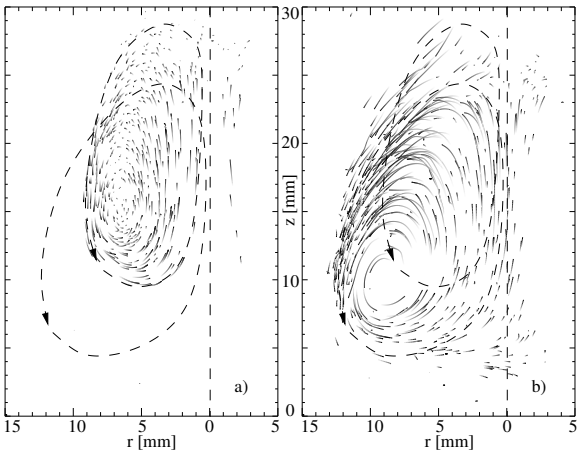


Figure 4.7: Convective dust clouds of $a = 3.05\mu m$ particles at a pressure of $50Pa$ for cases (a) "plasma on" and (b) "plasma off". The shape of the cloud and direction of the rotation in the "on" and "off" cases are indicated by the upper and lower loops, respectively, and their overlap shows the region used for the reconstruction of radial electric force (see Fig. 4.9). The vertical dashed lines show the center of the tube.

Figure 4.8 shows the velocity field of the gas convection as calculated for the case without plasma for 3.05 $\mu m$ size particles at 50 Pa. The gas flow has a rotational tendency where the particle velocity sets upwards in the centre of the tube and downwards close to the wall. The center of the particle cloud and the gas convection center are not in the same positions due to the relative velocity of the particles and the gas.

The radial electric force estimated by comparing particles trajectories in the "plasma on" and "plasma off" cases is presented in figure 4.9. The force tends to zero in the center of the tube and rapidly increases towards the tube walls.

The results obtained above clearly demonstrate the presence of gas convection. However, in the conditions of our experiments the estimated critical Rayleigh number for free convection is not high enough to produce this kind of gas flow. On the other hand, it is well known that if a non-uniformly heated body is inserted in a rarefied gas, the gas starts moving along the body in the direction of the temperature gradient [143], [144], [145]. This phenomenon is known as thermal gas creep (or thermal gas slip). It was predicted theoretically by Maxwell [146] and experimentally verified by Reynolds [147]. The velocity of the gas creep was estimated and it was shown that the convection velocity should decrease

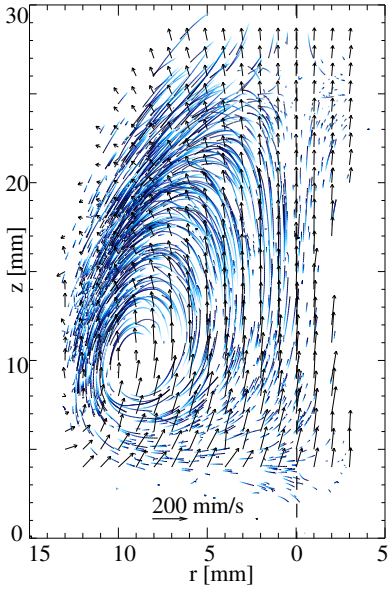


Figure 4.8: Averaged gas flow velocity field (vectors) superimposed with particles trajectories. The vertical dashed line indicates the center of the tube.

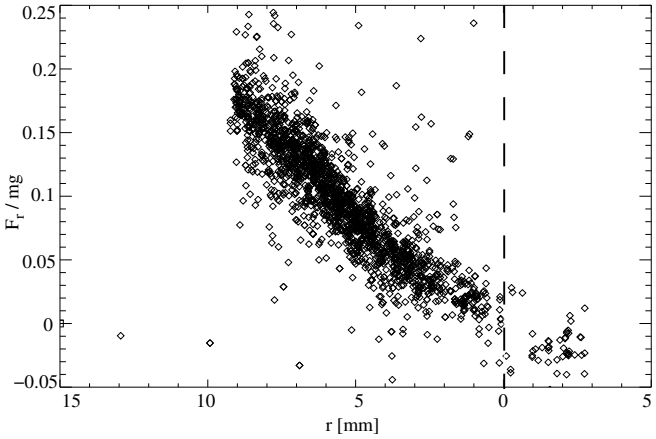


Figure 4.9: Reconstructed radial force for the overlapping region. The vertical dashed line indicates the center of the tube.

with the pressure as $\propto p^{-1}$ [97]. The free convection should increase with pressure [148].

A detailed analysis of the experiments at different pressures confirms the inverse pressure dependence of the convection velocity and clearly points to gas creep as the reason of convection.

### 4.2.4 Conclusion

To conclude, we observed steady-state particle clouds levitated in the vertical glass tube above the heated wire. The particles exhibited a global convective flow. We showed that the particle vortices were induced by convection of the neutral gas. The mechanism responsible for the gas convection was thermal creep along the inhomogeneously heated tube walls. The phenomenon of thermal creep, which commonly occurs in rarefied gases under the presence of thermal gradients, has never been taken into account in experiments with complex plasmas. We believe that this phenomenon should generally play a substantial role in the experiments, because

- the resulting convection can be triggered in the absence of gravity,
- it operates in the pressure range typical for complex plasmas, and
- it does not require substantial temperature gradients and hence might be triggered due to natural temperature inhomogeneities always present in experiments.

# 4.3 Spectroscopic Evaluation of the Effect of the Microparticles on a Radiofrequency Argon Plasma

## 4.3.1 Objectives

The objective of this work is to evaluate changes of number densities of metastable and resonant levels in an argon rf discharge induced by the presence of microparticles. For this purpose the spatial distribution of plasma emission spectra is observed in a pure plasma and in a plasma with particles. The measurements of the number density of the $1s$ states were based on a single mirror self-absorption method [149], [150]. In order to use this method in the presence of particles in the discharge a correction for the extinction of light on the microparticles is introduced.

## 4.3.2 Experimental method

Experiments are carried out in the "PK-3 Plus" laboratory setup at working pressures of 15, 30 and 60 Pa in argon buffer gas. The light from the discharge was collected by an optic fiber with a collimator attached to it. A mirror opposing the fiber was installed in such a way so that reflected light from the discharge could be used to probe the plasma. For each position in the discharge spectra with and without mirror were recorded. For the same plasma conditions measurements were done twice for each position for the microparticle free plasma and plasma with a large cloud of particles levitated in it.

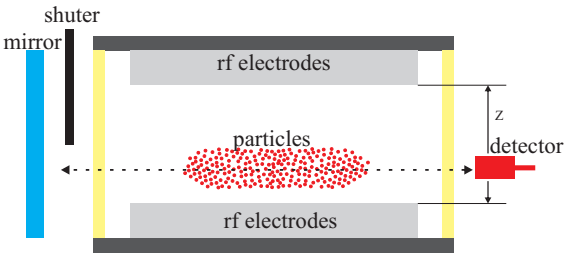


Figure 4.10: Sketch of the experimental setup for measuring the selfabsorption using single-mirror method.

The evaluation of the relative absorption was done by measuring a portion of the reflected light, transmitted through the plasma. In the microparticle-free plasma the only

mechanism contributing to the relative absorption is the absorption of the radiation by bottom levels of the respective transitions, i.e. self-absorption. In addition to that, in complex plasmas microparticles will also effectively contribute to the absorption due to extinction. Therefore, the absorption profile and optical thickness had to be rewritten as a sum of the plasma and microparticle components. Estimations, using the experimental data on the broadening of Ar lines, shows that collisional broadening is negligible and pure Doppler profile can be used [119]. Using the Doppler profile allows us to combine the relative absorption with the optical thickness of the plasma which is directly connected to the number density of the bottom state of the observed transition [151].

### 4.3.3 Results

To correctly determine the number density of the argon states in complex plasmas, the correction for the extinction of the light by the microparticles had to be taken into account. Due to the lack of data on the refractive index of melamine-formaldehyde in the observed spectral range it was impossible to make any estimations on light-particle interaction. For this reason we estimated this values experimentally using an argon lamp to evaluate the extinction on microparticles levitated in the *neon* buffer gas under the same plasma conditions and the same microparticle density. Neon plasma was used in order to avoid the absorption of source argon lines by the plasma therefore only extinction on particles can be measured. Typical values of the measured attenuation of argon lines by microparticles are presented in figure 4.11.

According to our results, for the number densities of the argon states to be determined in presence of a microparticle cloud, the attenuation $K_{ij}^{d}$ (Fig.4.11) must be taken into account. It was shown that neglecting this effect can lead up to 25 % overestimation of the number density of states.

Under the present conditions the discharge is strongly non-uniform and exhibits a classical $\alpha$-form of the rf discharge [152] with increased light intensity close to the powered electrodes and a darker area in the center presented in figure 4.3.3a. Due to the influence of gravity, the injected particles in the discharge concentrate themselves in the glow region above the bottom electrode figure 4.3.3c, which results in breaking the spatial symmetry of the light emission, figure 4.3.3b. A bright region above the bottom electrode significantly shifts into the central, relatively dark area of the discharge, while the upper half of the

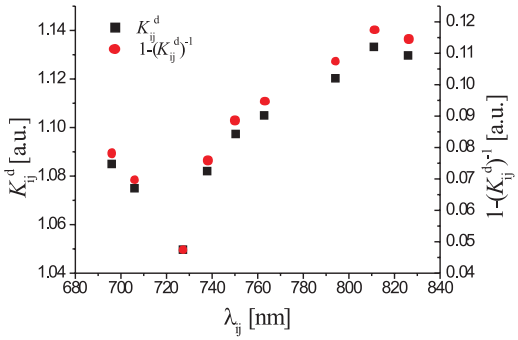


Figure 4.11: Measured spectral dependence of the attenuation $K_{ij}^{d}$ and relative absorbtion $1-\left(K_{ij}^{d}\right)^{-1}$ of the light by a cloud of 2.55 $\mu m$ diameter microparticles. In the spectral range of interest the relative absorbtion varies more than twice. The higest value of $K_{ij}^{d}$, obtained in our experiments, is $\approx$1.13

discharge remains almost undisturbed. Using the proposed method and correction due to the presence of microparticles in the discharge the observed changes in the light intensities were used for the evaluation of the number density of metastable and radiative states.

The axial distribution of the number density of states undergoes practically the same changes as the light distribution of the line intensities in the presence of microparticles. The strongest relative changes (twice or more with respect to microparticle-free plasma) are in the center of the discharge. This effect is much less pronounced at 15 Pa than at 30 and 60 Pa.

The observed effects of microparticles on the plasma can have different explanations. A non local increasing of the light emission and metastable densities were tried to be explained with the few mechanisms:

- Disturbance in the ionization balance due to the additional depletion of electrons on the particles surfaces.
- Secondary electron emission from ions and metastables interaction with particle surface.
- Sputtering of particles.

However, deeper insight into the role of each mechanism would require further experimental and theoretical investigations.

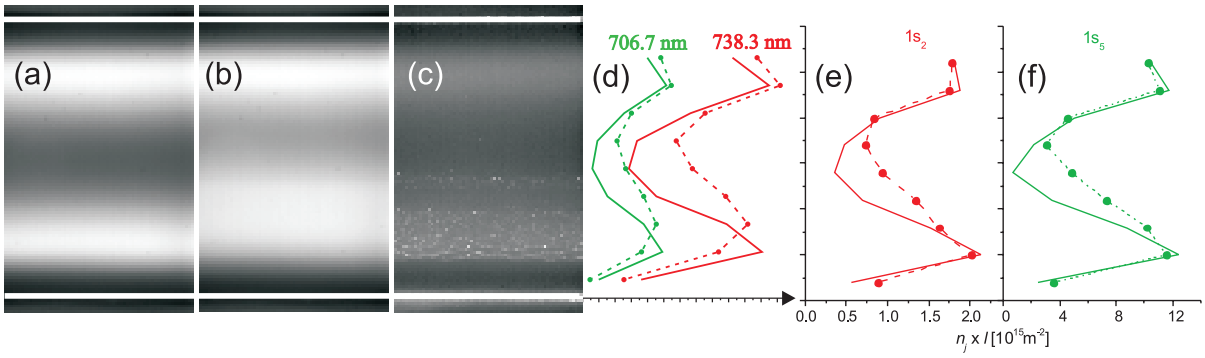


Figure 4.12: Influence of the presence of the microparticle cloud on the parallel-plate RF-discharge in argon at 30 Pa. (a) videoimage of a microparticle-free discharge; (b) videoimage of a discharge containing a microparticle cloud in the vicinity of the bottom electrode; (c) videoimage of a laser-illuminated microparticle cloud; (d) axial profiles of the intensities of argon spectral lines; (e) axial profile of the number density of metastable $1s_5$ state; (f) axial profile of the number density of radiative $1s_2$ state. In figures (d)-(f) solid line corresponds to the microparticle-free case and dashed line with circles corresponds to the case of a plasma, containing a microparticle cloud.

### 4.3.4 Conclusion

This work clearly demonstrated the influence of the microparticles presence in the plasma on the light emission and metastable density distribution. Under the considered experimental conditions its is clear that the cloud of microparticles, levitating in the plasma produces a significant non-local influence on the discharge. Presence of such a microparticle cloud leads to the enlargement of the bottom glow region, containing the microparticles. Measurements of the densities of $1s$ excited states of argon did not reveal significant changes in the amplitudes of their variation, whereas some local values increased twice and more in presence of microparticles. The underlying processes that cause these effects are not completely understood showing the importance of further investigations in this direction. In addition, it was shown that more attention should be focused on microparticle-light interaction in further spectroscopic observations of complex plasmas.

# 4.4 Determination of Electron Temperature in Low-pressure Plasmas by Means of Optical Emission Spectroscopy

## 4.4.1 Objectives

In this work a simple model for the electron temperature evaluation in a steady-state low-pressure plasma is proposed. Here we propose a method that allows to determine the parameters of the electron energy distribution function (EEDF) using the ratio of intensity of the same spectral line measured from two different but equal volumes in the plasma. The main objective of this work was to construct a model which takes into account the population from metastable levels leading to the increase of the contribution of low energy electrons in the processes of light emission.

## 4.4.2 Model

This model is based on the assumption of the Maxwellian electron energy distribution function and hence it is defined by one electron temperature. In the model we use the optical cross section [112], [113] for the ground and metastable states which include all possible cascade populations for the observed transitions.

If we observe a transition $\alpha$ from two different positions in plasma marked as 1 and 2, ratio of the light intensities can be expressed as

$$E_\alpha(T_{e,1}, T_{e,2}, \frac{n_{e,1}}{n_{e,2}}) = \frac{I_{\alpha,1}}{I_{\alpha,2}} \tag{4.3}$$

which is a function of the electron temperatures $T_{e,1}$, $T_{e,2}$ and the ratio of electron densities in these two positions $n_{e,1}/n_{e,2}$. The intensity is expressed by using optical cross sections described by equations (2.38) and (2.39) in chapter 2.5.1.

Now if we observe three transitions $\alpha$, $\beta$ and $\gamma$ then equation 4.3 can be constructed for all three of them. Using two transitions (e.g. $\alpha$ and $\beta$) a new quantity can be constructed which will cancel out the dependence on the electron densities:

$$F_{\alpha,\beta}(T_{e,1}, T_{e,2}) = \frac{E_\alpha}{E_\beta} = \frac{I_{\alpha,1}/I_{\alpha,2}}{I_{\beta,1}/I_{\beta,2}} \tag{4.4}$$

The same equation can be constructed for different combination of lines e.g. $\beta$, $\gamma$. In this way two equations can be constructed which will at the end depend only on electron temperatures in the observed points. Finally, a system of equations can be constructed in the following form:

$$F_{\alpha,\beta}(T_{e,1}, T_{e,2}) - \frac{I_{\alpha,1}/I_{\alpha,2}}{I_{\beta,1}/I_{\beta,2}} = 0 \tag{4.5}$$

$$F_{\beta,\gamma}(T_{e,1}, T_{e,2}) - \frac{I_{\beta,1}/I_{\beta,2}}{I_{\gamma,1}/I_{\gamma,2}} = 0 \tag{4.6}$$

Here we concentrate on a Maxwellian EEDF for simplicity. The model can be easily extended for the case of more complicated EEDF. This will require to expand the model with additional spectral lines in order to build the system of equations for more then two unknowns.

Shortly, two types of measurements were done, one in a pure plasma and another one with a cloud of melamine-formaldefyde monodisperse particles of 2.55 $\mu m$ diameter, levitated in it. Typical density of microparticles was always of the order of $10^{11}$ $m^{-3}$. The method was demonstrated on the results presented in previous section (for details see [119]).

The input parameters of the method are the density of the long-living argon states, ground and two metastable states, $n_g$, $n_{1s5}$ and $n_{1s3}$, respectively and the intensity of the spectral lines. The metastable densities are measured by the single-mirror method, described in previous chapter. Due to the relatively large self-absorption the measured intensity of spectral lines had to be corrected for the values estimated in [119]. The results presented below are just to demonstrate the performance of the method and to give ideas of how the method can be applied to the experimental data (from previous section).

### 4.4.3 Results

The method was applied for two different experimental conditions. First, the electron temperatures in two different points in the plasma were evaluated for pure plasma, and then this method was used for the evaluation of changes of the electron temperature in the same point in the plasma due to the presence of particles.

The results are presented in $(T_1, T_2)$ plane, i.e. for two different positions in the pure plasma or same position for cases with and without particles in the plasma. In ideal case the solution can be represented as the intersection of two curves corresponding to equations

4.5 and 4.6 in $(T_1, T_2)$ plane. Due to the uncertainty of the measurements the results of the model are presented as intersections of finite areas which are determined by the uncertainty of the function F defined by the value $\delta F$.

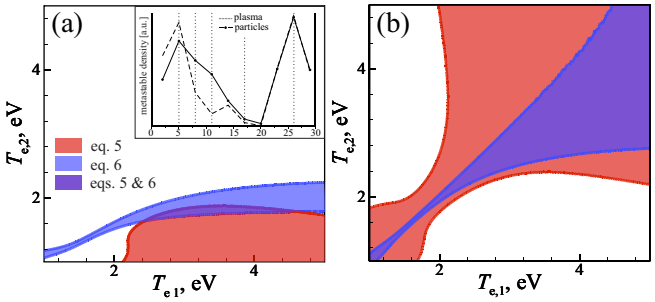


Figure 4.13: Solution of eqs. 4.5 and 4.6 for the points in microparticle-free plasma at an argon pressure of 60 Pa and RF power of 0.2 W with $\delta F = \pm 0.05$: (a) index 1 corresponds to the vertical position $z = 5$ mm (peak of emission), index 2 - to $z = 11$ mm (minimum of the emission); (b) index 1 - $z = 5$ mm (peak of emission), index 2 - $z = 26$ mm (symmetric peak of emission). Evidently, the temperatures are much better determined if the two points with significantly different parameters are considered. The metastable density profile and the positions used for the evaluation are presented in the inset.

In figure 4.13 an example of the solution of the system for two characteristic points in the microparticle-free plasma are presented. Fig 4.13(a) represent the solution of the system for positions in the plasma which are quite different in all input parameters which lead to the difference in the electron temperatures in these two positions, presented as purple crossection. On the other hand, fig 4.13(b) is the case for two points in the discharge with almost the same parameters (metastable density and light intensity) and the solution of the system indicate the equality of electron temperatures, $T_{e,1} = T_{e,2}$ line lying inside the intersection.

The analysis for the case of the presence of microparticles in the plasma is presented in figure 4.14. The estimated electron temperatures were done for the same position in plasma with and without particles. For the following consideration we define the electron temperature in a microparticle-free plasma $T_p \equiv T_{e,1}$ and electron temperature in a dusty plasma, $T_d \equiv T_{e,2}$. Figure 4.14a for $z = 5$ mm (for positions reference see inset in figure 4.13a) the upper limit of $T_e$ is 4.4 eV significantly larger then that of $T_d$ (2.8 eV). Situation is opposite at $z = 8$ mm (4.13b) where the upper limit of $T_d$ is higher and the density of

the $1_s$ state increase in the presence of microparticles. At $z = 17$ and $z = 26$ mm (4.13c,d respectively) influence of microparticles is small and $T_e$ and $T_d$ can hardly be determined.

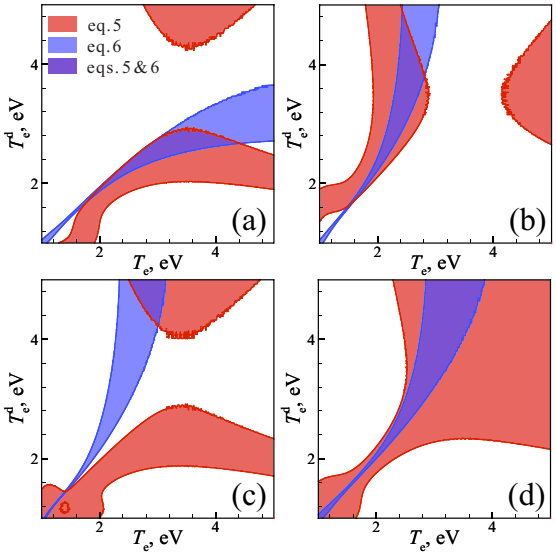


Figure 4.14: Solution of eqs. 4.5 and 4.6 for the points in the plasma at the argon pressure of 60 Pa and RF power of 0.2 W with $\delta F = \pm 0.02$. (a) $z = 5$ mm, presence of microparticles decreases the densities of $1s$ states; (b) $z = 8$ mm, presence of microparticles increases the densities of $1s$ states; (c) $z = 17$ mm and (d) $z = 26$, presence of microparticles practically does not affect the densities of $1s$ states; Vertical positions for (a) and (b) are inside the microparticle cloud, whereas for (c) and (d) outside. For (d) the density of $1s$ states is significantly higher, than that for (c). $T_\mathrm{e}$ exhibits much larger upper limit than $T_\mathrm{e}^\mathrm{d}$ in (a) and vice versa in (b), which is in accord with the previously observed effect of microparticles on the densities of $1s$ states of argon. For (c) and (d) effect of microparticles is negligibly small and therefore, determination of the temperatures is not possible.

### 4.4.4 Conclusion

In conclusion, we presented a spectroscopic method, allowing to evaluate (in the assumption of a Maxwellian EEDF) the electron temperature in a low-pressure plasma. The method is based on the experimentally measured density of metastable states and intensity of spectral lines. Spectroscopic data from [119] was used as an example for the temperature evaluation. Construction of the model cancels the influence of the relative calibration of spectral lines

e.g. sensitivity of the measurement devices on different wavelengths. Construction of the system with more spectral lines would allow to use more complicated EEDF's as well as estimation of electron densities changes.

# Chapter 5

# Outlook and future work

The first paper enclosed in this thesis deals with the structural properties of complex plasmas. Only a limited number of publications of a three dimensional analysis of complex plasma structures was the main argument for conducting this work. The presented structures represent the first observation of an ordered complex plasma in a dc-like discharge and a tube-like geometry. It was shown that the ordering of the microparticles is strongly influenced by the confinement (dependent on both, geometry of the tube and plasma properties) and gravity resulting in the appearance of macro structures like shells and layers. The main drawback in this work is the strong compression due to the gravity.

- *Future work should be oriented on observation of these structures under microgravity conditions. Without gravitational perturbation microparticles should arrange in a more ideal way consisting of only cylindrically symmetric shell structures. This kind of environment would be perfect for parametric studies of the structural arrangement and could reveal its full nature. A complex dc discharge experiment (PK-4) under microgravity on board of ISS is planned for 2012.*

The second paper address fundamental thermodynamic properties of gases. The thermal induced gas creep is a phenomena predicted by Maxwell more than 150 years ago. Since then there are not many publications devoted to experimental verifications of this effect. Today, thermal creep is used in industry for chemical vapor deposition in integrated circuit fabrication and crystal growth. The literature for thermal induced gas creep mostly consists of reports of numerical simulations. In complex plasma, as it was shown, this effect can be responsible for a strong convective motion of the particles. Convective motions

of microparticles are present in many experiments but its nature was usually assigned to termophoretic forces or gradients in the electric field. The presented results may serve the fluid mechanic community as an experimental verification of the existence of thermal creep and the dusty plasma community as a demonstration of the significance of this effect on dusty plasmas. Recent experimental work [138] confirms the results presented here. The importance of a thermally induced gas creep in colloidal science was recently reported in [135] where it was found to be responsible for forming colloidal crystals.

The last two papers presented in this thesis are dedicated to plasma spectroscopy. In the first work, the effect of the presence of microparticles in the plasma is evaluated by a measurement of the metastable density. For this purpose the selfabsorption method for the evaluation of the metastable density is used for a pure plasma, while for a plasma with microparticles a correction factor had to be included taking into account the extinction of light on microparticles. Beside the main results of the metastable density evaluation this work is important for the measurement of light extinction on the microparticle surface. The proposed correction should be taken into account for any spectroscopic evaluation of complex plasmas, according to the microparticle density and size. The discussion of possible reasons for metastable density changes due to the presence of microparticles in the plasma is focused on the disturbance of the ionization balance and plasma particle interaction in form of secondary electron emission.

- *Future work should be devoted to more precise measurement of light extinction by microparticles in complex plasmas. Measurements should be done for further particle sizes and materials.*

- *Based on the results presented here, a new experiment is already designed for MIE scattering measurements which should result in the evaluation of refractive index of the observed particles.*

- *The method for the extinction measurement used in presented work can be used for the evaluation of the size distribution of the particles in complex plasmas. The minimum of the extinction depends on the particle size, while the intensity of the extinction on the particle density. More attention should be directed on this method because of its simplicity and since it is an in-situ measurement. The setup allowing detailed, systematic measurements is already in the construction stage.*

The last paper presented within this thesis focuses on a simple evaluation of electron temperature changes based on the results of the previous paper. A simple model is proposed, based on measurements of the light intensity, the metastable density, and a basic assumptions about the shape of EEDF. The biggest advantage of this model is the fact that it can be extended to more lines and more complicated EEDFs.

- *Future work should be directed to the more precise evaluation of the proposed model with the parallel comparisons with the experimental and numerical works.*
- *With more precise measurements of the plasma emission spectra model should be tried for more complicated EEDFs taking into account more spectral lines.*

# Bibliography


[1] I. Langmuir, C. G. Found, and A. F. Dittmer, Science **LX**, 392 (1924).

[2] O. Havnes, Adv. Space Res. **4**, 75 (1984).

[3] O. Havnes, T. K. Aanesen, and F. Melandsø, J. Geophys. Res. **95**, 6581 (1990).

[4] H. Thomas et al., Phys. Rev. Lett. **73**, 652 (1994).

[5] J. H. Chu and L. I, Phys. Rev. Lett. **72**, 4009 (1994).

[6] Y. Hayashi and K. Tachibana, Jpn. J. Appl. Phys. **33**, L804 (1994).

[7] A. Melzer, T. Trottenberg, and A. Piel, Physics Letters A **191**, 301 (1994).

[8] O. Havnes et al., J. Geophys. Res. **101**, 10839 (1996).

[9] R. Greenberg, A. Brahic, and eds., *Planetary Rings*, The University of Arizona Press, Arizona, 1984.

[10] B. A. Smith et al., Science **212**, 163 (1981).

[11] B. A. Smith et al., Science **215**, 504 (1982).

[12] C. K. Goertz and G. E. Morfill, Icarus **53**, 219 (1983).

[13] E. Grün, G. E. Morfill, R. J. Terrile, T. V. Johnson, and G. Schwehm, Icarus **54**, 227 (1983).

[14] G. E. Morfill and H. M. Thomas, Icarus **179**, 539 (2005).

[15] G. S. Selwyn, J. Singh, and R. S. Bennett, J. Vac. Sci. Technol. A **7**, 2758 (1989).

[16] K. G. Spears, T. J. Robinson, and R. M. Roth, Plasma Science, IEEE Transactions on **14**, 179 (April 1986).

[17] H. Kersten et al., Contrib. Plasma Phys. **41**, 598 (2001).

[18] A. Bouchoule, *Technological impacts of dusty plasmas, in: A. Bouchoule (Ed.), Dusty Plasmas: Physics, Chemistry and Technological Impacts in Plasma Processing*, Wiley, Chichester, 1999.

[19] S. V. Vladimirov, K. Ostrikov, and A. A. Samarian, *Physics and applications of Complex Plasmas*, Imperial College, Lonon, 2005.

[20] A. Bouchoule and L. Boufendi, Plasma Sources Sci. Technol. **3**, 292 (1994).

[21] A. Bouchoule and L. Boufendi, Plasma Sources Sci. Technol. **2**, 204 (1993).

[22] A. Bouchoule, A. Plain, L. Boufendi, J. P. Blondeau, and C. Laure, J. Appl. Phys. **70**, 1991 (1991).

[23] L. Boufendi and A. Bouchoule, Plasma Sources Sci. Technol. **3**, 262 (1994).

[24] L. Boufendi et al., J. Appl. Phys. **73**, 2160 (1993).

[25] L. Boufendi et al., J. Appl. Phys. **76**, 148 (1994).

[26] L. Boufendi et al., Appl. Phys. Lett **60**, 169 (1992).

[27] E. Stoffels, W. W. Stoffels, G. M. W. Kroesen, and F. J. de Hoog, J. Vac. Sci. Technol. **14**, 556 (1996).

[28] A. Pigarov et al., Journal of Nuclear Materials **363-365**, 216 (2007).

[29] M. S. Barnes, J. H. Keller, J. C. Forster, J. A. O'Neill, and D. K. Coultas, Phys. Rev. Lett. **68**, 313 (1992).

[30] A. Bouchoule, *Dusty Plasmas: Physics, Chemistry and Technological impacts in Plasma Processing*, Wiley, New York, 1999.

[31] P. R. i Cabarrocas, P. Gay, and A. Hadjadj, J. Vac. Sci. Technol. **A 14**, 655 (1996).

[32] P. R. i Cabarrocas, N. Layadi, M. Kunst, C. Clerc, and H. Bernas, J. Vac. Sci. Technol. **A 16**, 436 (1998).

[33] W. Stoffels and E. Stoffels, Trends in Vacuum Science and Technology **4**, 1 (2001).

[34] R. J. Buss and S. V. Babu, J. Vac. Sci. Technol. **A 14**, 577 (1996).

[35] F. Vivet, A. Bouchoule, and L. Boufendi, J. Appl. Phys. **83**, 7474 (1998).

[36] A. V. Ivlev et al., To be published .

[37] H. Thomas et al., Phys. Rev. Lett. **73**, 652 (1994).

[38] J. Chu and L. I, Phys. Rev. Lett. **72**, 4009 (1994).

[39] Y. Hayashi and S. Tachibana, Jpn. J. Appl. Phys. **33**, L804 (1994).

[40] A. Melzer, T. Trottenberg, and A. Piel, Phys. Lett. A **191**, 301 (1994).

[41] V. E. Fortov et al., JETP Lett. **64**, 92 (1996).

[42] V. E. Fortov et al., JETP Lett. **63**, 187 (1996).

[43] V. E. Fortov et al., Dokl. Phys. **44**, 279 (1999).

[44] V. I. Vladimirov et al., Plasma Physics Reports **27**, 36 (2001).

[45] H. M. Thomas and G. E. Morfill, Nature **379**, 806 (1996).

[46] R. D. Smirnov, A. Y. Pigarov, M. Rosenberg, S. I. Krasheninnikov, and D. A. Mendis, Plasma Physics and Controlled Fusion **49**, 347 (2007).

[47] P. R. i Cabarrocas, A. F. i Morral, S. Lebib, and Y. Poissant, Pure Appl. Chem. **74**, 359 (2002).

[48] P. R. i Cabarrocas et al., Journal of Physics D: Applied Physics **40**, 2258 (2007).

[49] M. Rubin-Zuzic et al., Nature Physics **2**, 181 (2006).

[50] C. A. Knapek, A. V. Ivlev, B. A. Klumov, G. E. Morll, and D. Samsonov, Phys. Rev. Lett. **98**, 015001 (2007).

[51] C. A. Knapek, D. Samsonov, S. Zhdanov, U. Konopka, and G. E. Morll, Phys. Rev. Lett. **98**, 015004 (2007).

[52] V. Nosenko, S. K. Zhdanov, A. V. Ivlev, C. A. Knapek, and G. E. Morfill, Phys. Rev. Lett. **103**, 015001 (2009).

[53] R. Heidemann, S. Zhdanov, R. Sütterlin, H. M. Thomas, and G. E. Morll, Phys. Rev. Lett. **102**, 135002 (2009).

[54] R. L. Merlino, A. Barkan, C. Thompson, and N. D'Angelo, Phys. Plasmas **5**, 1607 (1998).

[55] S. Nunomura, S. Zhdanov, D. Samsonov, and G. Morfill, Phys. Rev. Lett. **94**, 045001 (2005).

[56] V. Nosenko, S. Zhdanov, and G. Morll, Phys Rev Lett **99**, 025002 (2007).

[57] V. Nosenko and S. K. Zhdanov, Contrib. Plasma Phys. **49**, 191 (2009).

[58] S. Mitic, B. A. Klumov, U. Konopka, M. H. Thoma, and G. E. Morll, Phys. Rev. Lett. **101**, 125002 (2008).

[59] G. E. Morfill and A. V. Ivlev, Review of Modern Physics **81**, 1353 (2009).

[60] P. K. Shukla and A. A. Mamun, *Introduction to dusty plasma*, IOP Publishing, 2002.

[61] J. E. Allen, B. M. Annaratone, and U. de Angelis, Journal of Plasma Physics **63**, 299 (2000).

[62] R. V. Kennedy and J. E. Allen, Journal of Plasma Physics **69**, 485 (2003).

[63] S. Vladimirov, K. Ostrikov, and A. Samarian, *Physics and Applications of Complex Plasmas*, Imperial Press, London, 2005.

[64] T. Matsoukas and M. Russell, J. Appl. Phys. **77**, 4285 (1995).

[65] B. Rovagnati, M. Davoudabadi, G. Lapenta, and F. Mashayek, J. Appl. Phys. **102**, 073302 (2007).

[66] A. V. Zobnin, A. P. Nefedov, V. A. Sinel'Shchikov, and V. E. Fortov, Soviet Journal of Experimental and Theoretical Physics **91**, 483 (2000).

[67] S. A. Khrapak et al., Phys. Rev. E **72**, 016406 (2005).

[68] S. A. Khrapak and G. E. Morll, Phys. Plasmas **15**, 114503 (2008).

[69] S. Khrapak and G. Morll, Contrib. Plasma Phys. **49**, 148 (2009).

[70] V. E. Fortov, A. G. Khrapak, S. A. Khrapak, V. I. Molotkov, and O. F. Petrov, Phys. Usp. **47**, 447 (2004).

[71] S. Khrapak, S. Zhdanov, A. Ivlev, and G. Morfill, J. Appl. Phys. **101**, 033307 (2007).

[72] S. Khrapak, G. Morfill, A. G. Khrapak, and L. G. D'yachkov, Phys. Plasmas **13**, 052114 (2006).

[73] U. Konopka, G. E. Morfill, and L. Ratke, Phys. Rev. Lett. **84**, 891 (2000).

[74] A. M. Ignatov, Plasma Phys. Rep. **22**, 585 (1996).

[75] V. N. Tsytovich, Y. K. Khodataev, G. E. Morll, R. Bingham, and D. J. Winter, Comments Plasma Phys. Control. Fusion **17**, 249 (1996).

[76] M. Lampe, G. Joyce, G. Ganguli, and V. Gavrishchaka, Phys. Plasmas **7**, 3851 (2000).

[77] V. N. Tsytovich, Y. K. Khodataev, G. E. Morll, R. Bingham, and D. J. Winter, Comments Plasma Phys. Control. Fusion **18**, 281 (1998).

[78] A. Melzer, V. A. Schweigert, and A. Piel, Physical Review Letters **83**, 16 (1999).

[79] S. Vladimirov and K. Ostrikov, Phys. Rep. **393**, 175 (2004).

[80] P. S. Epstein, Phys. Rev. **23**, 710 (1923).

[81] M. Mikikian, L. Boufendi, and A. Bouchoule, Spectroscopic analysis and instabilities observation during dust particle growth, in *30$^{th}$ EPS Conf. on Contr. Fusion and Plasma Phys.*, edited by R. Koch and S. Lebedev, volume 27A, pages 0–3.1B, 2003.

[82] D. Samsonov and J. Goree, Phys. Rev. E **59**, 1047 (1999).

[83] S. Khrapak, A. V. Ivlev, G. E. Morfill, and H. M. Thomas, Phys. Rev. E **66**, 046414 (2002).

[84] V. Yaroshenko et al., Phys. Plasmas **12**, 093503 (2005).

[85] A. Ivlev, S. Zhdanov, S. Khrapak, and G. Morfill, Plasma Phys. Control. Fusion **46**, B267 (2004).

[86] I. H. Hutchinson, Plasma Phys. Controlled Fusion **48**, 185 (2006).

[87] A. Ivlev, D. Samsonov, J. Goree, G. Morfill, and V. Fortov, Phys. Plasmas **6**, 741 (1999).

[88] S. A. Khrapak and V. V. Yaroshenko, Phys. Plasmas **10**, 4616 (2003).

[89] G. E. Morfill et al., Phys. Rev. Lett. **83**, 1598 (1999).

[90] V. E. Fortov, A. V. Ivlev, S. A. Khrapak, A. G. Khrapak, and G. E. Morfill, Phys. Reports **421**, 1 (2005).

[91] S. Khrapak, A. Ivlev, G. Morfill, and H. Thomas, Phys. Rev. E **66**, 046414 (2002).

[92] S. Khrapak, A. Ivlev, G. Morfill, and S. Zhdanov, Phys. Rev. Lett. **90**, 225002 (2003).

[93] H. Rothermel, T. Hagl, G. E. Morfill, M. H. Thoma, and H. Thomas, Phys. Rev. Lett. **89**, 175001 (2002).

[94] C. Gerthsen, Springer, Berlin (1958).

[95] F. Reif, McGraw-Hill, New York (1965).

[96] R. N. Varney, Phys. Rev. **88**, 362 (1952).

[97] S. Mitic et al., Phys. Rev. Lett. **101**, 235001 (2008).

[98] M. Schwabe et al., Phys. Rev. Lett. **102**, 255005 (2009).

[99] M. Rubin-Zuzic, H. M. Thomas, S. K. Zhdanov, and G. E. Morll, New J. Phys. **9**, 39 (2007).

[100] L. M. Vasilyak, S. P. Vetchinin, D. N. Polyakov, and V. E. Fortov, JETP **100**, 1166 (2005).

[101] V. Fortov, A. Ivlev, S. Khrapak, A. Khrapak, and G. Morll, Physics Reports **421**, 30 (2005).

[102] B. A. Klumov and G. E. Morfill, JETP Lett. **85**, 498 (2007).

[103] B. Smith et al., Advances in Space Research **34**, 2379 (2004).

[104] T. E. Sheridan, Physic of Plasmas **15**, 103702 (2008).

[105] O. S. Vaulina, S. V. Vladimirov, O. F. Petrov, and V. E. Fortov, Physics of Plasma **11**, 3234 (2004).

[106] P. J. Steinhardt, D. R. Nelson, and M. Ronchetti, Phys. Rev. B **28**, 784 (1983).

[107] B. A. Klumov and G. E. Morfill, JETP Lett. **90**, 444 (2009).

[108] Y.-M. Ling, J. Phys. D: Appl. Phys. **39**, 3305 (2006).

[109] N. Kang, S. ghee Ohand, and A. Ricard, J. Phys. D: Appl. Phys. **41**, 155203 (2008).

[110] T. M. Desai et al., Vacuum **46**, 223 (1994).

[111] X.-M. Zhu, W.-C. Chen, J. Li, and Y.-K. Pu, J. Phys. D: Appl. Phys. **42**, 025203 (2009).

[112] B. Moiseevitch and S. Smith, Rev. Mod. Phys. **40**, 238 (1968).

[113] D. Heddle and J. Gallagher, Rev. Mod. Phys. **61**, 221 (1989).

[114] J. B. Boffard1, C. C. Lin, and C. A. D. Jr, J. Phys. D: Appl. Phys. **37**, R143 (2004).

[115] D. Samsonov and J. Goree, IEEE Trans. Plasma Sci. **27**, 76 (1996).

[116] S. Hübner and A. Melzer, Phys. Rev. Lett. **102**, 215001 (2009).

[117] H. T. Do, H. Kersten, and R. Hippler, New J. Phys. **10**, 053010 (2008).

[118] H. T. Do, V. Sushkov, and R. Hippler, New J. Phys. **11**, 033020 (2009).

[119] S. Mitic, M. Y. Pustylnik, and G. E. Morfill, New J. Phys. **11**, 083020 (2009).

[120] G. H. P. M. Swinkels, PhD Thesis (1999).

[121] V. Fortov et al., Journal of Experimental and Theoretical Physics **87**, 1087 (1998).

[122] M. Horanyi, B. Walch, and S. Robertson, Geophys. Res. Lett. **22**, 2079 (1995).

[123] M. Horanyi, B. Walch, S. Robertson, and D. Alexander, J Geophys. Res. **193**, 8575 (1998).

[124] D. A. MacLennan, Physical Review **148**, 218 (1966).

[125] H. Ishii, S. Masuda, and Y. Harada, Surface Science **239**, 222 (1990).

[126] W. Butler, D. Oro, F. Dunning, and G. Walters, Surface Science **261**, 382 (1991).

[127] W. Sesselmann et al., Phys Rev Lett **50**, 446 (1982).

[128] A. P. Nefedov et al., New J. Phys. **5**, 33.1 (2003).

[129] O. S. Vaulina, A. P. Nefedov, O. F. Petrov, and V. E. Fortov, JETP **91**, 1147 (2000).

[130] V. E. Fortov et al., JETP **96**, 704 (2003).

[131] A. V. Ivlev, S. K. Zhdanov, and G. E. Morll, Phys. Rev. Lett. **99**, 135004 (2007).

[132] M. M. Vasiliev, S. N. Antipov, and O. F. Petrov, J. Phys. A: Math. Gen. **39**, 4539 (2006).

[133] D. W. Hess and K. F. Jensen, American Chemical Society, Washington, D.C. , 203 (1989).

[134] S. Mussoa, S. Porroa, M. Rovereb, M. Giorcellia, and A. Tagliaferro, J. Cryst. Growth **310**, 477 (2008).

[135] F. M. Weinert and D. Braun, Phys Rev Lett **101**, 168301 (2008).

[136] Y. Sone, Phys. Fluids A **3**, 997 (1991).

[137] Y. Sone, K. Sawada, and H. Hirano, Eur. J. Mech. B/Fluids **13**, 299 (1994).

[138] T. M. Flanagan and J. Goree, Phys. Rev. E **80**, 046402 (2009).

[139] T. Ohwada, Y. Sone, and K. Aoki, Phys. Fluids A **1**, 1588 (1989).

[140] T. Ohwada, Y. Sone, and K. Aoki, Phys. Fluids A **1**, 2042 (1989).

[141] V. Y. Aleksandrov, Fluid Dynamics **36**, 658 (2001).

[142] H. C. Weng and C.-K. Chen, J. Phys. D: Appl. Phys. **2008**, 115501.

[143] E. M. Lifshitz and L. P. Pitaevskii, Pergsmon, Oxford (1981).

[144] M. N. Kogan, Plenum, New York (1969).

[145] S. P. Bakanov, Usp. Fiz. Nauk **162**, 133 (1992).

[146] J. C. Maxwell, Philos. Trans. R. Soc. London **170**, 231 (1879).

[147] O. Reynolds, Philos. Trans. R. Soc. London 170 **170**, 727 (1879).

[148] S. Chandrasekhar, Oxford University, Oxford (1961).

[149] V. N. Ochkin, Berlin:Wiley (2009).

[150] Z. Gavare, D. Gött, A. V. Pipa, J. Röpcke, and A. Skudra1, Plasma Sources Sci. Technol. **15**, 391 (2006).

[151] M. Schulze, A. Yanguas-Gil, A. von Keudell, and P. Awakowicz, J. Phys. D: Appl. Phys. **41**, 065206 (2007).

[152] Y. P. Raizer, M. N. Shneider, and N. A. Yatsenko, *Radio-Frequency Capacitive discharges*, CRC Press LLC, Florida, 1995.

# Acknowledgements

The work presented in this thesis would not have been possible without the support and understanding of many people mixed with coincidence and little bit of luck to which i am very thankful.

At first I would like to thank Prof. Dr Gregor Morfill, my supervisor and group leader, for giving me unique opportunity to join his remarkable Complex Plasma group at the Max-Planck-Insitut für extraterrestrische Phisik and his support and encouragement during this work.

Special thanks to Prof. Dr. Markus Thomas for his guidance and help, specially in the beginning of my work at the institute, when the help was most needed and also for his patience for endless reading and corrections of this manuscript and many helpful suggestions.

I would like to express my deepest gratitude to people from PK-4 teem with whom I was closely collaborated during this time. Thanks to Herrn Herwig Höfner for his time and understanding regarding the continuous questions about all the technical details of the experimental setup. Thanks to outstanding engineers Christian Rau and Sebastian Albrecht for shown patience and understanding for all the technical challenges that I've presented them. It's the teem that every experimentalist can wish for! Their unique "finger-cross" system is responsible for many new scientific discoveries. I am very thankful for the shown trust and given freedom to work freely in the PK-4 setup with such great scientific and technical support.

Here I would like to thank the coauthors of publications that are bases of this thesis. Many thanks to Dr. Sergey Zhdanov, Dr. Boris Klumov, Dr. Uve Konopka, Robert Sütterlin, Dr. Alexey Ivlev, Dr. Markus Thomas, Herwig Höfner, Dr. Mikhail Pustylnik for their significant contributions and ideas. I am looking forward working with you on new problems.

Special gratitude goes to Mikhail and Boris for their never ending creative ideas which kept me busy and excited for last years.

I would like to thank the people specially responsible for non-scientific part of my life in Germany, Robert for all the social (specially night-life) activities, Ralf for all the sports we did, Manish for Indian dinners and specially my officemate Christina for all the fun in the office and coffee breaks from nerve breaking physics problems.

I would like to thank the rest of complex plasma group for great atmosphere and unselfish help: Dr. Tetyana Antonova, Dr. Pintu Bandyopadhyay, Philip Brandt, Dr. Lénaïc Couëdel, Chengran Du, Martin Fink, Florian Huber, Peter Huber, Dr. Lujing Hou, Ke Jiang, Dr. Michael Kretschmer, Dr. Roman Kompaneets, Dr. Sergey Khrapak, Dr. Yang- fang Li, Dr. Vladimir Nosenko, Dr. Mierk Schwabe, Dr. Satoshi Shimizu, Dr. Tetsuji Shimizu, Günter Stadler, Bernd Steffes, Dr. Hubertus Thomas, Karl

Tarantik, Prof. Dr. Vadim Tsytovich, Günter Wildgruber, Lisa Woerner, Valeriy Yaroshenko, Dr. Victoria Yarushenko, and Dr. Julia Zimmermann. Special thanks go to our secretaries, Elsbeth Collmar and Angelika Langer, for their support whenever needed.

Special thanks goes to Dr. Milenko Rubin-Zuzic who I consider personally responsible for me being here. All of this would be impossible that we didn't meat long ago on the conference when his talk about the institute strongly attracted me and make me wish to join such a prestige scientific group.

Also, I am very grateful to Prof. Dr. Miodrag Radović and Dr. Čedomir Maluckov who are responsible for my first contact with the experiments and research work in my earliest phase of education.

My deepest gratitude goes to my parents Ljubinka and Dragoslav and my brother Bojan for their love and support throughout my life. Without your understanding and blessing I couldn't make it.

I am thankful for the people that are around me all the time, specially for friends Mima and Kole which were great support.

At the end, I would like to thank my wife Tanja for her strength and energy she have invested in our relationship to make it work so god. Without you next to me, all the time, it would be so much harder for me to finish this great chapter of my life. Thank you for all the listening, support and all the peacefulness that your presence brings me.

# Curriculum Vitae

**Slobodan Mitić**

| | |
|---|---|
| Date of birth | January 14, 1979 |
| Place of birth | Niš, Serbia |
| Nationality | Serbian |
| E-mail | mitic@mpe.mpg.de |


**Educational qualifications**

| | |
|---|---|
| 1994 – 1998 | Secondary education<br>Gymnasium Svetozar Marković, Niš, Serbia |
| 1998 – 2005 | Masters of Science<br>Faculty of Natural Science, Department of Physics, Niš University, Serbia<br>Diploma thesis: Detection of Space and Time Evolution of Glow Discharge in Neon Filled Diode |
| 2006 – 2010 | PhD student<br>Thesis topic: Physical Processes in Complex Plasma<br>Thesis supervisor: Prof. Dr. Gregor Morfill<br>Place: Max-Planck-Institut für extraterrestrische Physik, Garching and Ludwig-Maximilians-Universität, München, Germany |

**Awards**

| | |
|---|---|
| 2006 | Research Assistant, Faculty of Natural Science, University Niš |

**Working experience**

| | |
|---|---|
| 2003 – 2006 | Research<br>Laboratory for Physics of Ionized Gasses,<br>Department of Physics, University Niš, Serbia |

# Publication list

## 5.1 Publication in refereed journals:

1. S. Mitić, B. A. Klumov, M. Y. Pustylnik and G. E. Morfill, Determination of electron temperature in low-pressure plasmas by means of optical emission spectroscopy, JETP Lett. *in print*, (2010)

2. S. Mitić, M. Y. Pustylnik and G. E. Morfill, Spectroscopic evaluation of the effect of the microparticles on radiofrequency argon plasma, New J. Phys. **11**, 083020 (2009).

3. S. Mitić, B. A. Klumov, U. Konopka, M. H. Thoma and G. E. Morfill, Structural properties of complex plasmas in a homogeneous dc discharge, Phys. Rev. Lett. **101**, 125002 (2008)

4. S. Mitić, R. Sütterlin, A. V. Ivlev, H. Höfner, M. H. Thoma, S. Zhdanov and G. E. Morfill, Convective dust clouds driven by thermal creep in a complex plasma, Phys. Rev. Lett. **101**, 235001 (2008).

5. M. K. Radović, Č. Maluckov, S. Mitić and B. Trajković, Two step current increases in glow discharge development in neon filled diode at 4 mbar, Facta Universitatis, **5**, 1, (2007).

6. S. Mitić, Č. Maluckov and M. K. Radović, Investigation of early multiplication processes of the glow discharge formation in neon filled diode at 1.33 mbar pressure, Contrib. Plasma Physics, **46**, 4, (2006).

## 5.2 Publication in conference proceedings:

1. S. Mitić, M. Y. Pustylnik and G. E. Morfill, Diagnostics of the Influence of Levitating Microparticles on the Low Pressure rf argon Plasma, 10th Workshop on Fine Particle Plasma, Toki, Japan, 2009.

2. S. Mitić, M. Y. Pustylnik and G. E. Morfill, Spectroscopic Evaluation of the Influence of the Effect of the Microparticles on the Plasma, Frontiers of Low Temperature Plasma Diagnostic, Blansko, Czech Republic, 2009.

3. S. Mitić, B. A. Klumov, U. Konopka, M. H. Thoma and G. E. Morfill, 3D Complex Plasma i Low Frequency Discharge, Contributed papers of 24nd International Symposium on the Physics of Ionized Gases, Novi Sad, Serbia, 2008.

4. S. Mitić, B. A. Klumov, U. Konopka, M. H. Thoma and G. E. Morfill, Super Cooled (Glassy) State of Complex Plasma, 5th International Conference on Physics of Dusty Plasmas, Ponta Delgada, Portugal, 2008.

5. S. Mitić, A. V. Ivlev, H. Höfner, M. H. Thoma, S. Zhdanov and G. E. Morfill, Convective dust clouds in a complex plasma, The 9th International Workshop on the Interrelationship between Plasma Experiments in Laboratory and Space, Palm Cove Resort, Cairns, Australia, 2007.

6. M. K. Radović, Č. Maluckov, S. Mitić and S. Rančev, Temporal and Spatial Formation of the Glow Discharge in Neon Filled Diode at 1.33 mbar, Contributed papers of 22nd International Symposium on the Physics of Ionized Gases, National Park Kopaonik, Serbia, 2006, pp. 371-374.

7. S. Mitić, Č. Maluckov and M. K. Radović, Electrical Gas Discharge Under Non SelfSustaining Conditions in Neon, Contributed papers of 22nd International Symposium on the Physics of Ionized Gases, National Park Tara, Serbia, 2004, Editor Lj. Hadžijevski, pp. 385-388

# Enclosed papers

This cumulative thesis consists of following papers which are attached afterwords.

## Copyright notice

Reprinted with permission from

- S. Mitić, B. A. Klumov, U. Konopka, M. H. Thoma and G. E. Morfill, Structural Properties of Complex Plasmas in a Homogenious Discharge, PRL **101**, 125002 (2008).
- S. Mitić, R. Sutterlin, A. V. Ivlev, H. Hofner, M. H. Thoma, S. Zhdanov and G. E. Morfill, Convection Dust Slouds Driven bt Thermal Creep in a Complex Plasma, Phys. Rev. Lett. **101**, 235001 2008.
- S. Mitić, M. Y. Pustylnik and G. E. Morfill, Spectroscopic Evaluation of the effect of the microparticles on radiofrequency argon plasma, New Journal of Phyisiccs, **11**, 083020, 2009
- S. Mitić, B. A. Klumov, M. Y. Pustylnik and G. E. Morfill, Determination of electron temperature in low-pressure plasmas by means of optical emission spectroscopy, JETP Lett. *in print*, 2010

# Structural Properties of Complex Plasmas in a Homogeneous dc Discharge

S. Mitic, B. A. Klumov, U. Konopka, M. H. Thoma, and G. E. Morfill
*Max-Planck-Institut für Extraterrestrische Physik, D-85741 Garching, Germany*
(Received 9 April 2008; published 16 September 2008)

We report on the first three-dimensional (3D) complex plasma structure analysis for an experiment that was performed in an elongated discharge tube in the absence of striations. The low frequency discharge was established with 1 kHz alternating dc current through a cylindrical glass tube filled with neon at 30 Pa. The injected particle cloud consisted of monodisperse microparticles. A scanning laser sheet and a camera were used to determine the particle position in 3D. The observed cylindrical-shaped particle cloud showed an ordered structure with a distinct outer particle shell. The observations are in agreement with performed molecular dynamics simulations.

DOI: 10.1103/PhysRevLett.101.125002 PACS numbers: 52.27.Lw

Since the discovery of plasma crystals, many experiments have been performed to quantify the crystalline state of complex plasmas by means of analyzing the scattered laser light of the microparticles that were introduced in the plasma environment. Most of these experiments were related to two-dimensional (2D) systems (e.g., [1–5]). Only a few experiments were focused on the analysis of 3D structures [6–14]. Extensive analysis on the crystallization phase transition by means of structural properties of a substantial particle cloud has been performed for 2D—[3] as well as 3D [12]—particle systems in radio-frequency discharges (the analysis of the 3D particle system was based on a 2D cross section analysis). A full 3D reconstruction has so far been reported only for systems smaller than a few hundred particles [10,15]. For dc discharges, crystalline systems have been investigated only in striations [8] or in double dc-plasma environments [16]. However, a full 3D structure analysis of these systems has not been performed.

Here we present for the first time a full 3D reconstruction of a microparticle cloud in a low frequency discharge plasma. In contrast to typical complex plasma experiments in dc discharge tubes [8], the particles in the experiment described here were not levitated in striations, where strong variations in the electric field lead to inhomogeneities in particle clouds even on small scales. Instead, the particles were confined in a horizontally mounted discharge tube, levitated by the radial electric field of the plasma sheath that was aligned with the tube walls. The discharge conditions were selected in a way that no striations were present in the positive column. In this way, large homogeneous particle clouds could be established.

The experiment setup was similar to the dc discharge experiment facility "PK-4" [17] that is being developed for complex plasma microgravity experiments aboard the International Space Station. The heart of the setup was given by a "*U*"-shaped discharge glass tube as sketched in Fig. 1. The discharge tube was filled with Ne at a pressure of 30 Pa using a flow controller for gas inlet on one side of the tube and a vacuum pump on the other side. For stability reasons, the gas inlet as well as the pump could be disconnected by valves so that experiments without gas flow but with stable discharge conditions could be performed. The stability period was about 10 minutes with closed valves. After this time, gas refreshment was necessary to avoid plasma parameter drift.

To ignite a plasma, a voltage of about 1000 V was applied along the discharge tube between the driven electrodes. This corresponded in our case to a dc current of 1 mA through the plasma. Under these circumstances, a longitudinal electric field is present in the discharge accompanied by a substantial directed ion flow. Since charged microparticles react to the electric fields as well as the ion flow, no steady-state conditions for microparticles introduced in the discharge can be reached in such a case. To compensate the effects of the longitudinal electric

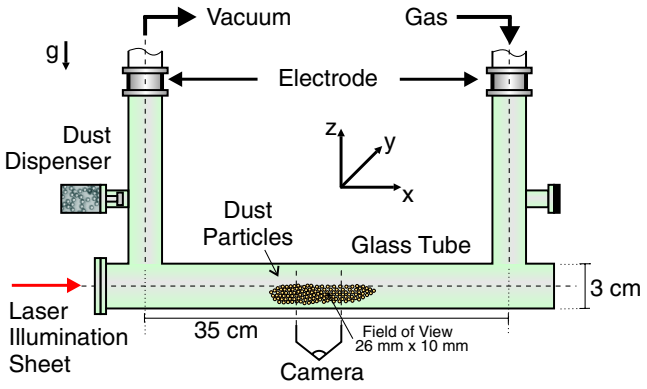


FIG. 1 (color online). Experimental setup. The tube had an inner diameter of 30 mm and a length of 750 mm with electrodes on both ends. The part of the discharge tube that was aligned perpendicular to the gravity vector had a length of about 350 mm with flat windows at the sides for optical illumination and observation purposes. To assure clean gas conditions, the discharge tube was always evacuated for several hours before each experiment, reaching base pressures below $10^{-3}$ Pa.

 

fields on particles in the plasma, the polarity of the voltage between the electrodes was switched with a frequency of 1 kHz. This frequency is far above the response frequency of the "heavy" microparticles in the experiments, so that the particles "see" a time-averaged zero longitudinal electric field and ion flow.

The particle cloud consisted of monodisperse, spherical melamine formaldehyde micron-sized particles of radius $r_p = (2.4 \pm 0.1)\ \mu$m and mass density $\rho_p = 1.51\ \mathrm{g/cm^3}$. The particle injection was via a dispenser mounted on one side of the glass tube. By changing the duty cycle of the polarity-switched plasma current, a time-averaged net force along the tube can be set. As a result, the particle cloud can be moved to any desired position within the tube. Our experiments were conducted with the particle cloud in the center of the discharge tube which was horizontally aligned. The particle cloud is then confined by the radial electric field of the sheath as well as horizontally by a weak confinement potential caused by the bends in the glass tube on both sides. The overall shape of the particle cloud represented the confinement structure in the discharge tube. The thickness and density of the cloud was higher in its center, while its size reduced to a few layers or even a single particle string at both ends. Typical length of the dust cloud was about 10 cm.

The particles were illuminated by a horizontally aligned sheet of laser light with a power of ~20 mW at a wavelength of 686 nm. The minimal thickness of the illumination sheet was about $\delta_L = (150 \pm 30)\ \mu$m. The positions of the particles were recorded with 50 frames per second by a camera that had a field of view of 26 mm along the tube and 10 mm across it.

Both camera and laser were attached to a translation stage that allowed for scans in height with a constant velocity while keeping the relative positions of camera and laser sheet fixed. The optimal scanning velocity was found to be 0.2 cm/s for two reasons. First, the velocity has to be low enough that the same particles appear at least in a few consecutive frames of the scan, and, second, the particle motion time (changes in 3D structure) is large compared to the scanning time. To determine the full spatial position of each particle, every particle position within each frame of a scan was identified. Using a correlation analysis, corresponding particles in consecutive frames were identified, and from these particle tracks the three-dimensional particle positions were calculated using the (light) intensity weighted $x$ and $y$ positions and frame number, which is related by the scanning velocity with the $z$ coordinate. This diagnostic method has been also used in our group by Zuzic *et al.* [7].

After injection of the particles and positioning of the particle cloud, the particles within the cloud did not have a well defined arrangement; i.e., the cloud was in a disordered state. A few minutes later, the first layers started to separate in the upper part of the particle cloud. About 10 minutes after injection, the system showed a partly ordered structure. At this time, a scan was performed shortly before the gas refreshment cycle that would destroy the structure of the particle system. The three-dimensional positions of the particles in the observed part of the cloud are presented in Fig. 2. Particle positions are overlaid for all microspheres in the cloud showing the projection of the system in the side view and top view (images in Fig. 2, upper part and lower part, respectively). As can be clearly seen, the particles in the bulk of the cloud represent a kind of vertically orientated structure with a single distinct outer particle layer that represented the structure of the radial confinement across the discharge tube.

To be able to compare the structural properties with molecular dynamics (MD) simulations, we had to estimate the corresponding experiment parameters. Using plasma parameter measurements from Ref. [18] (obtained using the same experimental setup), we estimate for the pressure of 30 Pa and the discharge current of 1 mA an electron and ion density of $n_e \approx n_i \approx 10^8\ \mathrm{cm^{-3}}$, an electron temperature of $T_e \approx 6$ eV, and an ion temperature of $T_i \approx 0.03$ eV. The corresponding characteristic length scales were $\lambda_D = 120\ \mu$m for the combined Debye length ($\lambda_D = 1/\sqrt{1/\lambda_{De}^2 + 1/\lambda_{Di}^2}$, where subscript $e$ stands for electron and $i$ for ion) and $\lambda_{imfp} = 180\ \mu$m for the ion mean free

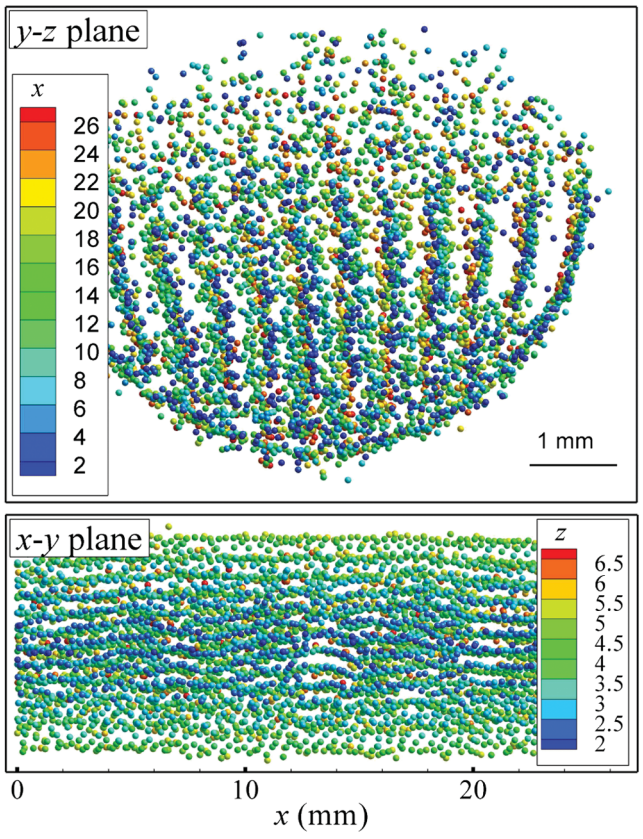


FIG. 2 (color). Experimentally recorded particle positions in the $y$-$z$ and $x$-$y$ planes (see orientation in Fig. 1). Particles are color-coded by corresponding third coordinate presented in millimeters. About 6000 particles were detected.

path. Using a 3D pair correlation analysis, we obtained for the interparticle distance $\Delta \approx 500\ \mu$m. From the "orbit motion limited" equation [19] and taking into account a correction for the charge reduction as obtained in Ref. [20] for the ratios $r_p/\lambda_D \approx 0.02$ and $\lambda_D/\lambda_{imfp} \approx 0.7$, we estimated the charge of the particles to have been $Z_d \simeq 5 \times 10^3$ electrons. As a result, we could calculate the coupling parameter $\Gamma \simeq 10$, using the definition $\Gamma = Z_D^2 \exp(-k)/\Delta T_d$, where $k = \Delta/\lambda_D \approx 4$. This would theoretically represent a liquid state.

For the molecular dynamic simulations, we assumed that all microparticles have the same charge $Z_d = 3 \times 10^3 e$, where $e$ is the electron charge, and the pair interaction between the particles is described by a screened Coulomb (Yukawa) potential $\phi(r) = Z_d/r \exp(-r/\lambda_D)$, with $r$ the distance between the particles and $\lambda_D$ the screening length. The system of equations

$$m\ddot{\mathbf{r}}_i = -Z_d \sum \nabla\phi - m\gamma\dot{\mathbf{r}}_i - m\mathbf{g} + \mathbf{L}_i \qquad (1)$$

was solved for each particle using the standard Verlet algorithm, where $\gamma$ describes Epstein friction. The terms on the right-hand side of Eq. (1) describe the electrostatic interaction between particles, neutral drag, gravity, and the stochastic Langevin force (thermal noise induced by particle collision with the neutral gas) defined from $\langle \mathbf{L}_i(t)\mathbf{L}_j(t+\tau)\rangle = 2\gamma m k_B T \delta_{ij}\delta(\tau)$, with the zero-mean condition $\langle \mathbf{L}_i(t)\rangle = 0$ (e.g., [21]).

Initially $N = 6000$ particles were randomly distributed over a cylinder of radius $r_c \sim 1$ cm. Periodical boundary conditions along $z$ and parabolic confinement in the $x$-$y$ plane were used. The parameters were similar to those of the experiment (particle size, mean interparticle distance $\Delta$, neutral gas density). Figure 3 shows typical particle positions at the steady-state stage for $\Gamma \simeq 10$.

3D particle positions can be used to define the local order of particles, which in turn gives us the key information about the phase state of the system to be investigated.

To determine the local order of the particles, a bond order parameter method is used [22]. In the framework of this method, the local rotational invariants for each particle

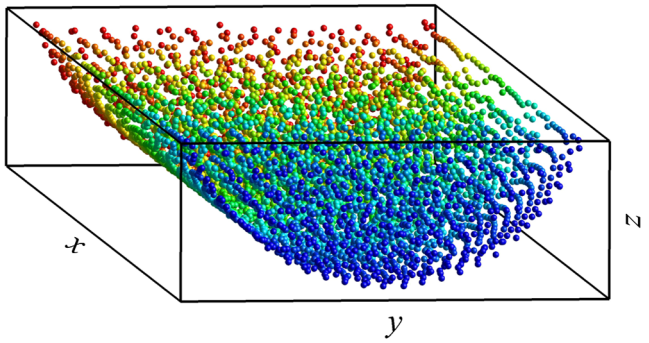


FIG. 3 (color online). MD simulations of the Yukawa system of dust particles. Snapshot of particle positions at steady-state stage.

are calculated and compared with those for ideal lattice types such as fcc/hcp/bcc. Local rotational invariants of second order $q_l(i)$ and third order $w_l(i)$ are calculated for each particle $i$ by using $N_b(i)$ nearest neighbors:

$$q_l(i) = \left(\frac{4\pi}{(2l+1)}\sum_{m=-l}^{m=l}|q_{lm}(i)|^2\right)^{1/2}, \qquad (2)$$

$$w_l(i) = \sum_{\substack{m_1,m_2,m_3 \\ m_1+m_2+m_3=0}} \begin{bmatrix} l & l & l \\ m_1 & m_2 & m_3 \end{bmatrix} q_{lm_1}(i) q_{lm_2}(i) q_{lm_3}(i), \qquad (3)$$

where $q_{lm}(i) = \frac{1}{N_b(i)}\sum_{j=1}^{N_b(i)} Y_{lm}(r_{ij})$ and $Y_{lm}$ are the spherical harmonics and $r_{ij} = r_i - r_j$, where $r_i$ are the coordinates of $i$th particle. In Eq. (3),

$$\begin{bmatrix} l & l & l \\ m_1 & m_2 & m_3 \end{bmatrix}$$

are the Wigner $3j$ symbols, and the summation in the latter expression is performed over all indices $m_i = -l, \ldots, l$, that satisfy the condition $m_1 + m_2 + m_3 = 0$.

To define the local order around a particle, we used $q_4$, $q_6$, and $w_4$. Figure 4 shows the simulated distributions of a Yukawa system of particles in the $q_4 - q_6$ plane for a liquidlike system ($\Gamma \sim 1$) [Fig. 4(b)] and a crystallized one ($\Gamma \simeq 10^4$) [Fig. 4(a)]. Results of the experiment are

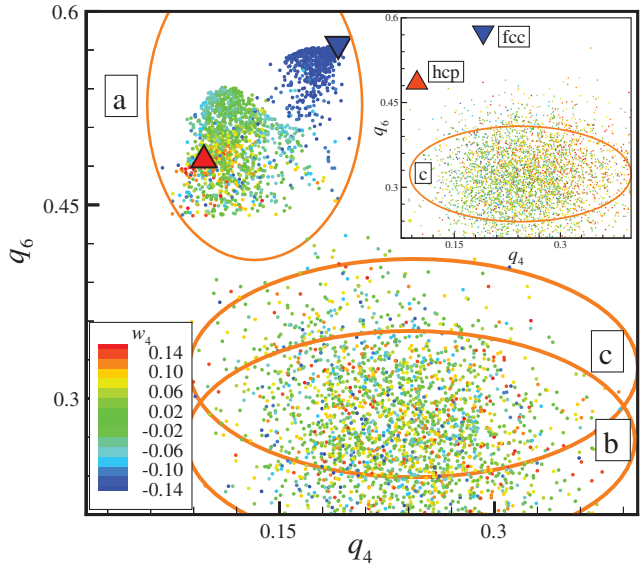


FIG. 4 (color). Distribution of dust particles at different values of $\Gamma$ in the plane of local order parameters $q_4 - q_6$ (calculated by using 12 nearest neighbors) as seen from MD simulations of Yukawa systems of particles together with experimental data. Scattered data are color-coded by the third-order rotational invariant $w_4$ value. Data for ideal hcp ($\triangle$) and fcc ($\nabla$) are also plotted. Distribution (b) shows liquidlike system with $\Gamma \sim 1$, while case (a) corresponds to a crystallized Yukawa system with $\Gamma \simeq 10^4$. Experimental data are scattered within the area marked with (c) and in detail presented in the inset.

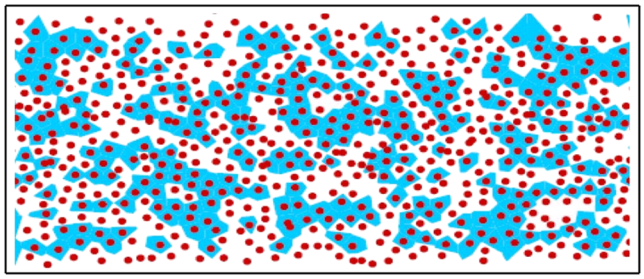

FIG. 5 (color online). Particle arrangement in the unfolded outer shell representation where shaded areas represent particles with 6 nearest neighbors.

plotted revealing liquidlike behavior of the observed data [Fig. 4(c)]. To obtain the crystallized Yukawa system, we performed 3D MD simulations of 6000 particles in a box with external confinement of a hard wall type in the vertical direction ($z$) with periodic boundary conditions in the horizontal ($x$ and $y$) directions.

From both projections presented in Fig. 2, some macrostructures are visible. In the $y$-$z$ projection, formation of layers is very well pronounced. In the central part of the cloud, layers are parallel, while on the ends in the radial direction they are curved following the shape of the confinement. Outer particles form a shell structure around these layers, and the shape of this shell is strongly dependent on the plasma confinement and particle number [23]. In a first step, the shell was unfolded, and then a triangulation and Voronoi analysis were done. The particle arrangement in this unfolded shell was analyzed, and the results are presented in Fig. 5. The shaded area around the particles represents particles which have 6 nearest neighbors, and they make up about 50% of all particles in this shell. About 25% of all particles have 5 neighbors, and about 20% have 7 neighbors. For a 2D plane, a sixfold structure represents the ground state in the crystal state, so the percentage of the sixfold structure can be used for the determination of the coupling parameter $\Gamma$ [24]. By comparing this results with simulations [24], the value of $\Gamma$ in this measurement is estimated to be about 10, which is consistent with our independent estimations based on the plasma parameters.

In this Letter, we presented the first 3D analysis of a complex plasma in a dc discharge environment. The discharge was switched at a rate of 1 kHz to produce striation-free plasma. The 3D analysis of the particle cloud showed a liquidlike structure with locally enhanced structural properties that indicated that the system was near crystallization. Molecular dynamics simulations were performed taking into account the experimental conditions. The simulated and experimental results were analyzed using methods to quantify the dynamical properties of liquidlike or glassy systems. Simulation and experiment showed good agreement. In addition, both showed a transition of a more structural particle arrangement from the outside of the particle cloud to a more irregular arrangement on the inside. On the outside, a shell-like structure could be observed. This could be of special interest, since it suggests that physical properties such as the shear viscosity might be anisotropic. The observed shell structure does not contradict the liquid behavior of the system, since it consists of only a few layers corresponding to a real liquid on the nanoscale. Thus confined complex plasma systems might help us to understand similar generic properties of other cylindrical-shaped systems, particularly those on the nanometer scale.

We acknowledge the support of DLR under Grants No. 50 WM 0504 and No. 50 WP 0700.

[1] H. M. Thomas and G. E. Morfill, J. Vac. Sci. Technol. A **14**, 501 (1996).
[2] G. E. Morfill, H. M. Thomas, U. Konopka, and M. Zuzic, Phys. Plasmas **6**, 1769 (1999).
[3] C. A. Knapek *et al.*, Phys. Rev. Lett. **98**, 015004 (2007).
[4] V. Nosenko, S. Zhdanov, and G. Morfill, Phys. Rev. Lett. **99**, 025002 (2007).
[5] A. Melzer, Phys. Rev. E **67**, 016411 (2003).
[6] Y. Hayashi, Phys. Rev. Lett. **83**, 4764 (1999).
[7] M. Zuzic *et al.*, Phys. Rev. Lett. **85**, 4064 (2000).
[8] V. E. Fortov *et al.*, in *Dusty Plasmas in the New Millenium: Third International Conference on the Physics of Dusty Plasmas* (AIP, New York, 2002).
[9] Y. Hayashi, in *Non-Neutral Plasmas Physics IV* (AIP, New York, 2002).
[10] O. Arp, D. Block, A. Piel, and A. Melzer, Phys. Rev. Lett. **93**, 165004 (2004).
[11] M. H. Thoma *et al.*, Am. J. Phys. **73**, 420 (2005).
[12] M. Rubin-Zuzic *et al.*, Nature Phys. **2**, 181 (2006).
[13] A. P. Nefedov *et al.*, New J. Phys. **5**, 33.1 (2003).
[14] G. E. Morfill *et al.*, in *Dusty Plasmas in the New Millenium: Third International Conference on the Physics of Dusty Plasmas*, AIP Conf. Proc. No. 649, edited by R. Bharuthram, F. Verheest, P. K. Shukla, and M. A. Hellberg (AIP, New York, 2002), p. 91.
[15] T. Antonova *et al.*, Phys. Rev. Lett. **96**, 115001 (2006).
[16] N. Sato, G. Uchida, R. Ozaki, and S. Lizuka, in *Physics of Dusty Plasmas* (AIP, New York, 1998).
[17] M. H. Thoma *et al.*, IEEE Trans. Plasma Sci. **35**, 255 (2007).
[18] V. E. Fortov *et al.*, Plasma Phys. Controlled Fusion **47**, B537 (2005).
[19] T. Matsoukas and M. Russell, J. Appl. Phys. **77**, 4285 (1995).
[20] B. Rovagnati, M. Davoudabadi, G. Lapenta, and F. Mashayek, J. Appl. Phys. **102**, 073302 (2007).
[21] B. Smit and D. Frenkel, *Understanding Molecular Simulation* (Academic, San Diego, 2002).
[22] P. Steinhardt, D. Nelson, and M. Ronchetti, Phys. Rev. Lett. **47**, 1297 (1981).
[23] Shell-like structures in complex plasmas have also been observed in an rf discharge, where a limited number of microparticles was spherically confined [10].
[24] B. A. Klumov and G. E. Morfill, JETP Lett. **85**, 498 (2007).

# Convective Dust Clouds Driven by Thermal Creep in a Complex Plasma

S. Mitic, R. Sütterlin, A. V. Ivlev H. Höfner, M. H. Thoma, S. Zhdanov, and G. E. Morfill

*Max-Planck-Institut für extraterrestrische Physik, D-85741 Garching, Germany*

(Received 5 February 2008; published 1 December 2008)

Steady-state clouds of microparticles were observed, levitating in a low-frequency glow discharge generated in an elongated vertical glass tube. A heated ring was attached to the tube wall outside, so that the particles, exhibiting a global convective motion, were confined vertically in the region above the location of the heater. It is shown that the particle vortices were induced by the convection of neutral gas, and the mechanism responsible for the gas convection was the thermal creep along the inhomogeneously heated tube walls. The phenomenon of thermal creep, which commonly occurs in rarefied gases under the presence of thermal gradients, should generally play a substantial role in experiments with complex plasmas.

DOI: 10.1103/PhysRevLett.101.235001 PACS numbers: 52.27.Lw

Convective motion of dust particles in complex (dusty) plasmas is a phenomenon that is often observed in very different experimental conditions. In particular, vortices in complex plasmas can be produced both in ground-based laboratories and under microgravity conditions, in dc and rf discharges of fairly different configuration, upon inhomogeneous heating, and in rather isothermal environments [1].

There are many publications, both theoretical and experimental, in which the origin of the vortex motion in complex plasmas has been investigated [2–11]. Basically, there are several mechanisms that can produce vortices: This can be due to the presence of nonpotential force(s) exerted on charged dust particles in the discharge (caused by inhomogeneous charges [7] or ion drag [9]), because of the convective motion of the background neutral gas or microparticles themselves [12], or due to a dissipative instability [10,11], affecting dust rotations with angular velocities decreasing with pressure [10,11]. This clearly indicates that the nature of such vortices—despite a quite similar appearance—might be very different.

In this Letter, we report on a recent series of experiments performed in a low-frequency glow discharge under gravity. We investigate the convective motion of dust particles in the presence of an external controllable heating and unambiguously show that under such conditions vortices in complex plasmas occur due to the neutral gas convection, with clouds of microparticles resembling convective clouds in the atmosphere (produced from, e.g., warm air pockets rising upwards and composed of water droplets, ice crystals, ice pellets, etc.). An important conclusion of our research is that the neutral gas convection is triggered by the *thermal creep*. This phenomenon occurring in rarefied gases under inhomogeneous heating is very different from conventional (Rayleigh) mechanisms for convection. We suggest that the thermal creep can be an essential factor in determining steady-state configurations of complex plasmas.

The experiments were conducted in a complex plasma produced by a low-frequency discharge in neon gas (with constant pressure between 30 and 100 Pa) of the PK-4 facility [13,14]. The plasma chamber consists of an elongated glass tube as shown in Fig. 1.

A gas discharge was maintained between the electrodes by a regulated discharge current of 1 mA. The discharge voltage polarity was changed with a frequency of 1 kHz (50% duty cycle). This frequency is more than an order of magnitude higher than the dust-plasma (response) frequency [1], so that the effective longitudinal force on microparticles (electric plus ion drag) vanishes.

In the course of the experiments, dust particles (spherical melamine-formaldehyde particles with a mass density of 1.51 g/cm$^3$) of two different radii $r_p = 1.64$ or

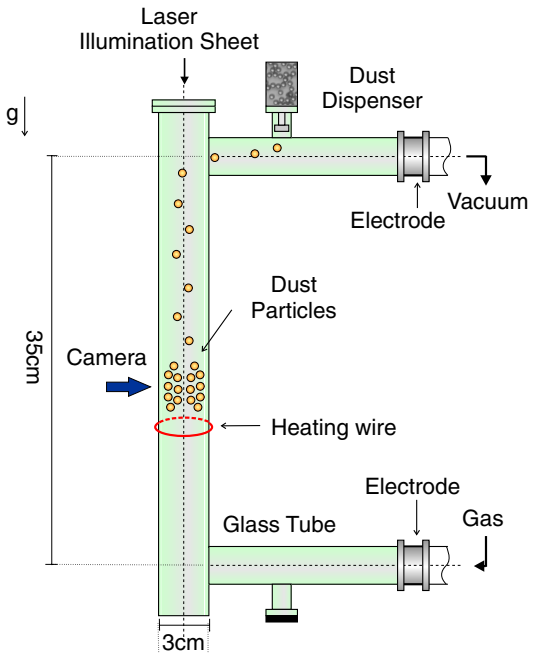


FIG. 1 (color online). Experimental setup.

 

3.05 $\mu$m were injected by a dispenser from above into the plasma and confined inside the vertical glass tube. The dust particles were illuminated along the tube axis by a laser sheet (wavelength 686 nm, power 20 mW, thickness 100 $\pm$ 30 $\mu$m, and width 15 mm), and the images were recorded by a PCO 1600 camera.

A metal wire (alloy of 70% Ni, 11% Fe, and 14% Cu and 0.5 mm in diameter) was put around the lower part of the tube to produce a temperature gradient. A dc current between 0.5 and 1.8 A was applied to this wire using a 10 V power supply. For avoiding unwanted electromagnetic effects on the plasma, only one loop of the wire (one-turn coil) was attached. The wire was insulated electrically (but not thermally) against direct contact to the tube walls.

Because of the gas temperature gradient, a thermophoretic force acts on the dust particles [15]:

$$\mathbf{F}_{\mathrm{th}} = -\gamma_{\mathrm{th}} \nabla T_n, \tag{1}$$

where $\gamma_{\mathrm{th}}[\mathrm{N\,cm/K}] \simeq 2.17 \times 10^{-6} (r_p[\mu\mathrm{m}])^2$ [16]. The thermophoretic force required to levitate particles is $F_{\mathrm{th}} = m_p g \simeq 2.74 \times 10^{-13}$ N for the smaller ones and $\simeq 1.76 \times 10^{-12}$ N for the larger ones ($m_p$ is the particle mass). According to (1), temperature gradients of $|dT/dz| \simeq 4.65$ K/cm for the smaller particles and $\simeq 8.64$ K/cm for the larger ones are required to compensate gravity.

The measured temperatures along the tube and the temperature gradients are shown in Fig. 2, where $z = 0$ is the position of the heating wire. It turns out that the maximum values of the temperature gradients are smaller than those necessary for thermophoretic levitation. Nevertheless, we observe that the particle cloud is confined in the area above the heating wire. Figure 3 shows vertical cross sections through the center of the clouds obtained for different pressures. As pointed out above, plasma forces cannot be responsible for this effect: Because of the fast polarity switching, neither an electric force nor an ion drag force [17] could support the levitation.

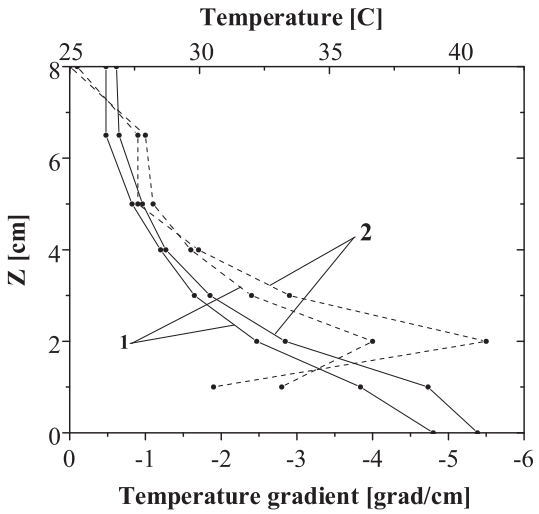


FIG. 2. Measured temperatures (solid lines) and calculated temperature gradients (dashed lines) for particles of (1) $r_p = 1.64$ $\mu$m and (2) $r_p = 3.05$ $\mu$m.

The dust particles are frictionally coupled to the neutral gas. Therefore, it is natural to assume that the intense convective motion of the particles seen in Fig. 3 is induced by the gas motion, which, in turn, is triggered by the local tube heating. Favorably directed, the gas convection could result in a global dust rotation and also contribute to the levitation of the particles, in addition to the thermophoresis. (Note that $\mathbf{F}_{\mathrm{th}}$ alone cannot cause the convection, because it is a potential force: $\nabla \times \mathbf{F}_{\mathrm{th}} \equiv 0$.)

The neutral drag force acting on a spherical particle is [18]

$$\mathbf{F}_n = \gamma_n (\mathbf{v}_f - \mathbf{v}_p), \tag{2}$$

where $\mathbf{v}_f$ is the velocity of gas flow, $\mathbf{v}_p$ is the particle velocity, and the Epstein friction coefficient for neon at room temperature reads $\gamma_n[\mathrm{N\,s/cm}] \simeq 2.7 \times 10^{-16} (r_p[\mu\mathrm{m}])^2 p[\mathrm{Pa}]$.

Note that the radial electric field of discharge exerts an additional force $F_r$ [19] which confines the particle cloud in radial direction. We observed that the dust particles after switching off the discharge expand across the tube, and particles keep rotating one or two cycles before eventually falling down.

In order to verify the hypothesis of the neutral gas convection as the principal mechanism responsible for the observed particle dynamics, we will analyze in detail one of our experiments performed with 3.05 $\mu$m particles at a pressure of 50 Pa.

As the first step, we determine the velocity field $\mathbf{v}_f$ of the convective gas flow and the radial electric force $F_r$. The particle motion is recorded at a frame rate of 500 frames/s in the course of the experiment comprising two separate cases: with and without plasma. The particles are detected in each frame, and then, based on the position of each particle in a few consecutive frames, their velocities and accelerations are extracted. Based on these data, the particle velocity profiles are reconstructed in the entire cloud. Particle velocities and accelerations are derived by fitting cubic splines to the complete particle trajectories.

The dynamics of individual particles (assuming weak interparticle interaction) is determined by the balance of forces:

$$m_p \ddot{\mathbf{r}} = \mathbf{F}_{\mathrm{th}} + \mathbf{F}_n + \mathbf{F}_r + m_p \mathbf{g}. \tag{3}$$

To separate the remaining unknown forces—the radial electric force and the neutral drag force—appearing in Eq. (3), we analyze first the data when no plasma was in the tube, and, hence, no radial electric force ($F_r = 0$) acts on the particles. This allows us to get the velocity field of the conveying gas molecules. With this information and assuming that switching on and off the plasma does not alter the gas convection, we calculate the radial electric force of the plasma in the region where particle trajectories recorded with and without plasma overlap, as shown in

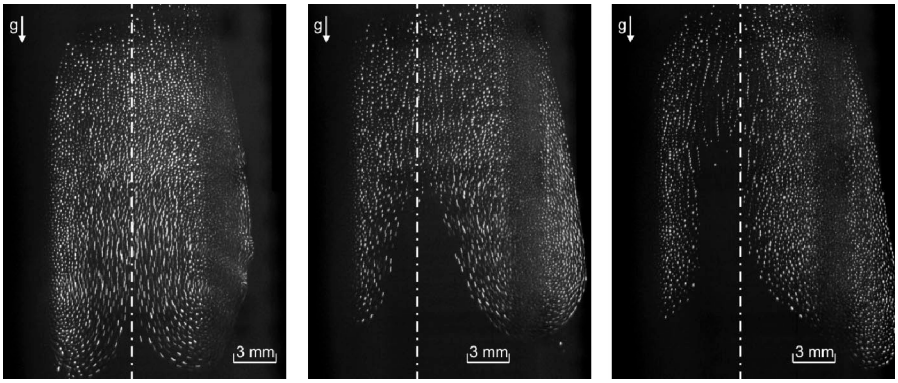


FIG. 3. Dust clouds of $r_p = 1.64$ $\mu$m particles at pressures of 30, 50, and 100 Pa (from left to right). The vertical dashed-dotted lines indicate the center of the tube. The field of view is $21 \times 26$ mm.

Fig. 4. In Fig. 4(a), the particle cloud in the presence of the plasma is a bit higher and further away from the tube wall. After switching off the plasma [Fig. 4(b)], particles come closer to the wall and the cloud expands further down. For the overlapping region, any differences in the particle motion between the cases with and without plasma must be due to electrical forces, since neither the temperature distribution nor the gas velocity field are affected by the discharge.

Figure 5 shows the velocity field of the gas convection as calculated for the case without plasma. The particle trajectories are overplotted. The distribution of flow velocities has a clear rotational tendency. Since the neutral drag force on the particles depends on the relative velocities of the particles and gas, the particles do not follow the gas flow but rotate eccentrically from the center of gas convection in the area of upward gas draft.

The radial force on the particles when plasma is on can now be fitted using the gas flow velocities in the overlapping region. Figure 6 shows that the radial force is zero at the tube axis and rapidly increases towards the tube walls.

The results obtained above clearly demonstrate the presence of gas convection. This is not free convection, though, merely because the onset of free convection is too high in terms of the critical Rayleigh number to cause gas flow under the conditions of our experiments. It is well known, however, that if one puts a nonuniformly heated body in a rarefied gas, the gas starts moving along the body *in the direction* of the temperature gradient [20–22]. This phenomenon is referred to as *thermal gas creep* (or *thermal gas slip*). It was predicted theoretically by Maxwell [23] and verified experimentally by Reynolds [24] and is governed by the relation

$$V_{\mathrm{TC}} = K_{\mathrm{TC}} \nu \nabla_{\parallel} \ln T_W, \tag{4}$$

where $V_{\mathrm{TC}}$ is the velocity of creep at the body surface, $\nu$ is the kinematic viscosity of the gas, $T_W$ is the temperature of

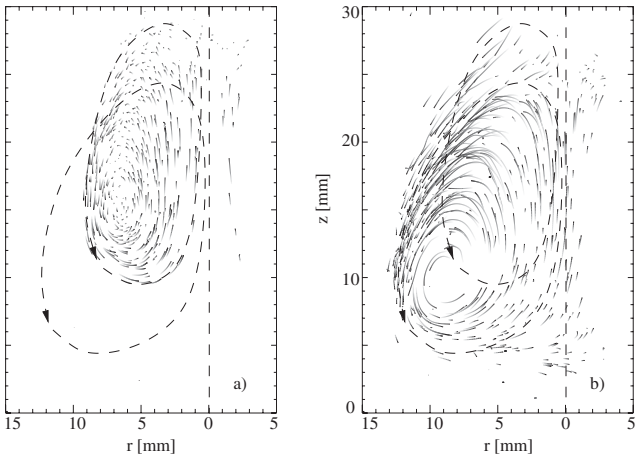


FIG. 4. Convective dust clouds of $r_p = 3.05$ $\mu$m particles at a pressure of 50 Pa for cases (a) "plasma on" and (b) "plasma off." The shape of the cloud and direction of the rotation in the "on" and "off" cases are indicated by the upper and lower loops, respectively, and their overlap shows the region used for the reconstruction of radial electric force (see Fig. 6). The vertical dashed lines show the center of the tube.

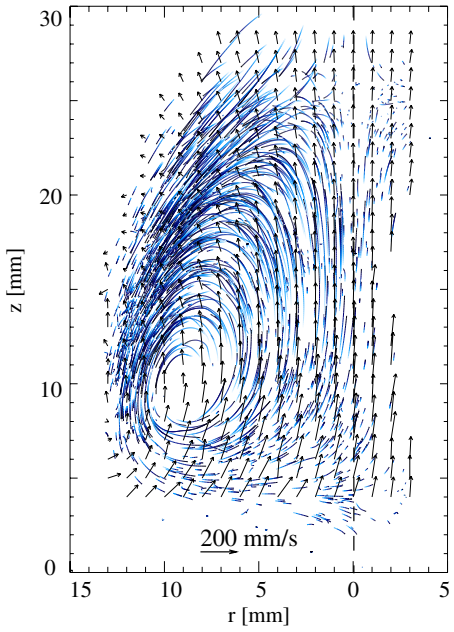


FIG. 5 (color online). Averaged gas flow velocity field (vectors) superimposed with particle trajectories. The vertical dashed line indicates the center of the tube.

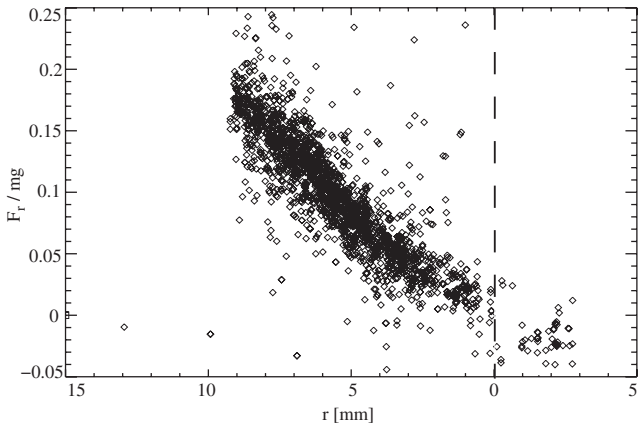


FIG. 6. Reconstructed radial force for the overlapping region. The vertical dashed line indicates the center of the tube.

the heated body, i.e., the glass walls in our case, and $\|$ indicates the component of the gradient along the surface. For a long tube, the radial distribution of the (longitudinal) velocities is well known: $v_z = V_{\mathrm{TC}}(2r^2/R^2 - 1)$ [22]. In our geometry, the vertical temperature gradient is negative: $dT_W/dz < 0$ (see Fig. 2). Hence, the gas should flow downwards along the tube walls with $v_z(R) = V_{\mathrm{TC}}$ and upwards near the tube axis with $v_z(0) = -V_{\mathrm{TC}}$, which is in agreement with our observations (see Fig. 5). For a quantitative comparison with the experiment, we rewrite Eq. (4) in the following form: $K_{\mathrm{TC}} = |V_{\mathrm{TC}}/\nu\nabla_z \ln T_W|$. Based on the experimental data shown in Figs. 2 and 5, we get $K_{\mathrm{TC}} \simeq 1$, which coincides with theoretical expectations ($K_{\mathrm{TC}}$ should be in the range of 0.7–1.2 [21]). Moreover, the magnitude of the convection velocity decreases monotonically with pressure, which is also in line with theory: Combining Eqs. (3) and (4), we obtain that the velocity should scale as $\propto p^{-1}$, which is in good agreement with our measurements shown in Fig. 7. (Note that the conventional Rayleigh mechanism predicts the opposite tendency, when the velocity increases with pressure.)

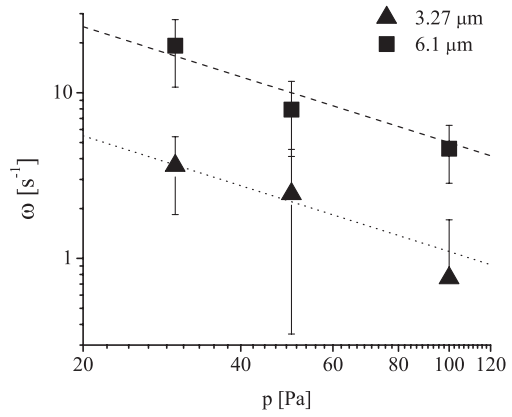


FIG. 7. Angular velocity (vorticity) of the rotating particles versus gas pressure The dashed line $\omega[\mathrm{s}^{-1}] = 500(p[\mathrm{Pa}])^{-1}$ and the dotted line $\omega[\mathrm{s}^{-1}] = 110(p[\mathrm{Pa}])^{-1}$ indicate a dependence proportional to $p^{-1}$ of the cloud vorticity.

In conclusion, we observed steady-state particle clouds levitating in a vertical glass tube, above a heated wire. The particles exhibited a global convective flow. We showed that the particle vortices were induced by the convection of neutral gas, analogously to convective clouds in the atmosphere. The mechanism responsible for the gas convection was the thermal creep along the inhomogeneously heated tube walls. The phenomenon of thermal creep, which commonly occurs in rarefied gases under the presence of thermal gradients, has never been taken into account in experiments with complex plasmas. We believe that this phenomenon should generally play a substantial role in the experiments, because (i) the resulting convection can be triggered in the absence of gravity, (ii) it operates in the pressure range typical for complex plasmas, and (iii) it does not require substantial temperature gradients and hence might be triggered due to natural temperature inhomogeneities always present in experiments.

The authors acknowledge valuable discussions with Uwe Konopka. This work was supported by DLR under Grant No. 50 WM 0504.

[1] V. E. Fortov *et al.*, Phys. Rep. **421**, 1 (2005).
[2] O. S. Vaulina *et al.*, JETP **91**, 1147 (2000).
[3] P. K. Shukla, Phys. Lett. A **268**, 100 (2000).
[4] V. N. Tsytovich *et al.*, Phys. Plasmas **13**, 032306 (2006).
[5] S. N. Antipov *et al.*, in *Proceedings of the 33rd EPS Conference on Plasma Physics* (European Physical Society, Frascati, Italy, 2006), Vol. 30I, p. D-5.027.
[6] M. Rubin-Zuzic *et al.*, New J. Phys. **9**, 39 (2007).
[7] V. Fortov *et al.*, JETP **96**, 704 (2003).
[8] O. Vaulina *et al.*, New J. Phys. **5**, 82 (2003).
[9] G. Morfill *et al.*, Phys. Rev. Lett. **83**, 1598 (1999).
[10] A. Samarian *et al.*, Phys. Scr. **T98**, 123 (2001).
[11] O. S. Vaulina *et al.*, Plasma Phys. Rep. **30**, 988 (2004).
[12] A. V. Ivlev *et al.*, Phys. Rev. Lett. **99**, 135004 (2007).
[13] V. Fortov *et al.*, Plasma Phys. Controlled Fusion **47**, B537 (2005).
[14] S. A. Khrapak *et al.*, Phys. Rev. E **72**, 016406 (2005).
[15] J. Tyndall, Proc. R. Inst. G.B. **6**, 3 (1870); W. Cawood, Trans. Faraday Soc. **32**, 1068 (1936); L. Waldmann, Z. Naturforsch. A **14**, 589 (1959).
[16] H. Rothermel *et al.*, Phys. Rev. Lett. **89**, 175001 (2002).
[17] A. V. Ivlev *et al.*, Plasma Phys. Controlled Fusion **46**, B267 (2004).
[18] P. Epstein, Phys. Rev. **23**, 710 (1924).
[19] Y. P. Raizer, *Gas Discharge Dynamics* (Springer-Verlag, Berlin, 1991).
[20] M. N. Kogan, *Rarefied Gas Dynamics* (Plenum, New York, 1969).
[21] S. P. Bakanov, Usp. Fiz. Nauk **162**, 133 (1992).
[22] E. M. Lifshitz and L. P. Pitaevskii, *Kinetic Theory of Gases* (Pergamon, Oxford, 1981).
[23] J. C. Maxwell, Philos. Trans. R. Soc. London **170**, 231 (1879).
[24] O. Reynolds, Philos. Trans. R. Soc. London **170**, 727 (1879).

New Journal of Physics
The open-access journal for physics

# Spectroscopic evaluation of the effect of the microparticles on radiofrequency argon plasma

**S Mitic**[1], **M Y Pustylnik and G E Morfill**

Max-Planck-Institut für Extraterrestrische Physik, Giessenbachstraße 1, 85741 Garching, Germany
E-mail: mitic@mpe.mpg.de

*New Journal of Physics* **11** (2009) 083020 (16pp)
Received 4 May 2009
Published 19 August 2009
Online at http://www.njp.org/
doi:10.1088/1367-2630/11/8/083020

**Abstract.** Axial distributions of 1s excited states of argon were measured in a radiofrequency (RF) discharge by a self-absorption method. Experiments were performed in the PK-3+ chamber, designed for microgravity experiments in complex (dusty) plasmas on board the International Space Station. A correction of a standard self-absorption method for the extinction of the light by the levitating microparticles is proposed. Distributions, measured at the same discharge conditions in a microparticle-free discharge and a discharge containing a cloud of levitating microparticles, revealed the non-local influence of the microparticle cloud on the discharge plasma. The most probable cause of this influence is the disturbance of the ionization balance by the levitating microparticles.

[1] Author to whom any correspondence should be addressed.

## Contents



## 1. Introduction

Complex (dusty) plasmas are of great interest for technological applications as well as from the point of view of basic physics. Many industrial processes suffer from the presence of microparticles in the volume of discharges [1] and in many of them the presence of microparticles is desirable [2]. For fundamental science complex plasmas represent unique models of strongly coupled systems, available for observation at a kinetic level [2, 3]. For both fields, the influence of microparticles on the plasma is of significant importance. It has been known for a long time that the losses of plasma particles on the surface of the microparticles suspended in a plasma, may be comparable to that on the walls of the setup, resulting in e.g. faster decay of the plasmas [4]. Later, in the 1990s the influence of nanometer-sized particles on capacitively coupled radiofrequency (RF) discharges was extensively studied. The main results of these studies can be summarized as follows: the presence of nanometer-sized particles with a density of the order of $10^{14}\,\mathrm{m}^{-3}$ in a plasma leads to a strong shift of the ionization balance in the discharge. This shift reveals itself in changes of practically all the plasma properties: current–voltage characteristics and RF-matching parameters [5, 6], increase of integral intensity of the radiation as well as the number density of metastables [5, 7], dramatic decrease of the electron density and increase of temperature [5, 6]. This transformation was given the name '$\alpha$–$\gamma$'' [5, 8, 9] transition in analogy with the $\alpha$–$\gamma$ transition previously known for capacitively coupled RF discharges [10]. Recently, such tiny effects as the modification of the $H_\alpha$ line shape in the presence of nanometer-sized particles have been revealed [11].

For nanometer-sized particles, the gravitational force is negligibly small. Therefore, if injected into or grown in the discharge, these particles will occupy the entire plasma volume. It is not surprising then that their influence on the discharge has a global character. A very local effect of microparticles on the plasma has been recently demonstrated by Do *et al* [12]. They levitated a very thin (2–3 mm vertical extension) cloud of monodisperse silica microspheres of 10 $\mu$m diameter and measured the axial and radial profiles of the number density of metastable

states using laser absorption spectroscopy. The microparticle-induced changes were very local. The density of metastables decreased (in contrast to the increase in the case of experiments with nanometer-sized particles) only inside the microparticle cloud. This decrease was attributed to the loss of metastables on the surface of the suspended microparticles.

In this work, we concentrate on the evaluation of the effect of micropaticles on the plasma in the PK-3+ chamber, which is the heart of the International Space Station-based complex plasma laboratory [13]. In several microgravity and ground-based experiments in PK-3+ [13] and its predecessor PK-3 Nefedov [14, 15], changes of the plasma glow distribution, caused by the motion of microparticles (e.g. injection of microparticles, heartbeat instability, etc), were observed. This suggests the necessity for the evaluation of the effect of microparticles on the plasma in this device. We use a single-mirror self-absorption method [16, 17] to measure the absolute values of the number densities of metastable and resonant states of argon in the presence of microparticles as well as in the absence of microparticles in the discharge. We try to draw conclusions about the physical mechanisms underlying the observed microparticle-induced changes.

## 2. Experimental method

### *2.1. Experimental setup*

The PK-3+ setup is, briefly, a symmetrically driven parallel plate 13.56 MHz RF discharge with disc-shaped electrodes 6 cm in diameter and 3 cm gap. Experiments were carried out at working pressures of 15, 30 and 60 Pa with argon buffer gas. RF voltage of about 20 V peak-to-peak was applied to the electrodes. RF power of 0.2 W was kept constant in all the experiments. Electron temperature and density lie in the range of 3–7 eV and $10^{14}$–$10^{15}$ $m^{-3}$ [18, 19].

Light from the discharge was collected by an optical fiber with a collimator attached to it. The collimator provided the horizontal line of sight of approximately 2 mm thickness. A Hamamatsu Mini-spectrometer TM-series with 3 nm resolution was used to obtain the spectrum. The optical fiber could be moved vertically by a translation stage in order to obtain the vertical profile of light emission (figure 1). Spectra were recorded with a 3 mm step.

For the measurements of self-absorption a protected-Al mirror, opposing the fiber, was used. For each position of the fiber and for each discharge condition, spectra with and without the mirror were recorded. Also the measurements were repeated twice at the same argon pressure for the microparticle-free plasma and the plasma with a large cloud of microparticles, levitating in it.

As microparticles we used monodisperse plastic (melamineformaldehyde) microspheres of 2.55 $\mu$m diameter. To observe them levitating in a plasma we illuminated them with a vertical laser sheet and observed the scattered light with a video camera (figure 1). The number density of the microparticles was always of the order of $10^{11}$ $m^{-3}$. The same videocamera could be used for imaging of the integral glow of the discharge.

In the PK-3+ setup, the refreshment of gas is performed in pulses. During all measurements the time interval between two pulses was set to 40 s. This periodical gas refreshment resulted in a slight periodic change of discharge parameters. This fact was reflected in the periodical behavior of the intensities of the spectral lines. Therefore, the spectral measurements were synchronized with the gas injection and were performed 20 s after it.

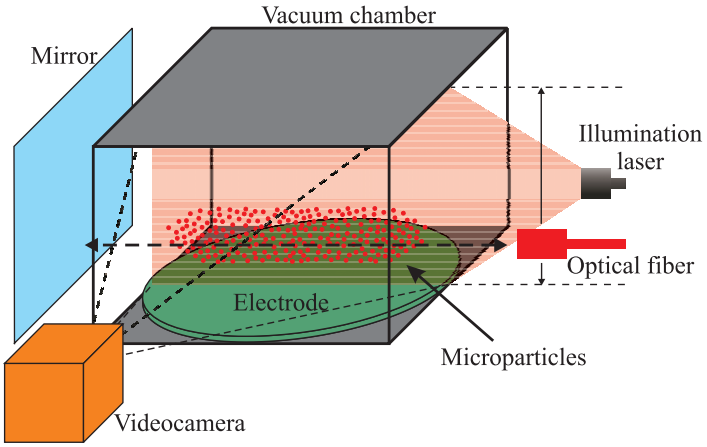


**Figure 1.** Scheme of the experimental setup. A discharge is generated by applying RF voltage to the electrodes. Under the laboratory conditions microparticles levitate closer to the bottom electrode due to gravity. They are illuminated with a vertical laser sheet and observed by a video camera. An optic fiber is used to collect the light from the discharge. A mirror, placed opposite to the fiber, allows the evaluation of self-absorption.

### *2.2. Determination of the number density of the argon states*

The populations of the argon levels are determined using a well-known single mirror self-absorption method [16, 17]. Discharge radiation, reflected by the mirror, is used to probe the plasma. Measurements of the intensities of the spectral lines for the transition $i \rightarrow j$ with and without the mirror allow us to determine the relative absorption $A_{ij}^{\mathrm{L}}$:

$$A_{ij}^{\mathrm{L}} = \frac{1 + r_{ij} - I_{ij}^{\mathrm{m}}/I_{ij}^{\mathrm{n}}}{r_{ij}}, \tag{1}$$

where $r_{ij}$ is the reflectance of the mirror at the wavelength $\lambda_{ij}$ of the considered transition, $I_{ij}^{\mathrm{m}}$ and $I_{ij}^{\mathrm{n}}$ are the line intensities with and without the mirror, respectively. We assume that our plasma is uniform along the (radially directed) line of sight, i.e. the top and bottom states of each radiative transition as well as the microparticles are distributed uniformly. At the same time, we consider axial distributions of the parameters to be important. In this approximation, the intensity of a spectral line registered by a detector, observing a certain line of sight, may be expressed as follows [16]:

$$I_{ij} = \int_{-\infty}^{\infty} \frac{I_{ij}^{1}(\nu)}{\kappa_{ij}(\nu)} \left(1 - \mathrm{e}^{-\tau_{ij}(\nu)}\right) \mathrm{d}\nu, \tag{2}$$

where $\nu$ is the frequency detuning from the center of a spectral line, $I_{ij}^{1}(\nu)$ is the intensity profile, emitted by the unit of length of the plasma, $\kappa_{ij}(\nu)$ is the absorption profile, so that the optical thickness of the plasma $\tau_{ij}(\nu) = \kappa_{ij}(\nu) \times l$ ($l$ is the length of the plasma along the line of sight). The mirror effectively serves as a light source with the intensity $I_{ij}^{\mathrm{s}} = r_{ij} I_{ij}$, of which the intensity

$$I_{ij}^{\mathrm{t}} = r_{ij} \int_{-\infty}^{\infty} \frac{I_{ij}^{1}(\nu)}{\kappa_{ij}(\nu)} \mathrm{e}^{-\tau_{ij}(\nu)} \left(1 - \mathrm{e}^{-\tau_{ij}(\nu)}\right) \mathrm{d}\nu \tag{3}$$

will be transmitted through the plasma to the detector side. The relative absorption is then $A_{ij}^{\mathrm{L}} = (I_{ij}^{\mathrm{s}} - I_{ij}^{\mathrm{t}})/I_{ij}^{\mathrm{s}}$. Substituting equations (2) and (3) into the expression for $A_{ij}^{\mathrm{L}}$ after some algebra yields

$$A_{ij}^{\mathrm{L}} = 2 - \frac{\int_{-\infty}^{\infty} \frac{I_{ij}^{\mathrm{l}}(\nu)}{\kappa_{ij}(\nu)} \left(1 - \mathrm{e}^{-2\tau_{ij}(\nu)}\right) \mathrm{d}\nu}{\int_{-\infty}^{\infty} \frac{I_{ij}^{\mathrm{l}}(\nu)}{\kappa_{ij}(\nu)} \left(1 - \mathrm{e}^{-\tau_{ij}(\nu)}\right) \mathrm{d}\nu}. \tag{4}$$

In microparticle-free plasmas, the only mechanism contributing to $A_{ij}^{\mathrm{L}}$ is the absorption of the radiation by the bottom states of respective transitions, i.e. self-absorption. In addition to that, in complex plasmas microparticles will also effectively contribute to the absorption due to extinction. Therefore total absorption coefficient and optical thickness may be rewritten as a sum of plasma and microparticle components: $\kappa_{ij}(\nu) = \kappa_{ij}^{\mathrm{d}} + \kappa_{ij}^{\mathrm{pl}}(\nu)$ and $\tau_{ij}(\nu) = \tau_{ij}^{\mathrm{d}} + \tau_{ij}^{\mathrm{pl}}(\nu)$. The microparticle contribution may be considered to be independent of the frequency within a typical width of a spectral line since the variation of the Mie-scattering and absorption cross-sections as well as the refractive index of the microparticle material is negligible in such a narrow spectral band. Equation (4) may therefore be rewritten in the following way:

$$A_{ij}^{\mathrm{L}} = 2 - \frac{\int_{-\infty}^{\infty} \frac{I_{ij}^{\mathrm{l}}(\nu)}{\tau_{ij}^{\mathrm{pl}}(\nu) + \ln(K_{ij}^{\mathrm{d}})} \left(1 - \frac{\mathrm{e}^{-2\tau_{ij}^{\mathrm{pl}}(\nu)}}{\left(K_{ij}^{\mathrm{d}}\right)^2}\right) \mathrm{d}\nu}{\int_{-\infty}^{\infty} \frac{I_{ij}^{\mathrm{l}}(\nu)}{\tau_{ij}^{\mathrm{pl}}(\nu) + \ln(K_{ij}^{\mathrm{d}})} \left(1 - \frac{\mathrm{e}^{-\tau_{ij}^{\mathrm{pl}}(\nu)}}{K_{ij}^{\mathrm{d}}}\right) \mathrm{d}\nu}. \tag{5}$$

Here $1/K_{ij}^{\mathrm{d}} = \exp(-\tau_{ij}^{\mathrm{d}})$, i.e. $K_{ij}^{\mathrm{d}}$ is the attenuation of a spectral line by the microparticles levitating in a plasma.

Profiles $\kappa_{ij}^{\mathrm{pl}}(\nu)$ and $I_{ij}^{\mathrm{l}}(\nu)$ are determined by the broadening mechanism of a spectral line. Estimations, using the experimental data on the broadening of Ar lines [20, 21], show that under our conditions collisional broadening is negligible and consequently a pure Doppler profile can be used: $\kappa_{ij}^{\mathrm{pl}}(\nu)$, $\tau_{ij}^{\mathrm{pl}}(\nu)$, $I_{ij}^{\mathrm{l}}(\nu) \propto \exp\left(-\lambda_{ij}^2 \frac{M}{2k_{\mathrm{B}}T}\nu^2\right)$, where $M$ is the argon atom mass and $T$ is the temperature of the neutral gas. This allows us to bind the relative absorption with the optical thickness in the center of the line $\tau_{ij}^{\mathrm{pl}}(0)$:

$$A_{ij}^{\mathrm{L}} = 2 - \frac{\int_{-\infty}^{\infty} \frac{\mathrm{e}^{-\omega^2}}{\tau_{ij}^{\mathrm{pl}}(0)\mathrm{e}^{-\omega^2} + \ln(K_{ij}^{\mathrm{d}})} \left(1 - \frac{\exp\left(-2\tau_{ij}^{\mathrm{pl}}(0)\mathrm{e}^{-\omega^2}\right)}{\left(K_{ij}^{\mathrm{d}}\right)^2}\right) \mathrm{d}\omega}{\int_{-\infty}^{\infty} \frac{\mathrm{e}^{-\omega^2}}{\tau_{ij}^{\mathrm{pl}}(0)\mathrm{e}^{-\omega^2} + \ln(K_{ij}^{\mathrm{d}})} \left(1 - \frac{\exp\left(-\tau_{ij}^{\mathrm{pl}}(0)\mathrm{e}^{-\omega^2}\right)}{K_{ij}^{\mathrm{d}}}\right) \mathrm{d}\omega}, \tag{6}$$

where $\omega = \lambda_{ij}\sqrt{\frac{M}{2k_{\mathrm{B}}T}}\nu$ is a dimensionless integration variable. In the absence of microparticles ($K_{ij}^{\mathrm{d}} = 1$) expression (6) is reduced to a well-known equation for a single mirror method [17]. On the other hand, if self-absorption is switched to zero ($\tau_{ij}^{\mathrm{pl}}(0) = 0$), equation (6) reduces to $A_{ij}^{\mathrm{L}} = 1 - (K_{ij}^{\mathrm{d}})^{-1}$, which represents the relative absorption of a monochromatic wave [16]. The latter is expected, since we neglected the detuning dependence of $K_{ij}^{\mathrm{d}}$. The stronger the

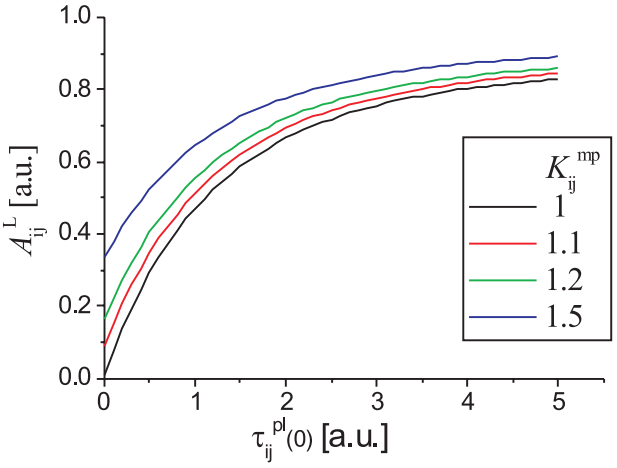


**Figure 2.** Dependence of the relative absorption $A_{ij}^{\mathrm{L}}$ on the optical thickness in the center of a spectral line $\tau_{ij}^{\mathrm{pl}}(0)$ at different attenuations by microparticles $K_{ij}^{\mathrm{d}}$. The higher $K_{ij}^{\mathrm{d}}$ is, the smaller $\tau_{ij}^{\mathrm{pl}}(0)$ is required to provide the same total relative absorption. The contribution of microparticles to the total absorption is especially significant at small $\tau_{ij}^{\mathrm{pl}}(0)$.

attenuation by the macroparticles, the smaller the optical thickness $\tau_{ij}^{\mathrm{pl}}(0)$ will be at a given relative absorption $A_{ij}^{\mathrm{L}}$ (figure 2).

All the quantities in the rhs of (1) can be experimentally measured. Therefore $\tau_{ij}^{\mathrm{pl}}(0)$ can be determined from (6), provided the respective microparticle-caused attenuation $K_{ij}^{\mathrm{d}}$ is known. Supposing the Doppler broadening of the line, $\tau_{ij}^{\mathrm{pl}}(0)$ is connected with the number density of the bottom state of the transition [22]:

$$\tau_{ij}^{\mathrm{pl}}(0) = \frac{\lambda_{ij}^{3}}{8\pi}\sqrt{\frac{M}{2k_{\mathrm{b}}T}}\frac{g_i}{g_j}A_{ij}n_j l, \tag{7}$$

where $g_i$ and $g_j$ are the statistical weights of the top and bottom states of the transition, respectively, $A_{ij}$ is the Einstein coefficient and $n_j$ is the number density of a bottom state.

Using the experimental method described above and solving equations (1), (6) and (7) for the following spectral lines of argon: 706.7, 794.8, 738.3 nm and 826.4 nm, we could determine the populations of the $1s_5$, $1s_3$, $1s_4$ and $1s_2$ levels, respectively.

### *2.3. Estimation of the microparticle-caused attenuation*

To correctly determine the number density of argon states in complex plasmas, we need to take into account the extinction of the plasma radiation by the microparticles levitating in it. It is, however, difficult to estimate the extinction cross-section numerically due to the lack of data on the refractive index of melamineformaldehyde in the spectral range of interest. Clean *in situ* measurement is also a problem due to the difficulty in distinguishing between the extinction and self-absorption.

We estimated the extinction experimentally. To perform this, we ignited a *neon* discharge in the same PK-3+ chamber and levitated in it clouds of the same microparticles, with the number

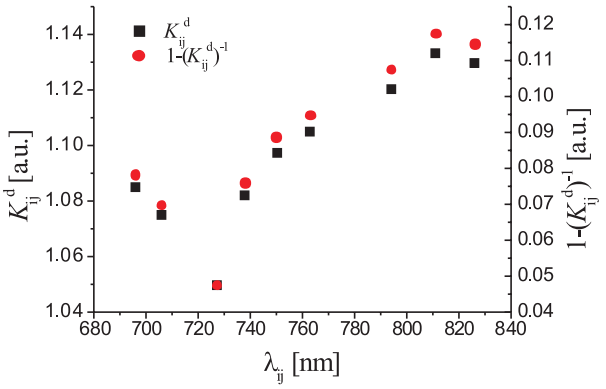


**Figure 3.** Measured spectral dependence of the attenuation $K_{ij}^{\mathrm{d}}$ and relative absorbtion $1-(K_{ij}^{\mathrm{d}})^{-1}$ of light by a cloud of microparticles. In the spectral range of interest, the relative absorbtion varies by more than a factor of two. The highest value of $K_{ij}^{\mathrm{d}}$ obtained in our experiments is $\approx 1.13$.

densities and axial extensions close to those that we observed in the main experiment. We used an argon lamp to evaluate the attenuation of its light by the cloud of microparticles. In this case, self-absorption does not take place. Therefore we may assign $K_{ij}^{\mathrm{d}}$ the attenuations measured in this way. Typical values of $K_{ij}^{\mathrm{d}}$ for our dust clouds (microparticle density of $\sim 10^{11}\,\mathrm{m}^{-3}$) are given in figure 3.

## 3. Results

### *3.1. Microparticle-free plasma*

Here we present the results of the measurements in the microparticle-free plasma. Since the discharge is strongly non-uniform along its axis $z$, for the correct comparison of different regimes we always consider axial distributions of the quantities of interest. The point $z = 0$ corresponds to the bottom electrode. In all the experiments, measured line intensities followed the classical glow distribution in the so-called $\alpha$-form of a RF discharge [10]: they had humps close to the powered electrodes and a dip in the center. Examples of these distributions for the argon pressure of 15 Pa are shown in figure 4. Optical thicknesses and number densities exhibit similar behavior. Maximal values of optical thicknesses are of the order of unity and are therefore not negligible, allowing for the determination of the line-of-sight integrated number densities $n_j \times l$. Remarkable is the hierarchy of number densities of different levels, also independent of pressure: the $1s_3$ level has the smallest number density, significantly larger and very close to each other are those of two radiative levels and $1s_5$ exhibits the largest population. The same hierarchy was obtained in a GEC reference cell by the so-called 'robust method' [22] at argon pressures higher than 1 Pa.

Axial distributions of $n_j$ are pressure dependent. All the levels behave similarly with pressure. An example for a metastable level $1s_5$ and radiative level $1s_2$ is given in figure 5. In the humps, the number densities are considerably larger for 60 Pa than for 15 and 30 Pa. In the central area, the tendency is opposite: at 15 Pa the number densities are increased with respect to those at 30 and 60 Pa. The pressure dependence of the number densities is summarized in

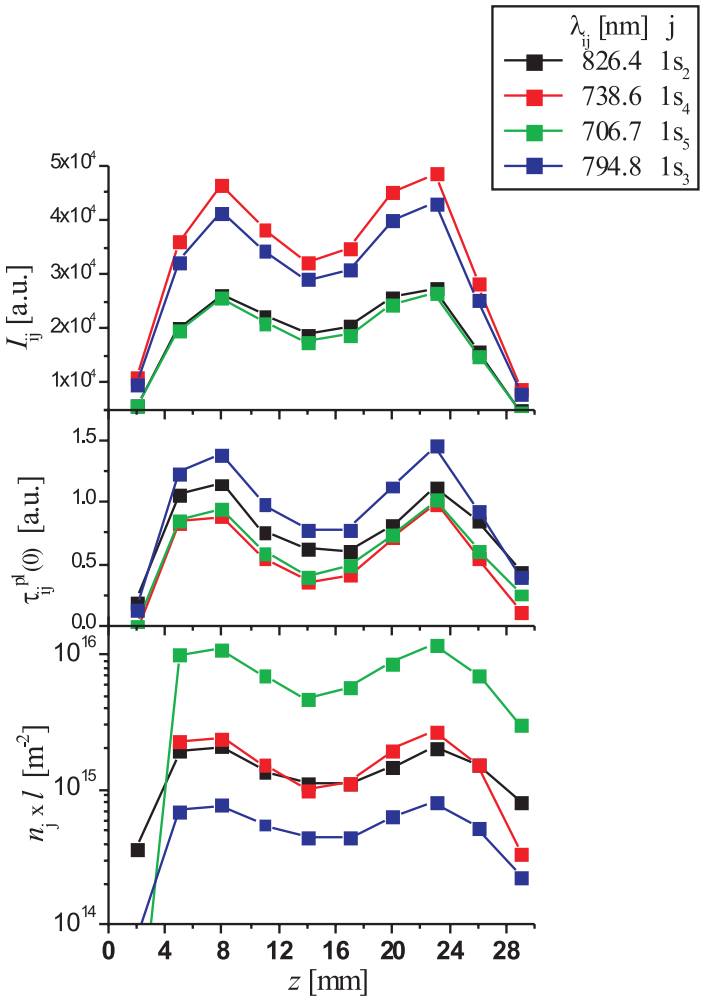


**Figure 4.** Axial distributions of intensities and optical thicknesses for the considered spectral lines and line-of-sight-integrated densities of the respective bottom levels at an argon pressure of 15 Pa in a microparticle-free discharge. All three quantities exhibit similar behavior with humps close to the electrodes and a dip in the center.

table 1: absolute maximal values and minimal values in between the humps at different pressures are given.

### *3.2. Effect of a microparticle cloud*

The effect of the levitating cloud of microparticles on the plasma can be seen from the simple imaging of the discharge glow. Figure 6(a) represents the image of a microparticle-free discharge. The glow in this case is symmetric with respect to the middle plane of the discharge. Injection of microparticles leads to the evident break of this symmetry. Due to gravity microparticles concentrate themselves in the glow region above the bottom electrode (figure 7(a)) and as a result the shape of this glow region is significantly modified—it is broadened and extends significantly deeper into the central, relatively dark area of the discharge

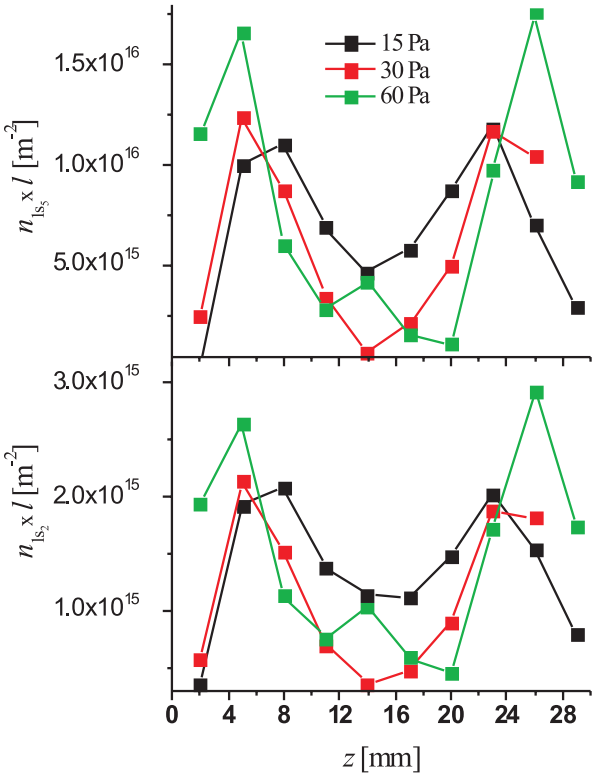


**Figure 5.** Pressure dependence of the axial profiles of the number densities for $1s_2$ and $1s_5$ states of argon. Humps of the distributions grow on the increase of pressure, whereas the dip, on the contrary, considerably drops as the pressure is increased. Similar dependence on pressure is observed for all four considered levels.

**Table 1.** Line-of-sight integrated number densities of metastable and radiative states of argon in the PK-3+ chamber at humps and dips of the axial distribution for different pressures. The values are given in $10^{15}$ m$^{-2}$. RF power is 0.2 W.

| | Hump | | | | Dip | | | |
|---|---|---|---|---|---|---|---|---|
| Pressure (Pa)/levels | $1s_5$ | $1s_3$ | $1s_2$ | $1s_4$ | $1s_5$ | $1s_3$ | $1s_2$ | $1s_4$ |
| 15 | 11.1 | 0.78 | 2.4 | 2.1 | 4.7 | 0.50 | 1.1 | 0.99 |
| 30 | 12.5 | 0.98 | 3.0 | 2.1 | 0.67 | 0.23 | 0.36 | 0.08 |
| 60 | 16.6 | 1.1 | 3.7 | 2.7 | 1.1 | 0.19 | 0.45 | 0.09 |

(figure 6(b)). The upper glow region appears to be influenced much more weakly. The axial profiles of the intensities of the spectral lines support the effect observed with the imaging (figure 6(c)). In addition, they exhibit a slight increase of the intensity in the upper glow region. The maxima of intensity profiles in the bottom glow region shift several mm toward the center of the discharge in the presence of a microparticle cloud. Therefore, it is clear that a cloud of microparticles levitating in our plasma produces significant non-local influence on the discharge.

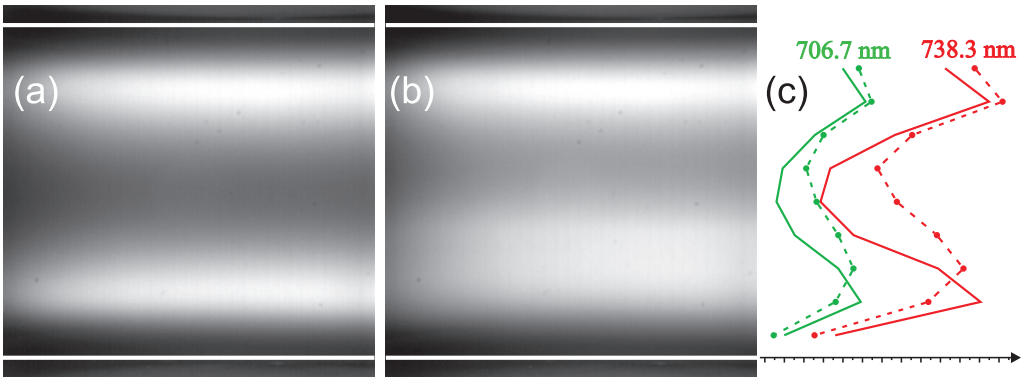


**Figure 6.** Images of the plasma glow at 30 Pa (white horizontal lines represent the electrodes): (a) microparticle-free discharge, (b) discharge with a cloud of microparticles. (c) Axial profile of the intensities of the spectral lines. Solid curve corresponds to the microparticle-free plasma and dashed curve to the plasma with a cloud of microparticles. The main effect of the microparticles on the glow is the extension of the bottom glow region into the central area of the discharge.

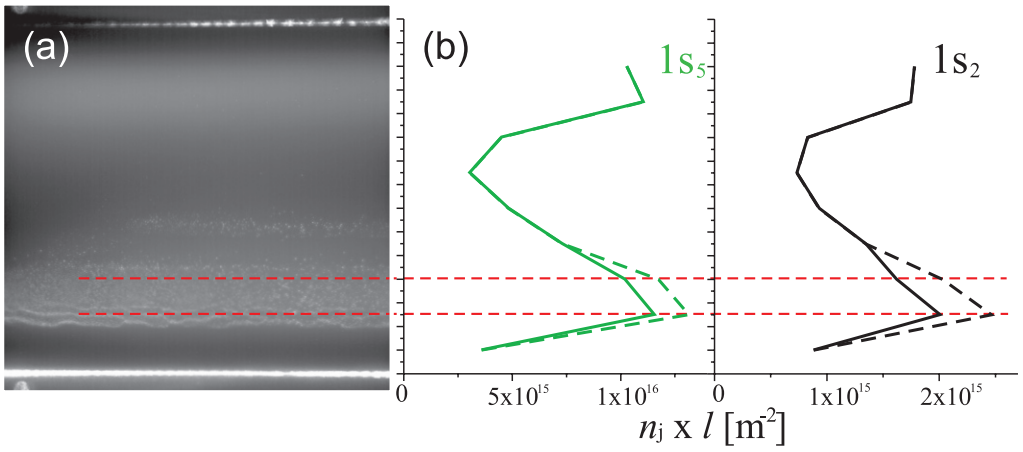


**Figure 7.** (a) Typical image of a discharge with a cloud of microparticles levitating in it (30 Pa). The cloud consists of a main thick cloud and a much smaller cloud, levitating above the main one. Attenuation $K_{ij}^{\mathrm{d}}$ is taken into account only for the main cloud. (b) Comparison of the number densities of $1s_2$ and $1s_5$ states, determined with measured $K_{ij}^{\mathrm{d}}$ (solid curve) and $K_{ij}^{\mathrm{d}} = 1$ (dashed curve). Not accounting for the extinction of the plasma light by microparticles may lead to up to 25% overestimation of the number densities of states.

According to our method, for the number densities of the argon states to be determined in the presence of a microparticle cloud, attenuation $K_{ij}^{\mathrm{d}}$ (figure 3) must be taken into account. There are two issues that alter the exact relevance of values of $K_{ij}^{\mathrm{d}}$ estimated in section 2.3 to the actual values of the extinction in the self-absorption experiments. Firstly, Mie-scattering measurements are sensitive to geometrical factors like, e.g. view angle of the detector or angular composition of the incident light [23]. In a very simple estimation of $K_{ij}^{\mathrm{d}}$ we were not able to

reproduce the geometry of the light source: for the self-absorption measurements we used a large mirror, which covered almost the entire rectangular viewport (80 mm height and 95 mm width), whereas to estimate $K_{ij}^{\mathrm{d}}$ we employed a cylindrically shaped Ar lamp, which was oriented vertically and covered the entire height of the viewport, but was only 6 mm thick in the horizontal direction. Secondly, as already mentioned, $K_{ij}^{\mathrm{d}}$ was estimated for a structure of microparticles different from (but nevertheless similar to) the one used in the self-absorption experiment. We, therefore, cannot depend on the high precision of the extinction correction of the number density of the states. In spite of this, we would like to demonstrate the importance of accounting for the microparticle-caused light attenuation.

We should also note that $K_{ij}^{\mathrm{d}}$ should certainly be different at different heights. In our consideration, we skip the axial dependence and simply use the values of $K_{ij}^{\mathrm{d}}$ from figure 3 for every point inside the 'main' microparticle cloud. We do not account for the microparticle-caused attenuation in a small cloud, located slightly above the main one, due to its smaller radial extension. We checked that for such small clouds attenuation appears to be undetectable. In figure 7(b), the results of the determination of $n_j$ with measured $K_{ij}^{\mathrm{d}}$ and $K_{ij}^{\mathrm{d}} = 1$ are compared. Neglecting the microparticle-caused attenuation under our conditions may lead to up to 25% overestimation of the number densities. This overestimation may be even larger in the experiments, where the structures of microparticles are denser and/or more extensive, e.g. under microgravity conditions [13] or when thermophoresis is used to compensate for gravity [24].

The axial distribution of the number density of states undergoes practically the same changes as the distribution of line intensities does in the presence of microparticles. The bottom hump of the distribution is stretched toward the midplane of the discharge (figure 8). Therefore, the strongest relative changes (double and more with respect to the microparticle-free plasma) are in the center of the discharge. This effect is much less pronounced at 15 Pa than at 30 and 60 Pa (figure 9). The upper hump remains practically unaffected by the presence of microparticles.

## 4. Discussion

### *4.1. Ionization balance*

As already mentioned, microparticles suspended in a plasma volume may constitute a significant bulk loss of plasma particles. Let us try to estimate this loss for the conditions of our experiment. For this we have to compare the loss of the electrons on the microparticles with their production rate in a microparticle-free plasma. The axial distribution of electron temperature in $\alpha$ RF discharges is significantly non-uniform [10]. It determines the observed two-humped distribution of brightness. The distribution of ionization should also reproduce this structure. The microparticle cloud in our experiment roughly occupies the volume, corresponding to one of these maxima. The second maximum is practically not affected by the presence of microparticles. This suggests the diffusive interchange between the two maxima is weak, allowing therefore to treat the ionization balance in them independently from each other.

We consider here three mechanisms of ionization: electron impact on metastable argon atom ($1s_5$), metastable pooling and electron impact on ground state argon atoms. We use the expressions for constants of these processes from [25] to calculate the respective rates for electron temperatures $T_{\mathrm{e}} = 1$–$7$ eV and electron densities $n_{\mathrm{e}} = 10^{14}$–$10^{15}\,\mathrm{m}^{-3}$. Line-of-sight averaged densities from table 1 with $l$ equal to the electrode diameter (0.06 m) were used to

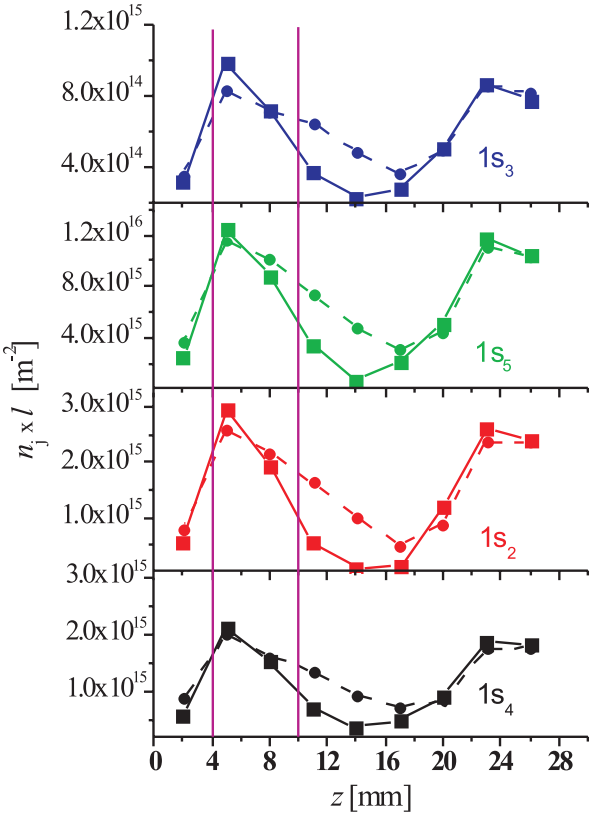


**Figure 8.** Effect of the microparticle cloud on number densities of different argon states at 30 Pa. Solid curves correspond to the plasma without the microparticles, dashed curves—to the plasma with a dust cloud levitating inside it. The central area of the discharge experiences the strongest influence of the microparticle cloud. Magenta vertical lines represent the upper and lower boundaries of the main microparticle cloud.

obtain the number densities of metastables. Electron impact ionization from the ground state dominated at $T_e \gtrsim 2$ eV.

The loss of electrons on the microparticles is an essential function of their surface potential, which is in turn self-consistently connected to the conditions in the background plasma. We cannot calculate the electron loss self-consistently. Instead, we estimate the electron flux on microparticles with a certain fixed potential, immersed into a microparticle-free plasma, and compare it with the respective ionization rate.

The absolute value of the potential may lie between zero and the potential of an isolated particle, given, e.g. by orbital-motion-limited (OML) theory [27]. The OML electron flux is given by the following equation:

$$j_e(\phi) = \pi a^2 n_e \sqrt{\frac{8}{\pi}\frac{T_e}{m}}\, \exp\left(\frac{\phi}{T_e}\right), \tag{8}$$

where $a$ is the radius of a spherical microparticle, $m$ is the electron mass and $\phi$ is the surface potential of a microparticle. We will consider the fluxes in the range $j_e(0) > j_e > j_e(\phi_{is})$, where $\phi_{is}$ is the surface potential of an isolated microparticle: $\sqrt{T_e/m}\exp(\phi_{is}/T_e) = \sqrt{T/M}(1-\phi_{is}/T)$.

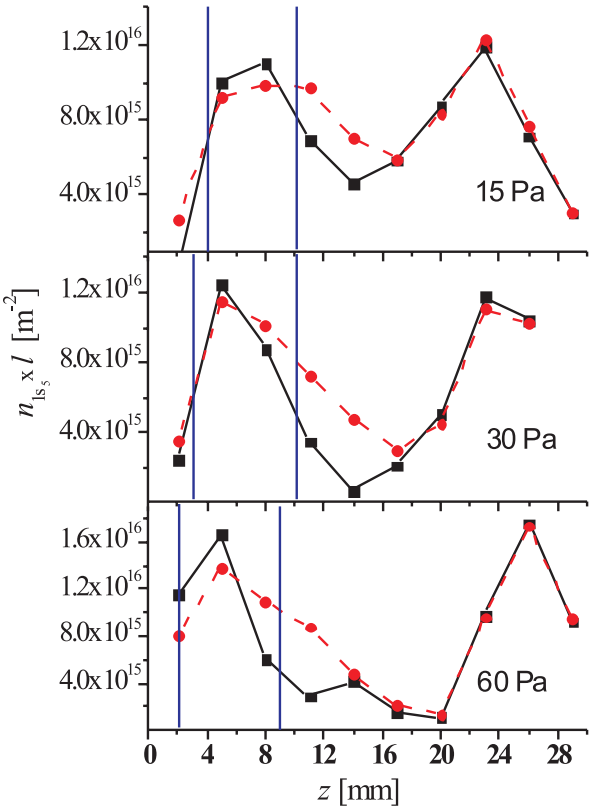


**Figure 9.** Pressure dependence of the effect of the cloud of microparticles on the number density of $1s_5$ level. Blue vertical lines represent the upper and lower boundaries of the main microparticle cloud. The effect of the presence of microparticles on the number densities of other states has a similar pressure dependence.

The bulk loss of electrons is then $n_d j_e(\phi)$, where $n_d$ is the density of microparticles, estimated for all the experiments to be of the order of $10^{11}$ m$^{-3}$.

On a map in figure 10, the $(T_e, n_e)$ plane is divided into three regions (30 Pa)—where ionization rate exceeds both losses $n_d j(\phi_{is})$ and $n_d j(0)$, where it lies in between them and where it is below both of them. The map looks qualitatively similar for other pressures. Being deep in the red region would mean that the presence of the microparticle cloud would not significantly affect the ionization balance. In the blue region, the plasma cannot be sustained due to the loss of electrons on suspended microparticles. The green region represents the transient situation. A possible situation in the green region is e.g. the following: the loss of electrons on microparticles is significant during their charging, but becomes much less significant after they are charged to equilibrium.

This treatment does not take into account depletion of electrons in the presence of microparticles, often associated with the so-called Havnes parameter [26]. This depletion would make sustainment of the plasma at a given $T_e$ even more difficult.

As follows from figure 10, in the reasonable range of $n_e$ and $T_e$ for our plasma we can expect a strong effect of the microparticles on the ionization balance. The transformation that our plasma undergoes may be qualitatively understood in the following way. The line intensities

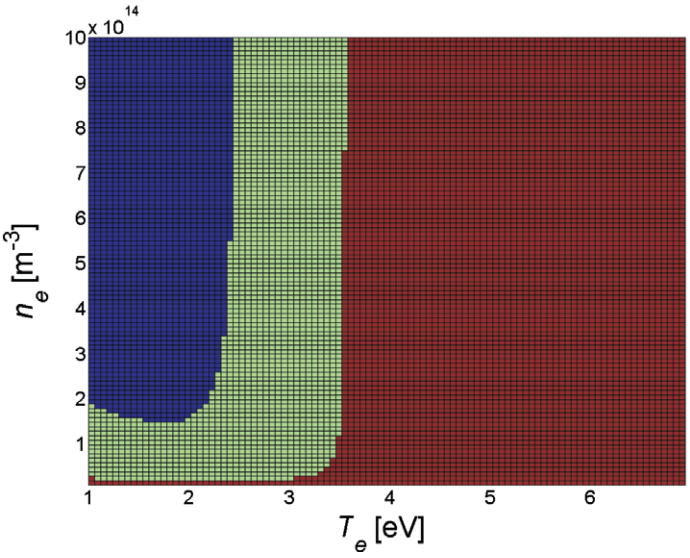


**Figure 10.** Color map presenting the qualitative comparison of ionization rate and loss of electrons on the microparticles for 30 Pa. In the red area, the ionization rate exceeds both $n_d j_e(0)$ and $n_d j_e(\phi_{is})$, in the green area it is in between them and in the blue area loss on microparticles dominates over the ionization. In the reasonable range of parameters the region with a significant impact of microparticles on the ionization balance is found.

we observe are strong functions of the electron temperature. Since injection of microparticles does not at least increase the amplitude of the discharge brightness, the amplitude of the electron temperature does not seem to increase. Instead, the region with high $T_e$ is spread quite far outside the main microparticle cloud so that diffusive influx of electrons into the cloud could compensate for the loss of electrons on the microparticles. This transformation, however, requires further experimental and theoretical investigations to reveal the mechanisms underlying it.

### *4.2. Metastables*

Lifetimes of argon metastable states significantly exceed their typical diffusion times in plasmas. Therefore, metastable atoms can reach the surface of a microparticle levitating in a plasma and be quenched on it well before they decay. This aspect of metastable–microparticle interactions has been studied in detail in [12], where a very local effect of microparticles on the density of $1s_3$ neon metastables was observed: the density decreased only within the dimensions of the microparticle cloud and was not perturbed outside. This is in contrast with the results of our measurements: we do not observe a significant change of the number density of metastable states inside the cloud of microparticles, instead we have a dramatic increase of it closer to the middle plane of the discharge.

Absorption of metastables in our case may be obscured by the disturbance of the ionization balance, discussed above. In [12], the plasma volume was much bigger: 13 cm RF-electrode diameter in the center of a 40 cm diameter chamber. Therefore, microparticles occupy a significantly smaller part of the discharge volume. In addition, in [12], significantly lower pressure (1–10 Pa) and significantly higher RF powers are used, resulting in spatial

enlargement of the discharge features. Consequently, the vertical extension of the microparticle cloud becomes significantly smaller than the area with enhanced ionization. This does not allow microparticles to significantly influence the ionization balance in the case of [12]. A demonstration of the transition from the local to non-local influence of microparticles is also an interesting task for future investigations.

### *4.3. Surface of a microparticle as a source of species*

The surface of a microparticle is not only a sink of plasma particles. It may also serve as a source of either impurities due to sputtering or of electrons due to secondary emission. It is known that under static pressure conditions in the PK-3 Nefedov chamber, nanoparticles grow due to the sputtering of either the melamineformaldehyde microspheres, lying on the bottom electrode, or those levitating in the volume of the chamber under microgravity conditions [14]. In this case, the amount of radicals in the discharge volume is fairly large and nanoparticles are grown on the timescale of minutes at, however, much higher RF power compared to that we use. Since in our experiments the gas in the chamber is refreshed every 40 s, we may most likely neglect the influence of sputtering on the plasma. Monitoring the emission spectra in between two gas pulses showed no dependence of their evolution on the presence of microparticles in the discharge. The periodic evolution of the spectra is therefore associated with periodic pressure variations only.

Secondary electron emission caused by ions and especially metastable atoms may become significant. For argon metastables the yield may approach unity on metallic surfaces [29]. Emission of electrons from surfaces under the effect of metastable rare-gas atoms is used in surface analysis (so-called metastable deexcitation spectroscopy, see e.g. [30]) and takes place therefore on materials of different nature. To reveal the role of the secondary electron emission from the surfaces of microparticles levitating in plasmas, special dedicated experiments are required.

## 5. Conclusion

Microparticles, immersed in a RF-discharge plasma under gravity conditions levitate above the powered electrode in a glow region, i.e. an area with increased electron temperature. For the PK-3+ setup it was demonstrated that for large clouds of microparticles, whose axial extension is comparable to the axial extension of the glow region, their influence on the plasma is non-local. The presence of such a microparticle cloud leads to the enlargement of the bottom glow region, containing the microparticles. Measurements of the densities of 1s excited states of argon did not reveal significant changes in the amplitudes of their variation, whereas some local values increased by a factor of two or more in the presence of microparticles. The upper glow region stayed practically unperturbed. The most probable mechanism responsible for this influence is disturbance of the ionization balance by the levitating microparticles.

## Acknowledgments

We acknowledge important discussions with Dr B Klumov as well as help in conducting the experiments from Dr T Antonova. This work was supported by DLR/BMWi (grant no. 50WP0203).

## References


[1] Bouchoule A 1999 Technological impacts of dusty plasmas *Plasmas: Physics, Chemistry and Technological Impacts in Plasma Processing* ed A Bouchoule (New York: Wiley)
[2] Vladimirov S V and Ostrikov K 2004 *Phys. Rep.* **393** 175
[3] Fortov V E, Khrapak A G, Khrapak S A, Molotkov V I and Petrov O F 2004 *Phys.-Usp.* **47** 447
[4] Dimoff K and Smy P R 1970 *Phys. Lett.* A **32** 13
[5] Bouchoule A and Boufendi L 1993 *Plasma Sources Sci. Technol.* **2** 204
[6] Bouchoule A and Boufendi L 1994 *Plasma Sources Sci. Technol.* **3** 292
[7] Tachibana K, Hayashi Y, Okuno T and Tatsuta T 1994 *Plasma Sources Sci. Technol.* **3** 314
[8] Böhm C and Perrin J 1991 *J. Phys. D: Appl. Phys.* **24** 865
[9] Fridman A A, Boufendi L, Hibid T, Potapkin B V and Bouchoule A 1996 *J. Appl. Phys.* **79** 1303
[10] Raizer Yu P, Shneider M N and Yatsenko N A 1995 *Radio-Frequency Capacitive Discharges* (New York: CRC Press)
[11] Denysenko I, Berndt J, Kovachevich E, Stefanovic I, Selenin V and Winter J 2006 *Phys. Plasmas* **13** 073507
[12] Do H T, Kersten H and Hippler R 2008 *New J. Phys.* **10** 053010
[13] Thomas H M *et al* 2008 *New J. Phys.* **10** 033036
[14] Mikikian M *et al* 2003 *New J. Phys.* **5** 19
[15] Mikikian M, Couëdel L, Cavarroc M, Tessier Y and Boufendi L 2007 *New J. Phys.* **9** 268
[16] Ochkin V N 2009 *Spectroscopy of Low Temperature Plasma* (Berlin: Wiley)
[17] Gavare Z, Gött D, Pipa A V, Röpcke J and Skudra A 2006 *Plasma Sources Sci. Technol.* **15** 391
[18] Klindworth M, Arp O and Piel A 2007 *Rev. Sci. Instrum.* **78** 033502
[19] Takahashi K, Thomas H M, Morfill G E, Ivlev A V, Hayashi Y and Adachi S 2008 Diagnosis in complex plasmas for microgravity experiments (PK-3 plus) *Multifacets of Dusty Plasmas* (*AIP Conf. Proc.* vol 1041) ed J T Mendoça, D P Resendes and P K Shukla (Berlin: Springer)
[20] Copley G H and Camm D M 1974 *J. Quant. Spectrosc. Radiat. Transfer* **14** 899
[21] Aeschliman D P, Hill R A and Evans D L 1976 *Phys. Rev.* A **14** 1421
[22] Schulze M, Yanguas-Gil A, von Keudell A and Awakowitz P 2008 *J. Phys. D: Appl. Phys.* **41** 065206
[23] Nefedov A P, Petrov O F and Vaulina O S 1997 *Appl. Opt.* **36** 1357
[24] Rothermel H, Hagl T, Morfill G E, Thoma M H and Thomas H M 2002 *Phys. Rev. Lett.* **89** 175001
[25] Gudmundsson J T and Thorsteinsson E G 2007 *Plasma Sources Sci. Technol.* **16** 399
[26] Melandsø F and Havnes O 1991 *J. Geophys. Res.* **96** 5837
[27] Mott-Smith H M and Langmuir I 1926 *Phys. Rev.* **28** 727
[28] Stoffels WW, Stoffels E, Swinkels G H P M, Boufnichel M and Kroesen G M W 1999 *Phys. Rev.* E **59** 2302
[29] Dunning F B and Smith A C H 1971 *J. Phys. B: At. Mol. Phys.* **4** 1696
[30] Sesselman W, Konrad H, Ertl G, Küppers J, Woratschek B and Haberland H 1983 *Phys. Rev. Lett.* **50** 446

Pis'ma v ZhETF, vol. 91, iss. 5, pp. 249 – 253 © 2010 March 10

# Determination of electron temperature in low-pressure plasmas by means of optical emission spectroscopy

*S. Mitic*, B. A. Klumov*+, M. Y. Pustylnik*, G. E. Morfill**

*Max-Planck-Institut für Extraterrestrische Physik, D-85740 Garching, Germany

+Joint Institute for High Temperatures RAS, 125412 Moscow, Russia

Submitted 20 January 2010
Resubmitted 3 February 2010

A simple model, allowing to determine the electron temperature in a steady-state low-pressure plasma, is proposed. The model makes use of optical cross-sections and therefore takes into account direct and cascade excitation from ground and metastable states. Spectroscopic data from Mitic et al. (New J. Phys. **11**, 083020 (2009)) are used to illustrate the performance of the method.

Optical emission spectroscopy is a widely used non-intrusive method of plasma diagnostics [1]. The advantage of low-pressure plasmas is that the excited levels except for long-living metastables decay only radiatively. In equilibrium decay rate should equal the excitation rate, including the excitation from ground and metastable states. Excitation rate, however, is proportional to the electron density. Therefore, the ratio of line intensities, emitted from the same volume, depends only on the excitation cross-sections and the electron energy distribution function (EEDF). Provided the excitation cross-sections are known and the shape of the EEDF can be hypothesized, parameters of the EEDF (in the simplest case of the Maxwellian EEDF, on which we concentrate ourselves further in the article, electron temperature $T_e$) can be determined [2 – 5]. We should note, that a necessary instrumental condition for this kind of measurement is that a spectroscopic system is at least relatively calibrated.

Here we propose a method, that allows to determine the parameters of the EEDF, using the ratio of intensities of the same spectral line, measured from two different, but equal volumes of the plasma. This cancels the necessity of the relative calibration.

**Model.** Our assumptions are the following:

1) plasma is optically thin along any direction for the observed spectral lines; resonant vacuum UV radiation, however, may be trapped;

2) the shape of the EEDF in both volumes is Maxwellian with temperatures $T_{e,1}$ and $T_{e,2}$;

3) in both volumes the radiative levels are populated by (i) direct electron impact excitation of ground and metastable states and (ii) cascades from upper lying levels;

4) in both volumes depopulation of the levels is only by the radiative decay;

5) within each of the volumes the plasma is uniform.

In our consideration we use the optical cross-sections [7, 8] for the ground and metastable states. The advantage of optical cross-sections versus direct excitation cross-sections is that the optical cross-sections connect electron flux in the plasma with the photon flux it produces in a specific transition by exciting ground state or metastable atoms: they automatically account for such issues as the population of the upper level of the transition from cascades, radiation trapping, multiple decay channels of the upper level.

The measured intensity of a spectral line can be expressed as follows:

$$I_{ij} = C_{ij} h\nu_{ij} n_e \sum_s n_s k_{ij}^s, \qquad (1)$$

where $C_{ij}$ is the sensitivity of the detector for the photons with energy $h\nu_{ij}$, $n_e$ electron density, $n_s$ is the density of the state $s$, excitation from which is considered (i.e. either ground state $g$ or one of the metastable states) and $k_{ij}^s$ is the emission rate in the transition $i \to j$ due to the excitation from the state $s$.

$$k_{ij}^s = \int_0^\infty v\sigma_{ij}^s(v) f(v) dv, \qquad (2)$$

where $v$ is the electron velocity, $\sigma_{ij}^s(v)$ is the optical cross-section for the state $s$ and transition $i \to j$, $f(v)$ is the electron velocity distribution function. In the case of Maxwellian EEDF $k_{ij}^s$ depends only on the electron temperature.

Suppose $I_{ij,1}$ and $I_{ij,2}$ are the intensities measured from the two different volumes of the plasma. Their ratio can then be expressed as follows:

$$E_{ij}\left(T_{e,1}, T_{e,2}, \frac{n_{e,1}}{n_{e,2}}\right) = \frac{I_{ij,1}}{I_{ij,2}} = \frac{n_{e,1}}{n_{e,2}} \frac{\sum_s n_{s,1} k_{ij}^s(T_{e,1})}{\sum_s n_{s,2} k_{ij}^s(T_{e,2})}. \qquad (3)$$

$n_{e,1}$, $n_{e,2}$ are here the electron densities and $n_{s,1}$, $n_{s,2}$ are the densities of long-living states of argon in the two volumes respectively. Ratio $E_{ij}$ depends on both electron temperatures and ratio of electron densities $n_{e,1}/n_{e,2}$. Let us consider three different transitions $\alpha, \beta$ and $\gamma$. Then, using two transitions we can define a quantity $F$, which is totally independent of electron densities:

$$F_{\alpha,\beta}(T_{e,1}, T_{e,2}) = \frac{E_\alpha(T_{e,1}, T_{e,2}, n_{e,1}/n_{e,2})}{E_\beta(T_{e,1}, T_{e,2}, n_{e,1}/n_{e,2})} = \frac{I_{\alpha,1}/I_{\alpha,2}}{I_{\beta,1}/I_{\beta,2}}. \quad (4)$$

Adding the third transition allows us to determine $T_{e,1}$ and $T_{e,2}$, solving the following system of equations:

$$F_{\alpha,\beta}(T_{e,1}, T_{e,2}) - \frac{I_{\alpha,1}/I_{\alpha,2}}{I_{\beta,1}/I_{\beta,2}} = 0, \quad (5)$$

$$F_{\beta,\gamma}(T_{e,1}, T_{e,2}) - \frac{I_{\beta,1}/I_{\beta,2}}{I_{\gamma,1}/I_{\gamma,2}} = 0. \quad (6)$$

In principle, a system, involving more transitions, can be constructed and furhter solved by, e.g. using the mean least squares method.

We concentrate on the Maxwellian EEDF only for simplicity. Taking more spectral lines into consideration would allow to extend this method for the case of a more complicated EEDF.

**Experiment.** As an example we use the spectroscopic data, obtained in a previous [9] experiment. In this experiment the plasma is generated in a PK3+ chamber, which is the heart of a International-Space-Station-based complex plasma laboratory [10]. Briefly, PK3+ is a symmetrically driven parallel-plate 13.56 MHz discharge with the disc-shaped electrodes of 6 cm in diameter and 3 cm gap. Experiments were carried out in argon buffer gas at working pressure of 60 Pa, RF voltage of about 20 V peak-to-peak and power of 0.2 W. Spectra were recorded using a Hamamatsu Mini-spectrometer Module TG series, by collecting column of light parallel to the electrodes through a collimator into the optic fiber, which could be moved vertically by a translation stage in order to obtain axiat profile of the emission.

Two types of measurements were done: one in pure argon plasma and the other with a cloud of melamine-formaldehyde monodisperse spheres of 2.55 $\mu$m diameter, levitating in it. Under gravity conditions these microparticles concentrated themselves in the vicinity of the bottom electrode. Typical number density of microparticles, levitating in the plasma, was always of the order of $10^{11}\,\mathrm{m}^{-3}$.

Optical cross-section for the spectral lines of argon are known for the excitation from the ground state [11] as well as from the metastable states $1s_5$ and $1s_3$ [12].

The input parameters of the method, described above, are the densities of the long-living argon states, i.e. $n_g$, $n_{1s_5}$, $n_{1s_3}$ and intensities of spectral lines. Since the ionization degree is small, $n_g$ can be determined from the argon pressure. Metastable densities are measured by a single-mirror method [13], which is corrected for the presence of a microparticle cloud in a plasma [9].

Use of the intensities of the spectral lines, measured in Ref. [9] requires an important physical comment. In Ref. [9] it was revealed, that self-absorption (together with the extinction in case of complex plasmas) is important. In fact, measurement of $1s$ states, performed in Ref. [9], was possible due to the relatively large self-absorption. We assumed, however, that for the spectral lines $\alpha, \beta$ and $\gamma$ the plasma is optically thin. This means, that the measured intensities of the spectral lines cannot be simply substituted into eqs. (5) and (6). To get rid of the self-absorption and extinction the so-called escape factor should be used [14]. Since our detector observes a thin column of plasma, it is not difficult to connect the measured intensity $I_{ij}^{\mathrm{meas}}$ to the "local" intensity $I_{ij}^{\mathrm{loc}}$, i.e. to the locally emitted photon flux [9] for a Doppler-broadened line:

$$I_{ij}^{\mathrm{loc}} = I_{ij}^{\mathrm{meas}} \left( \frac{1}{\sqrt{\pi}} \int_{-\infty}^{\infty} \frac{e^{-\omega^2}}{\tau_{ij}^{\mathrm{pl}}(0) e^{-\omega^2} + \ln\left(K_{ij}^{\mathrm{d}}\right)} \times \right.$$
$$\left. \times \left( 1 - \frac{\exp\left(-\tau_{ij}^{\mathrm{pl}}(0) e^{-\omega^2}\right)}{K_{ij}^{d}} \right) d\omega \right)^{-1}. \quad (7)$$

Here $\tau_{ij}^{\mathrm{pl}}(0)$ is the optical thickness in the center of the spectral line and $K_{ij}^{\mathrm{d}}$ is the microparticle-caused attenuation of the plasma light. Both values are determined in Ref. [9]. Intensities of the following three spectral lines of argon, measured by a spectrometer, are used as $I_{ij}^{\mathrm{meas}}$ : 794.8, 826.4 and 706.7 nm (corresponding transitions $\alpha = \{2p_4 \to 1s_3\}$, $\beta = \{2p_2 \to 1s_2\}$ and $\gamma = \{2p_3 \to 1s_5\}$). These measured intensities are recalculated into "local" intensities using Eq. (7) and then substituted into Eqs. (5) and (6).

We should note, that Eq. 1 does not take into account self-absorption as a populating mechanism for the level $i$. This would lead to the necessity of considering the radiation transfer in the discharge, which significantly complicates the problem.

Optical cross-sections depend on the escape factor for the vacuum UV resonant photons [11], *i.e.* background gas pressure and dimensions of the setup. Dimensions of PK3+ chamber are comparable to those of the chamber, in which the optical cross-sections were measured. The measurements of the optical cross-sections were performed in the range of pressures of $10^{-1} - 1$ Pa. In two limiting cases of small pressure and

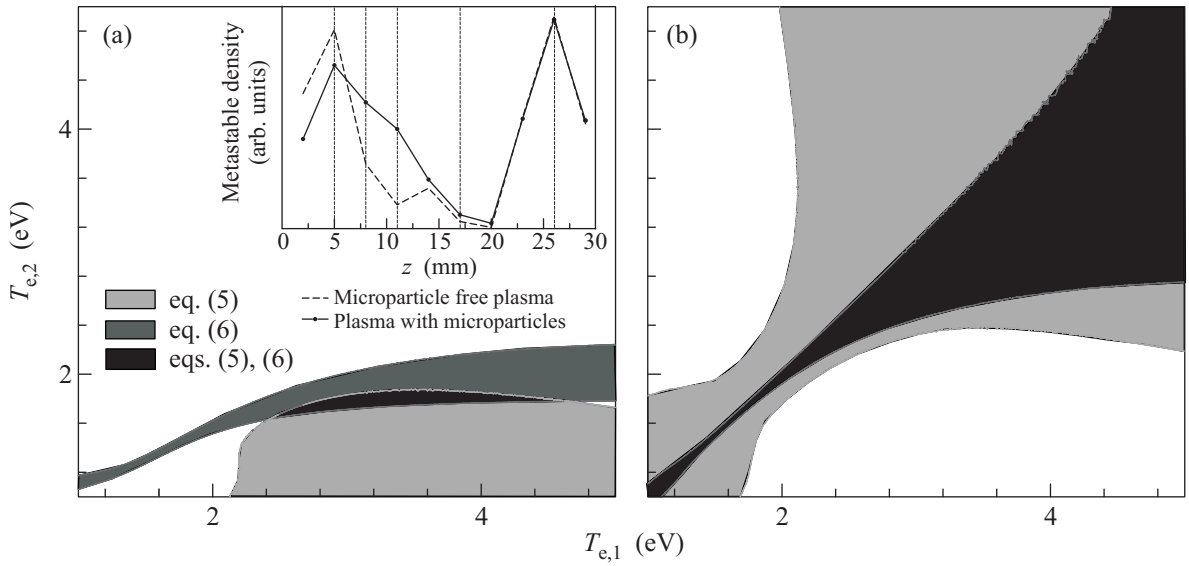


Fig.1. Solution of eqs. (5) and (6) for the points in microparticle-free plasma at the argon pressure of 60 Pa and RF power of 0.2 W [9] with $\delta F = \pm 0.05$: (a) index 1 corresponds to the vertical position $z = 5$ mm (peak of emission), index 2 – to $z = 11$ mm (minimum of the emission); in the inset the axial distributions of the number density of metastable atoms are presented; vertical dotted lines indicate the positions, at which the electron temperatures are evaluated; (b) index 1 – $z = 5$ mm (peak of emission), index 2 – $z = 26$ mm (symmetric peak of emission). Evidently, the temperatures are much better determined if the two points with significantly different parameters are considered

high pressure the optical cross-section is constant since the escape factor tends in these cases to unity and zero respectively. At high pressures the pressure dependence of the cross-sections start to saturate at about 0.66 Pa (5 mTorr). Therefore, at our working pressure this dependence is with a good guarantee saturated. Therefore, we used the optical cross-sections, measured for the pressure of 0.66 Pa.

In an ideal case solution of each of the eqs. (5) and (6) can be represented as a curve on the $(T_{e,1}, T_{e,2})$ plane. The intersection of these curves would yield the solution of the system and therefore, values of temperatures. However, in reality the line intensities are measured with a finite uncertainty, which results in the uncertainty of the function $F$. For the solution of (5) and (6) this would mean, that instead of exact values of the temperatures, only a range, in which the temperatures may lie at a given experimental uncertainty $\delta F$, can be determined. In our experiments $F_{\alpha,\beta}$ and $F_{\beta,\gamma}$ varied roughly between 0.9 and 1.1.

**Results for microparticle-free plasma.** Further we provide several examples of the solution of the system of (5) and (6). Due to large errors in the obtained temperatures, we cannot pretend on any quantitativeness of our measurements. Therefore, the examples below are used just to demonstrate the performance of the method and to give the ideas of how the method can be applied to the experimental data.

First group of examples, in which we consider two different points of the same microparticle-free discharge, is presented in Fig.1. Obviously, the temperatures are much better determined in the case, when the two points with significantly different conditions are taken. From Fig.1a we have for $T_{e,1} = 2.5 \div 4.7$ eV at the height $z = 5$ mm over the bottom electrode of the discharge and $T_{e,2} = 1.6 \div 1.8$ eV at $z = 11$ mm, i.e. $T_{e,1} > T_{e,2}$, which is expected since points 1 and 2 correspond to hump and dip of the emission respectively. At the same time in Fig.1b the intersection of the solutions of (5) and (6) covers the entire considered range of temperatures. It is therefore practically impossible to draw any quantitative information about the temperatures. However, the line $T_{e,1} = T_{e,2}$ lies inside the solution area, which is expected, since in Fig.1b symmetric points of the discharge are considered.

**Estimations of the influence of microparticles on $T_e$.** This method can be also used to evaluate the influence of the the presence of microparticles on the electron temperature by substituting into (5) and (6) the intensities, measured at the same $z$ in microparticle-free plasma and in plasma, containing a microparticle cloud (Fig.2). Previously [9] it has been revealed, that the cloud of microparticles produces a significant nonlocal influence on the distribution of the densities of $1s$ states of argon in an RF discharge. For the following consideration we define the electron temperature in a

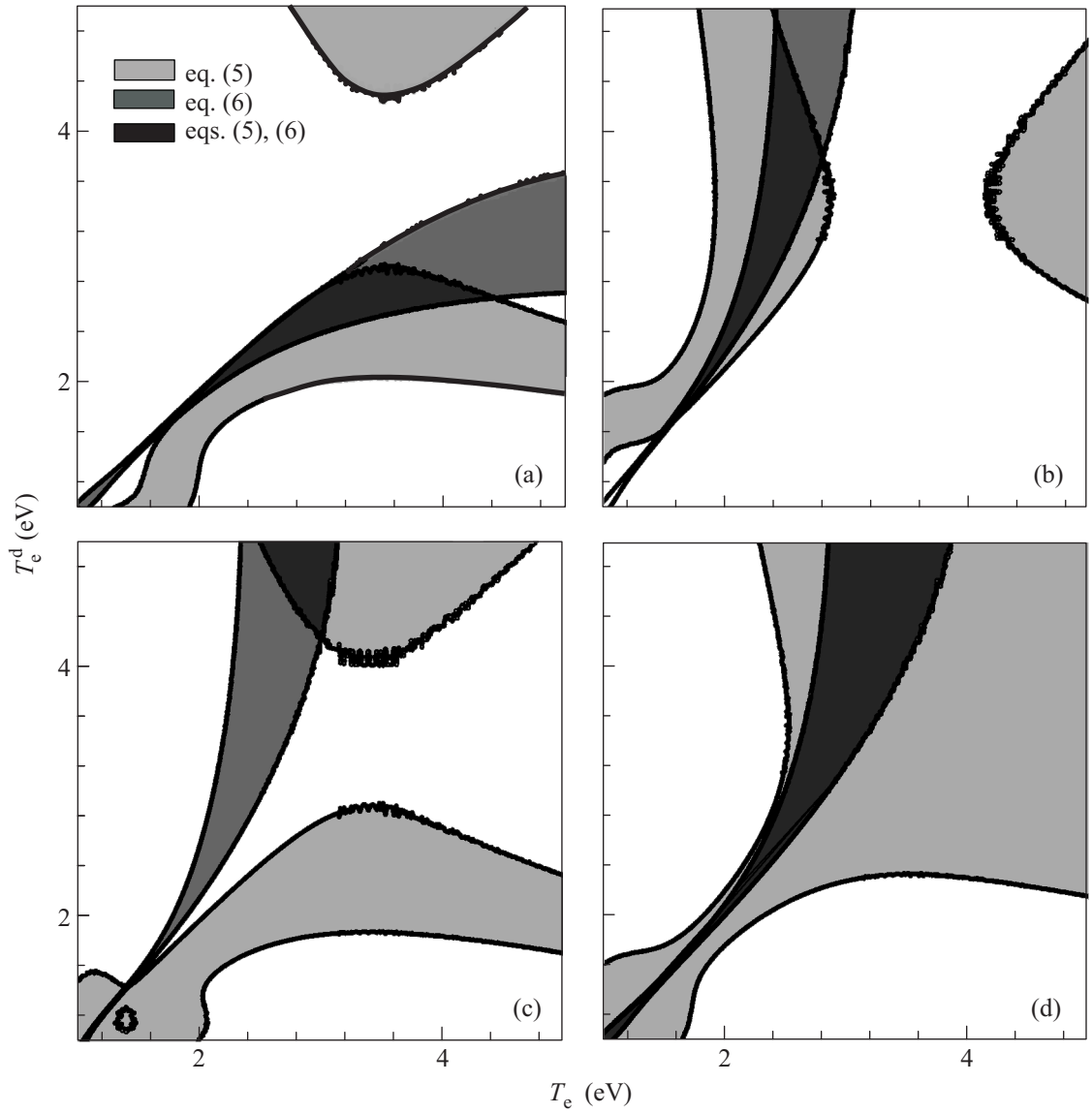


Fig.2. Solution of eqs. (5) and (6) for the points in the plasma at the argon pressure of 60 Pa and RF power of 0.2 W [9] with $\delta F = \pm 0.02$. Indices 1 and 2 correspond to the same vertical position $z$ in microparticle-free plasma and plasma with microparticles respectively; $T_e \equiv T_{e,1}$, $T_e^d \equiv T_{e,2}$. (a) $z = 5$ mm, presence of microparticles decreases the densities of $1s$ states; (b) $z = 8$ mm, presence of microparticles increases the densities of $1s$ states; (c) $z = 17$ mm, presence of microparticles practically does not affect the densities of $1s$ states; (d) $z = 26$ mm, presence of microparticles practically does not affect the densities of $1s$ states. Vertical positions for (a) and (b) are inside the microparticle cloud, whereas for (c) and (d) outside. For (d) the density of $1s$ states is significantly higher, than that for (c). $T_e$ exhibits much larger upper limit than $T_e^d$ in (a) and vice versa in (b), which is in accord with the previously observed effect of microparticles on the densities of $1s$ states of argon. For (c) and (d) effect of microparticles is negligibly small and therefore, determination of the temperatures is not possible

microparticle-free plasma $T_e \equiv T_{e,1}$ and electron temperature in a plasma, containing a microparticle cloud, $T_e^d \equiv T_{e,2}$. At $z = 5$ mm (Fig.2a) the upper limit of $T_e$ is 4.4 eV, i.e. significantly larger than that of $T_e^d$ (2.8 eV). In accord with this, presence of microparticles leads to decrease of the densities of $1s$ states at this height. Situation is opposite at $z = 8$ mm (Fig.2b), where the upper limit of $T_e^d$ is higher and the densities of $1s$ states increase in presence of microparticles. At heights $z$ of 17 and 26 mm (Fig.2c and Fig.2d respectively), where the influence of microparticles is small, $T_e$ and $T_e^d$ can hardly be determined.

In conclusion, we presented a spectroscopic method, allowing to evaluate (in the assumption of a Maxwellian

EEDF) the electron temperature in a low-pressure plasma. The input parameters of the method are the experimentally measured intensities of spectral lines and densities of metastable states. Spectroscopic data from Ref. [9] was used as an example for the temperature evaluation. The method suffers from uncertainties. The largest contribution comes from the uncertainty in the measurements of the ratios of spectral lines (5%), leading to 50% error in temperature measurement. Uncertainties in the densities of metastable states (∼20%) and optical cross-sections (∼30%) [12] were checked to be much less important. Morover, uncertainty in the $n_{1s_3}$ and $n_{1s_5}$ can be improved by using tunable laser methods, e.g. laser absorption spectroscopy [15]. We also hope for the improvement of the accuracy of the cross-section measurements in future. Another possibility to improve the accuracy of the method is to use more different line ratios, which will help to localize the solution on $(T_e^1, T_e^2)$ plane. Increasing the number of ratios involved may also allow to extend the method to non-Maxwellian multiple-parameter EEDFs and also to the relative measurements of the electron temperature.

This research was funded by Das Bundesministerium für Wirtschaft durch das Zentrum für Luft- und Raumfahrt e.V. (DLR) unter dem Förderkennzeichen 50 WB 0203.

1. V.N. Ochkin, *Spectroscopy of Low Temperature Plasma*, Wiley-WCH, Berlin, 2009.
2. R.J. Sovie, Phys. Fluids **7**, 613 (1963).
3. D. Samsonov and J. Goree, IEEE Trans. Plasma Sci. **27**, 76 (1999).
4. J.B. Boffard, C.C. Lin, and C.A. DeJoseph Jr., J. Phys. D **37**, R143 (2004).
5. N.J. Kang, S. Oh, and A. Ricard, J. Phys. D **41**, 155203 (2008).
6. X.-M. Zhu, W.-C. Chen, J. Li, and Y.-K. Pu, J. Phys. D **42**, 025203 (2009).
7. B.I. Moiseevitch and S.J. Smith, Rev. Mod. Phys. **40**, 238 (1968).
8. D.W.O. Heddle and J.W. Gallagher, Rev. Mod. Phys. **61**, 221 (1989).
9. S. Mitic, M.Y. Pustylnik, and G.E. Morfill, New J. Phys. **11**, 083020 (2009).
10. H.M. Thomas, G.E. Morfill, V.E. Fortov et al., New J. Phys. **10** 033036 (2008).
11. J.B. Boffard, B. Chiaro, T. Weber, and C.C. Lin, Atomic Data and Nuclear Data Tables **93**, 831 (2007).
12. J.B. Boffard, G.A. Piech, M.F. Gehrke et al., Phys. Rev. A **59**, 2749 (1999).
13. Z. Gavare, D. Gött, A.V. Pipa et al., Plasma Sources Sci. Technol. **15** 391 (2006).
14. F.E. Irons and J. Quant, Spectrosc. Radiat. Transfer **22**, 1 (1979).
15. H.T. Do, V. Sushkov, and R. Hippler, New J. Phys. **11**, 033020 (2009).